Experimental And Computational Studies Of Dynamic Processes In Ionic Water Clusters

Alexey S. Zatula

2012

Dissertation for the degree philosophiae doctor (Ph.D.)
Department of Chemistry, Faculty of Mathematics and Natural Sciences
University of Oslo, Norway

Series of dissertations submitted to the
Faculty of Mathematics and Natural Sciences, University of Oslo
No. 1243

ISSN 1501-7710

Cover: Inger Sandved Anfinsen.
Printed in Norway: AIT Oslo AS.

Produced in co-operation with Akademika publishing.
The thesis is produced by Unipub merely in connection with the
thesis defence. Kindly direct all inquiries regarding the thesis to the copyright
holder or the unit which grants the doctorate.

Table of contents

I Abstract

Clusters of water molecules mimic the transition from gas phase to bulk water. Cluster species of the desired sizes can be selected using mass spectrometric techniques and their size-dependent properties can thereby be measured. The properties of small ionic clusters are of particular relevance to atmospheric science, providing insights into nucleation phenomena.

This work is dedicated to the investigation of properties of selected ionic molecular clusters and their gas phase reactions with heavy water or ammonia, with a strong emphasis on proton transfer phenomena. This has been achieved both experimentally in cluster beam experiments and by quantum chemical calculations.

Both in the abundance spectra and the evaporation patterns of the investigated aqueous clusters “magic numbers” discontinuities in otherwise smoothly varying distributions were observed, and are discussed. To further examine a marked difference in the observed “magic-number” behaviour of $H^+(\text{pyridine})_1(H_2O)_n$ and $H^+(NH_3)_1(\text{pyridine})_1(H_2O)_n$ clusters, quantum chemical calculations have been employed. Next, relative reaction cross sections were measured for cluster ions reacting with D_2O and with NH_3 in the collision cell. Analysis of the results for the reaction $H^+(\text{pyridine})_1(H_2O)_n + NH_3$ allowed us to improve a kinetic model of the atmospheric positive ion composition.

Upon reaction of a cluster with D_2O a short-lived reaction intermediate is formed, which is followed by subsequent loss of D_2O, HDO or H_2O. The reaction channel leading to the loss of HDO requires proton mobility within the cluster, involving O–H-bond activation. The loss of HDO was not observed for protonated water clusters containing one pyridine molecule, a consequence of the immobilizing effect on the extra proton by the nitrogen base site. Similarly, the rates of protium/deuterium exchange for water clusters containing alkali metal ions are consistently extremely low.

However, the experiments show enhanced proton mobility in water clusters containing two or three pyridine molecules ($H^+(\text{pyridine})_{2–3}(H_2O)_n$), in 2,2’-bipyridine and 2,2’-ethylenebipyridine containing water clusters as well as in bisulfate water clusters ($HSO_4^-(H_2O)_n$). On the basis of systematic quantum chemical calculations we present consistent mechanisms for low energy water rearrangement and proton transfer along preformed "wires" of hydrogen bonds between the two distinct sites provided by these core ions in complete support of the experimental findings.

II List of publications

- Paper I

M. J. Ryding, A. S. Zatula, P. U. Andersson and E. Uggerud. Isotope exchange in reactions between size-selected ionic water clusters, $H^+(\text{pyridine})_m(H_2O)_n$, and D_2O. *Physical Chemistry Chemical Physics, 2011. 13(4), p. 1356-1367.*

- Paper II

A. S. Zatula, P. U. Andersson, M. J. Ryding and E. Uggerud. Proton mobility and stability of water clusters containing the bisulfate anion, $HSO_4^-(H_2O)_n$. *Physical Chemistry Chemical Physics, 2011. 13(29), p. 13287-13294.*

- Paper III

M. J. Ryding, Å. M. Jonsson, A. S. Zatula, P. U. Andersson and E. Uggerud. Reactions of $H^+(\text{pyridine})_m(H_2O)_n$ and $H^+(NH_3)_1(\text{pyridine})_m(H_2O)_n$ with NH_3: experiments and kinetic modelling. *Atmospheric Chemistry and Physics, 2012. 12, p. 2809-2822.*

- Paper IV

M. J. Ryding, K. I. Ruusuvuori, P. U. Andersson, A. S. Zatula, M. J. McGrath, T. C. Kurtén, I. K. Ortega Colomer, H. Vehkamäki and E. Uggerud. Structural Rearrangements and Magic Numbers in Reactions between Pyridine-containing Water Clusters and Ammonia. *The Journal of Physical Chemistry A, 2012. 116(20), p. 4902–4908.*

- Paper V

M. J. Ryding, P. U. Andersson, A. S. Zatula and E. Uggerud. Proton mobility in water clusters. *European Journal Of Mass Spectrometry, 2012. 18(2), p. 215–222.*

- Paper VI

A. S. Zatula, M. J. Ryding, P. U. Andersson, and E. Uggerud. Proton mobility and stability of water clusters containing alkali metal ions. *International Journal of Mass Spectrometry, accepted 2012.*

- Paper VII

A. S. Zatula, M. J. Ryding, and E. Uggerud. Concerted proton migration along short hydrogen bond wires in bipyridine/water clusters. *Physical Chemistry Chemical Physics, submitted 2012.*

1 Introduction

Better understanding of the nature of ions in solution is one of the never-ending tasks of physical chemistry and biology. In ionic clusters core ion of either polarity is solvated by a given number of neutral molecules. Despite their small size, clusters are governed by many of the same interactions that maintain ion solvation in solution. They also keep many characteristics of the bulk media that cause the wealth of features of condensed-phase dynamics. By introducing ionic or neutral molecules into a cluster of solvent molecules it becomes possible to investigate solvation at a fundamental level.

On this basis, detailed studies of formation, growth, physical properties and interactions within water cluster will most certainly remain important to improving our understanding of the nature of hydrogen-bonded systems and the chemistry of aqueous solutions.

However, clusters are not just interesting subjects of academic interest. For instance, molecular clusters are all-important for physical, chemical and biological processes of the earth and its atmosphere, acting as a solvent, reagent, precursor for particle formation, *etc*. Water clusters are relevant to the vital atmospheric processes regulating cloud formation, and thereby affect the earth's radiation balance and precipitation patterns. Moreover, the influence of aerosol particles has wider impact, having also effect on weather patterns and visibility. The effect of aerosols is a primary uncertainty in prediction of global climate changes and the greenhouse effect [1]. Molecular clusters are also closely related to the issues of air quality and human health, since the clusters can penetrate to the deepest part of respiratory tract, causing respiratory and circulatory diseases. For example, the design of asthma inhalers requires detailed insight into aerosol formation and behaviour.

Both neutral and charged molecular clusters are found in the atmosphere, and their importance for cloud formation is significant. Clusters containing amines and sulphur compounds are believed to act as key precursors for the formation of atmospheric particles, they are also important in understanding the chemistry of the lower part of the earth's atmosphere.

Moreover, proton transfer is one of the most important elementary reactions and play undisputable role in chemical, biochemical and atmospheric processes. Proton mobility in water occurs by means of fast proton hops, the so-called Grotthuss mechanism. This process and its elementary reaction steps can be examined in great detail by applying mass spectrometric methods to ionic water clusters in combination with analysis of cluster size trends in hydrogen/deuterium isotope exchange-rates. Analysis of the experiments may be facilitated by systematic quantum chemical model calculations.

The present study deals with relatively small ionic clusters (size $\leq$ 1500 u) consisting of water molecules and other species–bisulfate, ammonia and pyridine–common substances found in the atmosphere. The investigation aims at understanding the initial stages of water cluster formation from ions, emphasizing structural rearrangements of clusters related to proton transfer processes. To support the findings, results of investigations of clusters containing alkali-metal ions and bipyridine-family ions are also presented.

The clusters were studied in ion beam experiments: clusters produced by an electrospray (ESI) ion source were transferred into a part of instrument where they underwent gas phase reactions with D_2O or NH_3. Using the same instrument, cluster size distributions and the kinetics of molecular evaporation from the clusters were also measured. In total, the results of this work include: abundance spectra, evaporation patterns, relative cross sections for reactions of clusters with NH_3 and D_2O, and analysis of the tendency for the clusters to exhibit intermolecular hydrogen/deuterium rearrangements during the lifetime of a reaction intermediate. The experimental results were also used to refine a kinetic model of atmospheric ion abundances. As a part of the study, a series of quantum-chemical calculations has been conducted, with an aim in obtaining better insight into the results of the H/D exchange experiments. Moreover, a theoretical investigation aimed at examining surprising magic-number behaviour of clusters containing pyridine is included.

This introduction is followed by Chapter 2 where an overview on the role of molecular clusters in the Earth's atmosphere is discussed. Chapter 2 also provides a short background concerning the common experimental and theoretical methods used as well as providing the theoretical framework for the proton transfer studies in bulk systems and clusters. Chapter 3 describes the quadrupole time-of-flight unit (ESI-QTOF) setup that was used in the experiments as well as practical details of the quantum chemical simulations. The results are summarized in Chapter 4, and are followed by the most important final conclusions in Chapter 5.

2 Background

This chapter offers a brief introduction to key aspects of the Earth's atmosphere and basic properties of atmospheric particles (Chapter 2.1). A background of commonly used experimental and theoretical approaches of cluster studies is provided in Chapter 2.2 and 2.3, consequently. This is followed by Chapter 2.4 which introduces a short summary of the literature on properties and reactivity of ions.

2.1 Aerosols and clusters in the atmosphere

The Earth's atmosphere is the layer of gas and ions surrounding the Earth, which can be divided into several parts based on the temperature variation with height [2]. The troposphere is closest to earth part of the atmosphere, which extends to about 12 km above the surface. The tropospheric boundary layer is the part of the troposphere that is directly influenced by the surface of the Earth, which causes the temperature to be higher here, in turn, making for a high degree of mixing of air in this region. Above the tropopause lies the stratosphere, where the temperature increases gradually due to the absorption of solar UV radiation. Above the ozone layer, there is the mesosphere, where temperature decreases with height, followed by the thermosphere, which is characterized by a temperature that is increasing again due to absorption of radiation from the sun. The atmospheric pressure decreases with height in a crudely exponential manner throughout entire atmosphere [3].

We begin the chapter by discussing general properties of aerosols (Section 2.1.1). Section 2.1.2 provides introduction of health and environmental effects of atmospheric particles. After a discussion of formation and growth processes of atmospheric entities (Section 2.1.3), we will briefly review the chemistry of ionic clusters in the atmosphere (Section 2.1.4).

2.1.1 General properties of aerosols

An aerosol is a dispersion consisting of solid or liquid particles in a gas. Therefore atmospheric aerosols are particles (*e.g.* soot particles, dust, pollen) suspended in the air. The atmosphere is a very complex and constantly changing system, so it is obvious that atmospheric aerosols are strongly variable in terms of size and concentration. For instance, particle diameter spans several orders of magnitude, from a few nanometers to a few tenths of a millimeter [4]. The particle concentration (*usually expressed as the number of particles per volume*) is 1–10^5 cm^{-3} in the troposphere. It is not uniform and is typically divided into size ranges referred to as "modes": nucleation mode, Aitken mode, accumulation mode and coarse mode. Each size mode represents particles with different sources, formation mechanisms, chemical composition, and paths of removal from the atmosphere [5]. In general, atmospheric residence time of aerosols is influenced by such processes as Brownian motion, gravitational settling, coagulation, rainout and washout [6].

Atmospheric particles are classified according to their source, *e.g.* natural or anthropogenic particles, primary or secondary particles. A primary particle source implies that the particles are emitted in the condensed phase directly into the atmosphere, while a secondary source is one where particles are formed by reactions of gaseous substances in the atmosphere. Examples of primary sources include products of combustion, mechanical wear and tear, salt particles from sea-spray, pollen, desert dust, *etc*. [5] Anthropogenic sources include for example combustion of fossil fuels, industrial emissions or biomass burning. The natural sources are those occurring without the influence of man and may include sea-spray, forest fire, soil dust, pollens, *etc*., as well as gases emitted by volcano eruption (SO_2, H_2S) and phytoplankton (dimethylsulfide). They dominate the total emitted particulate mass on the global scale; however, anthropogenic emissions dominate in densely populated and industrialized areas [4].

The formation of aerosols in the atmosphere (*i.e.* secondary atmospheric aerosols) is a complex process; all mechanisms and steps are not fully understood. The particle formation can likely be divided into two parts, first the nucleation step where a nanometer sized molecular cluster (charged or neutral) is formed, and then growth of the cluster into a particle [7].

2.1.2 Environmental effects of atmospheric aerosols

According to the most recent report by the Intergovernmental Panel on Climate Change (IPPC) [1], the influence of human activities on the climate is significant. Figure 1 shows the change in radiative forcing for different contributing factors relative to the pre-industrial era. The radiative forcing is defined as the change in net irradiance (the difference in incoming and outgoing radiation energy) at the tropopause, assuming fixed tropospheric and surface temperatures but allowing the stratospheric temperature to readjust to equilibrium. As seen from the IPCC estimate, the overall influence of aerosols seems to be cooling the atmosphere, however there are large uncertainties regarding to which degree. The direct mechanisms that influence the global climate include scattering, reflection and absorption of solar radiation. The indirect effects mainly relate to the aerosol particles acting as cloud condensation nuclei. As seen from the Figure 1, the major uncertainties in current estimates appear from the effects of aerosols, thus further study of their influence is vital for correct estimation of the rate of climate change.

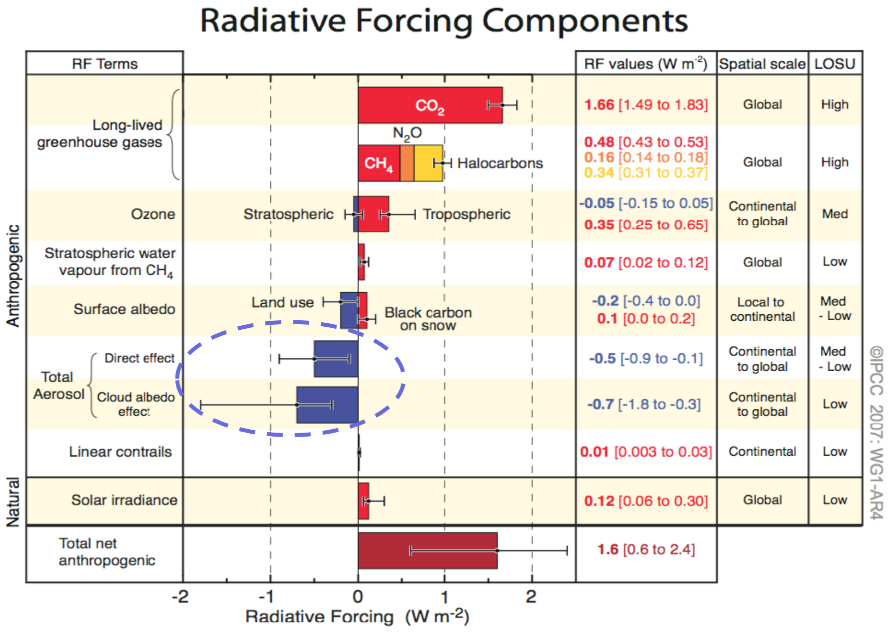

Figure 1. Impact on atmospheric radiative forcing (RF) due to human influence, as well as the level of scientific understanding (LOSU) for different sources [1].

Among other environmental effects of atmospheric aerosols there are also effects on visibility, ozone layer depletion, acid rains, *etc.* [8] However, effects of aerosols do not confine only to influence on the climate. The biggest concern in urban areas is particle emission from combustion and other sources also affecting the health and well being of humans. A human being processes 10–25 m^3 of air during a normal day, and naturally, particles enter respiratory system, and some are able to reach the deepest parts of the lungs such as the bronchioles or alveoli [5]. Since nanoparticles more readily penetrate deep into lungs, they are of a bigger threat to human health than larger ones [9]. Furthermore, increased levels of fine particles were shown to lead to a lowered life expectancy [10], affect cardiovascular and respiratory morbidity and mortality (*e.g.* [11, 12]). On the other hand, according to Metzger *et al.* ultrafine particles may anticorrelate with health risks [13]. In summary, there is still a considerable uncertainty with respect to properties of the particles that have the largest impact on health and mechanisms of their action. Impact of aerosols appears to be adverse, going beyond direct influence on human health, including climatological concerns [14] and, for example, practical challenges in constructing and improving asthma inhalers [15].

2.1.3 Formation and growth of molecular clusters in the atmosphere

Aerosol dynamic processes include homogeneous and heterogeneous nucleation, coagulation, deposition, condensation and evaporation [5]. Homogeneous nucleation is a process by which particles are formed from supersaturated gases without help from ions or a solid seed, *i.e.* only the gases that condense take part in the process. In contrast, heterogeneous nucleation involves ions or condensation nuclei.

From a macroscopic point of view, gas-to-particle nucleation can occur when the vapour pressure of some compound in the gas phase exceeds its saturation vapour pressure under the ambient conditions. For most atmospheric levels of air water content, homogeneous nucleation of pure water particles is believed to be rare, due to the difficulties of forming stable pure clusters $(H_2O)_n$, without very high supersaturation levels [5]. This is ascribed to the Kelvin effect: the equilibrium vapour pressure over a curved surface is greater than over a flat surface. This means that for a given level of supersaturation the droplets below a certain size will evaporate since the molecules tend to leave the surface more readily as the curvature increases. However, particles above a certain size (Kelvin diameter) will keep on growing. In microscopic terms, this implies that the binding energies of the embryonic molecular clusters are large enough to compensate for the negative entropy of the cluster formation.

As opposed to homogeneous nucleation, heterogeneous nucleation of water can happen even below supersaturation. Compared to homogeneous nucleation, heterogeneous nucleation is favoured in different ways depending on the nature of nuclei. On the one hand, an insoluble nuclei in a droplet leads to a larger "starting size" compared to homogenous nucleation, *i.e.* it is easier for the particle to reach the critical Kelvin diameter needed for growth. On the other hand, the presence of a charge adds thermodynamical stability to a cluster and enhances the initial growth rate by electrostatic dipole–charge interaction between the core ion and the strongly dipolar condensing molecules [5]. Finally, there is a continuous and ubiquitous supply of stable, fast growing ionic embryos in the atmosphere [16-18]. Thus, heterogeneous nucleation is the primary mechanism for atmospheric cloud formation.

It is clear why atmospheric nucleation is almost always multicomponent: if a molecule is strongly attached to other molecules of the same kind, it is naturally unlikely that it evaporates in the first place. Thus, the most probable nucleation mechanisms involve at least two types of molecules, which are attracted to each other stronger than to themselves. Possible pairs can be presumed from general chemistry: strong acids and strong bases, ions with opposite charge, or hydrogen bond donor and acceptor pairs are among the most obvious candidates.

Four processes are often suggested as the main mechanisms for nucleation of atmospheric clusters: binary homogeneous nucleation by water and sulfuric acid; ternary homogeneous nucleation of water, sulfuric acid and ammonia; homogeneous nucleation by iodine species; ion-induced nucleation of the binary or ternary type, or with organic species [7]. Upon closer look, sulfuric acid appears to be a common factor in most proposed mechanisms of atmospheric particle formation. Furthermore, particle formation rates have been observed to correlate with the concentration of sulfuric acid in a large variety of conditions [19]. So it is no surprise that nowadays it is agreed that sulfuric acid plays a central role in gas-phase nucleation [20-22] and it is considered to form key pre-nucleation clusters of water droplets and ice particles in the atmosphere. However, pure binary homogeneous nucleation of water and sulfuric acid is believed to take place mainly in an environment where relatively high sulfuric acid concentration can be achieved, or in the free troposphere, where the temperature and background aerosol concentration are low enough to allow significant sulfuric acid–water cluster formation [23].

Ternary homogeneous nucleation involving ammonia is suggested as the mechanism for nucleation in the continental boundary layer [24-26]. It should be noted that some recent studies [27-29] have suggested that the clustering or reactions of sulfuric acid with various organic species might be an important nucleation mechanism in the atmosphere. Further interesting studies [30, 31] show that amines (methylamine, dimethylamine, diethylamine, *etc.*) are even more effective in enhancing condensation of sulfuric acid molecules on the sulfuric acid/amine cluster than ammonia, both for charged and neutral clusters [7, 32]. In the coastal boundary layer iodine species after being emitted, form various iodine oxides like IO and OIO, which subsequently condense to form clusters. Homogeneous nucleation of iodine species is suggested to strongly influence particle formation in the coastal boundary layer [33]. Ion-induced nucleation of sulfuric acid–water clusters or other compounds [17, 34, 35] also may be an important source of particles in the upper troposphere or lower stratosphere.

While clusters (both charged and neutral) are always present, the formation of larger particles (> 3 nm) is usually observed to occur in bursts, known as nucleation events. Atmospheric particles interact with each other and with gases during their lifetime. If the clusters are small, extensive fragmentation is then believed to follow the recombination of charged cluster ions, but if the clusters are large enough, coalescence is assumed to occur. The formed clusters can thereafter be large enough to continue to grow spontaneously by condensation [36]. The particle precursors, *i.e.* the clusters, can grow into particles by several mechanisms. If the cluster was formed by homogenous nucleation, it is possible that growth occurs by condensation of the same species that formed the original cluster. This is a complete homogenous nucleation from gaseous species to particles. If there is a charge present in the cluster, the corresponding mechanism is the ion-induced heterogeneous particle nucleation. Clusters can also grow by undergoing self-coagulation, *i.e.* clusters combine to form larger particles [32].

2.1.4 Ionic clusters in the atmosphere

The ions that are the precursors for ion-induced nucleation of clusters are present in all parts of the atmosphere. Although charged clusters are much more stable and effective in nucleation than neutral ones, the abundance of neutral clusters is estimated to be 10–100 times larger than that of ionic clusters [37]. Consequently, ionic cluster formation is estimated to result in no more than 10% of the total particle formation rate in the lower troposphere. Recombination of ionic clusters could also account for ~10% of the formed neutral clusters [38]. Even though ions represent a small fraction of the atmosphere, they have a disproportionate influence on many atmospheric phenomena.

In the troposphere and stratosphere, ionization of air molecules occurs due to galactic cosmic rays and radioactive decay (for instance, by radon emitted from the ground) [37, 39]. Hydration plays important role in chemistry of ions that are formed in the D-layer of the ionosphere, between 60 and 90 km above the surface of the Earth. Solar activity UV and X-rays produce O_2^+ and N_2^+ ions from the air molecules, and NO^+ ions from NO. Formation of the protonated water clusters starts with hydration reactions of the ions O_2^+ and NO^+ resulting in a switch of the ionic core

$O_2^+(H_2O)_2 + H_2O \rightarrow H^+(H_2O)_2 + O_2 + OH$ and

$NO^+(H_2O)_2 + H_2O \rightarrow H^+(H_2O)_2 + HNO_2$

The produced protonated water cluster then grows by addition of other water molecules. Pure protonated water clusters dominate the stratospheric positive ion composition on heights 35–85 km above ground. Interestingly, there is a sharp decrease in abundance of $H^+(H_2O)_n$ above roughly 82–85 km in height and NO^+ as well as O_2^+ ions dominate the abundance of ions in this part of the atmosphere. This sharp atmospheric boundary is due to the fact that conversion of the primary NO^+ and O_2^+ ions into the hydrated proton clusters requires stabilization by three-body collisions, while above about 85 km the probability of such an event is too low [2, 40].

Atmospheric aromatic amines have received major attention since the first ion composition measurements at ground level in 1983 [41, 42]. Schulte and Arnold identified pyridinium as the dominating ion in the free troposphere over Europe, using air-plane based instrumentation [43]. One of the recent measurements by Junninen *et al.* [44] at the SMEAR III station in Helsinki, show protonated poly(alkyl) pyridines to be one of the main positive atmospheric compound types. Beig and Brasseur reported [45] a kinetic modelling work on positive and negative cluster ions in the atmosphere. It was found that clusters of the type $H^+(NH_3)_m(\text{pyridine})_1(H_2O)_n$ could dominate the positive ion spectrum between 1 and 6 km above the ground. The sources of pyridinated compounds in the atmosphere are believed to be predominantly automobile exhaust, biomass burning, manufacturing and agricultural use, as well as coal tars and tobacco smoke [46]. The cluster ions are proposed to be formed from protonated water clusters, $H^+(H_2O)_n$. The high proton affinity of ammonia, pyridine, picoline and lutidine is a major driving force in these reactions.

The most abundant negative ions in the troposphere are I^-, HSO_4^-, CO_3^- and NO_3^--core families of ions (*e.g.* [47]). Negative atmospheric ion formation begins with attachment of a free electron to air molecules resulting in the formation of the ions O_2^- and CO_3^-. Sulphur dioxide (SO_2) may react with oxidizers in the atmosphere (mainly OH radicals) to form sulfuric acid (H_2SO_4). Further the $NO_3^-(HNO_3)_nH_2O$, $HSO_4^-(H_2SO_4)_nH_2O$ ions are formed by clustering and the subsequent reaction with H_2O. It have also been reported [48, 49] that methanesulfonic acid, CH_4SO_3, and malonic acid, $C_3H_4O_4$, which are more acidic than nitric acid, are capable of replacing NO_3^- in clusters provided that their abundance is sufficiently high.

As a short digression, the importance of proton transfer phenomena for atmospheric processes can be shown by the interesting example of reactions in polar stratospheric clouds (PSCs). These heterogeneous reactions on the surfaces of micrometer-size particles consisting mainly of inorganic acids and water are largely responsible for the seasonal ozone depletion, the “ozone hole”. The primary causes of this phenomenon are halogens of anthropogenic origin which catalyse the destruction of ozone. Halogens have long lifetimes in the stratosphere, but they are gradually converted into more stable and less chemically active forms, mainly HCl and chlorine nitrate, $ClONO_2$. When the polar winter temperatures drop below about –80 °C, the PSCs, consisting of microscopic particles containing water and nitric acid, form. The HCl and $ClONO_2$ may condense on these particles, and heterogeneous reactions on their surface occur, converting them back to active species. During the polar spring, when the temperatures rise again and the PSC’s evaporate, the halogens in their active form are returned to the stratosphere and produce, by their catalytic effect, the observed ozone depletion.

The experiments confirmed that chlorine nitrate $ClONO_2$ [50] reacts rather efficiently with both anionic and cationic clusters, being hydrolysed on the cluster surface:

$$OH^-(H_2O)_n + ClONO_2 \rightarrow NO_3^-(H_2O)_n(HOCl) \rightarrow NO_3^-(H_2O)_i + HOCl + kH_2O$$

The efficient formation of HOCl provided by $OH^-(H_2O)_n$ and its evaporation from the cluster may be of importance for the stratospheric reactions and ozone depletion.

At this point, both field and laboratory studies allow us to safely conclude at least one thing: neutral as well as ionic nucleation of sulfuric acid appears to be of undisputable importance for gas-phase nucleation, providing efficient mechanisms for atmospheric new particle formation under favourable conditions [51-53]. The interaction between sulfuric acid (including bisulfate and sulfate ions) and water molecules is therefore fundamental to our understanding how cloud droplets grow in their initial phase. Furthermore, sulfuric acid–water vapour mixtures are prime examples of multicomponent nucleation. Water alone cannot nucleate due to its high saturation vapour pressure, while the concentration of sulfuric acid in the atmosphere is too low to be of significance by itself. The strong attraction of these molecules to each other means that their binary mixture can nucleate even if the partial pressures of the individual components are too low for them to nucleate on their own. As sulfuric acid is a good proton donor and a very poor proton acceptor, it comes as no surprise that ion-induced sulfuric acid - water nucleation is observed primarily for negative ions (*e.g.* [17, 54]).

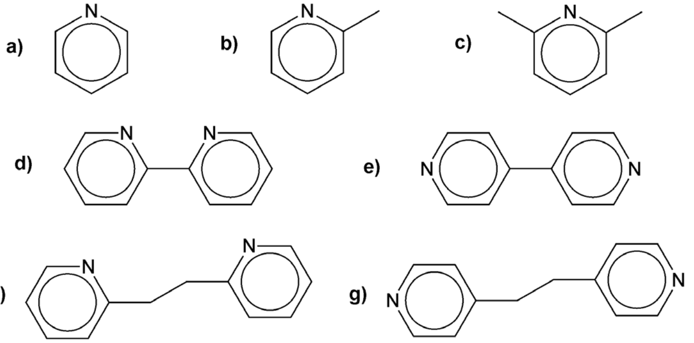

Figure 2. a) Pyridine, b) α-picoline, c) 2,6-lutidine, d) 2,2’-bipyridine (2,2’-BiPy), e) 4,4’-bipyridine (4,4’-BiPy), f) 2,2’-ethylenebipyridine (2,2’-EtBiPy), IUPAC name: 1,2-di(pyridin-2-yl)ethane, g) 4,4’-ethylenebipyridine (4,4’-EtBiPy), IUPAC name: 1,2-di(pyridin-4-yl)ethane.

In addition, amines are believed to be important in both neutral and ion-induced nucleation mechanisms [45], while ionic pyridinated compounds have been found to be present in the atmosphere [44, 55]. Pyridine is also an interesting tropospheric compound in light of the previously mentioned results of Kurtén *et al.* [30] indicating that amines other than ammonia might have a large impact on ternary nucleation processes of both neutral and charged clusters. Therefore studies of hydration of derivatives of sulfuric acid and amines are highly relevant from multiple viewpoints. As far as our study deals with a series of pyridine derivatives, their structures are given on the Figure 2.

2.2 Experimental studies of clusters

Section 2.2.1 offers a brief discussion of general considerations regarding experimental studies of clusters. Then a short introduction on commonly used experimental approaches of cluster studies is provided in Section 2.2.2.

2.2.1 General experimental considerations

Experimental studies of nanometer-sized clusters present some distinct complications. A typical instrument employed for detection of aerosols is the Condensation Nuclei Counter (CNC), in which an organic solvent is condensed on the particles to make them grow before being counted by a laser. Most commercial CNC systems have a lower detection limit of around 3 nm due to diffusion losses and insufficient nucleation by smaller particles (although there are instruments that can go lower in size range), see for instance [32]. On the other hand, if a research is focused on ionic clusters, there are large possibilities to transport, store, and detect charged species with masses ranging from few up to several thousand atomic mass units (u), so the above-mentioned problems vanish. Many of these techniques require high vacuum, which in itself is generally an attractive prospect: transport is easier, less side reactions with background gas, *etc.*

Further, hydrogen bonding and constant thermal motion complicate a determination of the detailed structure of bulk hydrogen-bonded systems. Additionally, the hydrogen-bonded vibrations are strongly coupled to the low-frequency local motions. Experimentally this leads to featureless spectral lines partially due to the intrinsic broadening of the states in the condensed phase, partially to extensive averaging over time and space. For instance, high-resolution studies of neutral water clusters in the far-infrared reveal very complex spectra due to multiple minima potentials and extensive proton exchange motions.

Fortunately, most of these effects are substantially reduced in small clusters, which are still capable of providing valuable insights into the structure and properties of the bulk. Finite clusters are easier to study [40, 56], also they are also more feasible to theoretical *ab initio* modelling. Studies of ionic water clusters, solvated ions, and their reactions have demonstrated that small “nanodroplets” with up to a hundred water molecules can also provide a medium for investigating a wide variety of aqueous reactions. In particular, mass-spectrometric methods are particularly useful in providing numerous valuable insights in studies of processes of atmospheric relevance dealing with clusters of such small size range.

Next, one can imagine two conceptually opposite practical approaches for generating water clusters. First, a solution can be dispersed into small droplets whose size can then be further reduced by evaporation. Probably, the most prominent of the “dispersive” techniques in the laboratory practice is the electrospray method, [57, 58] discussed in Section 3.1.1. Conversely, one can begin with a single atom, molecule, or ion acting as a nucleus, and grow under proper conditions a cluster with the water or other ligands around it. The “aggregating” experimental methods mostly employ supersonic expansions. When a high-pressure gas expands adiabatically into vacuum, the temperatures in the system descend quickly. Eventually the gas becomes “supersaturated”, and spontaneous nucleation can occur. Usually the expansion of the gaseous substance is not used alone, but, for instance, nucleation centers, such as ions, are provided [40, 59].

2.2.2 Mass-spectrometric techniques in cluster studies

There exist various mass-spectrometric methods for investigating unimolecular and ion–neutral reactions, with numerous possible derivatives, combinations, and modifications; some are shown in Figure 3 [40, 60]. Each of these experiments proceeds under different conditions and yields slightly different information.

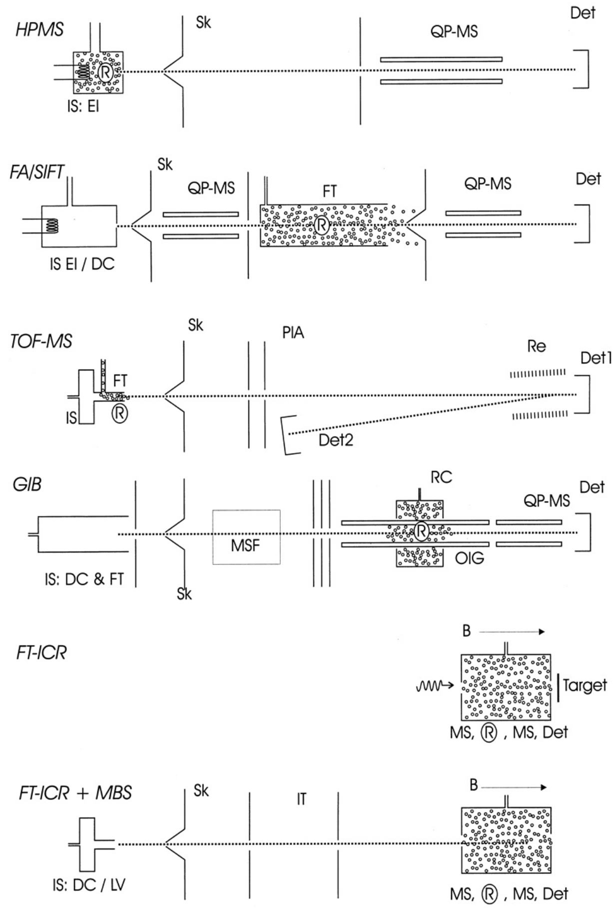

Figure 3. Schematics of some methods used in ionic cluster studies: a) HPMS, high-pressure mass spectrometry; b) FA/SIFT, flowing afterglow/selected-ion flow tube; c) TOF-MS, time-of-flight mass spectrometry; d) GIB, guided-ion beam; e) FT-ICR, Fourier transform ion cyclotron resonance. Abbreviations: MBS, molecular beam source; IS, ion source; EI, electron impact; Sk, skimmer; DC, discharge; QP–MS, quadrupole mass selection; FT, flow tube; Re, reflectron; Det, detector; MSF, magnetic sector field; OIG, octupole ion guide; RC, reaction cell; B, magnetic field vector; ®, location of reactive encounters; IT, ion transfer; LV, laser vaporization; PIA, pulsed ion acceleration. Reproduced with permission from [40], copyright 2000 American Chemical Society.

In high-pressure mass spectrometry (HPMS) [61], the reactions occur at relatively high pressures (1–10 mbar) hence collisions are frequent. Neutral reactant is typically in great excess of the ion concentration, and the pressure and temperature in such experiments are well defined, allowing to derive equilibrium constants for addition and switching reactions from such experiments. Examples of successful uses include measurements of the binding energies of the hydrated $H^+(H_2O)_n$ (n = 1–8) [62], studies of ionic water clusters [63-65], as well as investigations of water cluster reactions of species with atmospheric relevance, such as nitrogen oxides or acetonitrile [66-68].

Selected-ion flow tube (SIFT) [69] experiments provide better selectivity by the ability of mass-selection of the primary ions as a first phase. Thus only the selected ionic mass is injected into the reactor, which facilitates identification of the nature of product ions. On the other hand, the injection of ions may require high energies, so a good temperature definition could be lost. The higher energies can also result in altered reactivity and fragmentation and thus complicate the interpretation of the results. This technique was, for example, used to investigate reactions of the hydrated protons $H^+(H_2O)_n$, n = 2–11, with a set of gaseous reactants including methanol, ammonia, or acetonitrile [70].

Next, in a guided-ion beam techniques (GIB) the ions are guided through the reaction cell with a thermal energy distribution (*e.g.* [71]). The main advantages of the technique are elimination of ion loss and ion reactions on the cell wall, and an efficient ion collection, all resulting in higher accuracy for total cross-section measurements. Properties such as dissociation thresholds, branching ratios of dissociation reactions and kinetic energy release upon dissociation can be determined with this type of instruments. The binding energies can also be determined in a collision-induced dissociation (CID) experiment, as was, for instance, done for $H^+(H_2O)_n$ (n = 2–6) clusters [72].

In all the above methods the reactant kinetic energies have relatively broad distribution. In a next kind of investigation, using carefully designed ion optics it is possible to define kinetic energy of the selected-ion beam. In such experiments velocity of the reactant ions relative to the reactants can be varied and the rate coefficients are determined as a function of the ion energy. In the simplest implementation, the ion beam interacts with a low-pressure neutral gas in a static reaction cell. A crossed beam experiment, where the velocity of the neutral reactant is also now uniform, is a further improvement but leads to a substantial loss in signal intensity.

Experiments on electrically and magnetically trapped ions can yield essentially the same type of information that can be obtained in beam experiments. In Fourier transform-ion-cyclotron-resonance, FT-ICR mass spectroscopy [73] the ions in the field of a strong magnet are confined in an ultrahigh vacuum radially by the Lorentz forces resulting in a spiral “cyclotron” motion. The main advantages of the FT-ICR MS are long observation times, ultra high resolution and high mass accuracy. If not controlled, unwanted hyperthermal energies of the ions can be a disadvantage of this method. The maximum kinetic energy can be controlled by adjusting the voltage of the “trapping” electric field confining the ions axially.

In investigations of metastable fragmentation of hydrogen-bonded systems ionic clusters may be prepared by electron impact ionization or photoionization of the neutral species in molecular beams. Such ionization produces ions with elevated internal energy, often leading to their consequent dissociation on a microsecond time scale. The products are then detected in a “reflectron”, a type of time-of-flight mass spectrometer, TOF-MS, in which an electrostatic field is used to reflect the flight of ions. In such an experiment the metastable parent ions are all initially accelerated to the same velocity in the source, but the product ions have reduced kinetic energies and are therefore differently affected by the reflecting field and can thus be easily mass-analyzed and identified. The fragmentation patterns as well as the mass peak line shapes of the daughter ions provide useful insights into the cluster ion structure, stability, and rate of ligand loss [74, 75].

In another mass spectrometry technique, mainly used for characterization of metastable and collision-induced dissociation of ions, mass-analyzed ion kinetic energy spectrometry (MIKES), mass spectra are obtained on a sector instrument that combines at least one magnetic sector plus one electric sector [76-78]. The precursor ion with a particular mass-to-charge ratio *m/z* is selected using the magnetic sector, and then allowed to dissociate or react in a field-free region between the two sectors. The shapes of the product ion spectrum peaks analyzed in electric sector scan are related to the kinetic energy release distribution for the dissociation process and to the kinetic energy uptake for the ionic collision process.

2.3 Theoretical methods used to study clusters

In this chapter we discuss the theoretical methods that can be employed in cluster studies. They can be classified into three groups depending on the level of the underlying approximations and scale at which the interactions between the components are treated.

1. In classical nucleation theory the macroscopic properties of the participating compounds (surface tension, saturation vapour pressure, molecular volume) are used to describe the microscopic interactions. This theory is beyond the scope of present work, for a review see *e.g*. [79].

2. In methods based on classical interaction potentials specially designed force fields are used to describe the interactions between molecules, explicitly avoiding accounting the electrons or taking quantum mechanical effects into consideration.

3. In quantum chemistry simulations the interactions between constituents are computed by solving the Schrödinger equation (or related sets of equations) for the motion of electrons in fields of nuclei.

As a note, the popular "Car-Parrinello" molecular dynamics techniques [80] allow to perform theoretical treatment of water, ice, and, in particular, proton transfer events, with describing the structure and energetics of the hydrogen bonds in the presence of fluctuations, which is impossible within the Born-Oppenheimer approximation (Section 2.3.2). The basic concept includes the calculation of the forces that act on the particles directly out of the electronic structure during the simulation—instead of gaining this from potentials that were parameterized beforehand as force fields. Using the Car-Parrinello method, the forces are determined once at the beginning of the simulation, while later the ion propagates itself like a wave with its electrons. The electron follows the ion quasi-adiabatically, without an exchange with its environment. Realizations of this basic concept combine molecular dynamics with a first-principles description.

Thus we begin the present chapter by discussing force field methods (Section 2.3.1). This part is followed by an introduction of the basics of quantum chemistry (Section 2.3.2) and a more detailed description of ab initio methods, including correlated methods (Section 2.3.3). After a short discussion of density functional methods (Section 2.3.4), we will then briefly review the common basis sets (Section 2.3.5). Section 2.3.6 *concludes the chapter by providing general considerations and comments on theoretical studies of clusters, with a particular focus on practicability and accuracy.*

2.3.1 Force field methods

In this type of simulations molecular interactions are treated in terms of a force field, fitted to experimental or computational data [81, 82]. In spite of abundance of force fields in use today, most common of them share common characteristics with respect to the forms of description of the different interactions. Intramolecular parameters can be kept rigid during calculations, but generally the bond and angle terms are modelled as harmonic potentials centered on equilibrium values derived from experimental data or electronic structure calculations. Nonpolar interactions are typically described by Lennard-Jones terms. Electrostatic interactions between different molecules are treated using Coulomb terms. The potential energy for a system of particles is obtained by summing over all the different contributions.

Within this group of force field methods there are two main approaches: molecular dynamics (MD) and Monte Carlo (MC) simulations. The central idea of both molecular dynamics and Monte Carlo simulations is to allow a limited number (usually 10–10^4 units) of molecules to move according to the laws of classical mechanics for a certain amount of simulation time. The force acting on each functional group is computed from the force field. The disadvantage of MD compared to MC is that all the forces must be calculated at each individual step, which is time-consuming. In MC simulations, particles are arranged randomly at every step, and only the total energy of the system (rather than the forces) is computed and compared before and after each step. If the energy is lower after the random step, the new configuration is always accepted. If it is higher, the new configuration is accepted with a probability $e^{-\Delta E/k_B T}$, to ensure that the generated distribution of configurations follows the Boltzmann distribution. Typically, MD or MC simulations are performed either under conditions of constant particle number, volume and energy (called NVE, or microcanonical ensemble simulations) or constant particle number, volume and temperature (called NVT, or canonical ensemble simulations).

The major advantage of the methods based on classical potentials is that they are computationally cheaper than quantum chemical calculations, allowing the study of larger systems on longer timescales. The main disadvantage is that classical potentials are rarely transferable—a potential developed for a certain type of molecule in one environment will not necessarily predict its interactions correctly in a different environment. Furthermore, most force fields are by construction unable to treat non-equilibrium properties.

2.3.2 Quantum chemical methods, general information

Quantum chemistry is the branch of chemistry with primary focus on computing the properties of a system by applying quantum mechanics to evaluate the interactions between the nuclei and electrons. As computational resources are limited and size of systems of interest can be rather big, the main objective is to find approximate solution of Schrödinger equation. The approximations can be made in several of different ways, giving rise to a multitude of computational approaches, also known as "model chemistries" [82, 83].

The non-relativistic time-independent Schrödinger equation reads

$$\hat{H}\Psi = E\Psi \tag{2.1}$$

where $\hat{H}$ is the Hamiltonian operator of the system, E is its energy, Ψ is total molecular wavefunction. The Hamiltonian operator can also be written as

$$\hat{H} = \hat{T}_n + \hat{T}_e + \hat{V}_{ne} + \hat{V}_{ee} + \hat{V}_{nn} \tag{2.2}$$

where the first two terms present the nuclear and electronic kinetic energy operators, plus the three types of potential energy operators, corresponding to nuclei-electron, electron-electron and nuclei-nuclei interactions, respectively.

In nearly all studies on polyatomic systems, the Born-Oppenheimer approximation is used to split the wavefunction into electronic ($\chi(\mathrm{r}_{nuc})$) and nuclear ($\Phi(\mathrm{r}_{el})$) components

$$\Psi(\mathrm{r}_{el}, \mathrm{r}_{nuc}) = \chi(\mathrm{r}_{nuc})\Phi(\mathrm{r}_{el}) \tag{2.3}$$

The Born-Oppenheimer approximation originates from in the great difference between masses of electrons and nuclei. Because of the difference, electrons are assumed to react instantaneously to displacements of the nuclei. From the point-of-view of the electrons, the nuclei can thus be treated as classical point masses. The electronic wavefunction still depends on the nuclear positions, but only parametrically–the electronic wavefunction can be solved separately for each given nuclear configuration.

The Born-Oppenheimer approximation is very reliable for calculations of electronic ground states, although it is less reliable for excited states.

There exist two main families of methods capable of providing electronic energies accurate enough for energetic and structural predictions. The *ab initio* methods first iteratively solve the Schrödinger equation for electronic wavefunction $\Phi(\mathrm{r}_{el})$ for a system of electrons that move in each other's static average potential. This so-called Hartree-Fock wavefunction does not include the effects of correlation, and it can subsequently be improved upon. The other approach is density functional theory (DFT) pioneered by Hohenberg and Kohn [84] and developed by Kohn and Sham [85], in which the Schrödinger equation is reformulated in terms of the electron density, and exchange and correlation interactions are included via an exchange-correlation functional.

2.3.3 Ab initio methods

In *ab initio* methods, two major approximations to the form of the electronic wavefunction have to be made before the Schrödinger equation can be solved. The first main step is to describe the (3*N*-dimensional) electronic wavefunction in terms of a set of one-electron spin orbitals. The most common expansion is the Slater determinant:

$$\Phi(\mathrm{r}_{el}) = \frac{1}{\sqrt{n!}}\begin{vmatrix} \phi_1(\mathrm{r}_1) & \cdots & \phi_n(\mathrm{r}_1) \\ \cdots & & \cdots \\ \phi_1(\mathrm{r}_n) & \cdots & \phi_n(\mathrm{r}_n) \end{vmatrix} \tag{2.4}$$

where n is the number of electrons in the system and $\phi_n(\mathrm{r}_n)$ are the one-electron spin orbitals. Slater determinant is the simplest combination of one-electron orbitals that fulfils the requirement of the Pauli exclusion principle that the electronic wavefunction is antisymmetric with respect to the exchange of two electrons. In spin-restricted calculations, the spatial components of the spin orbitals are assumed to be identical for each pair of electrons. In spin-unrestricted calculations, two complete sets of molecular orbitals are used for α and β spin electrons.

The Schrödinger equation solved for a single Slater determinant yields the Hartree-Fock wavefunction. If desired, further determinants corresponding to various electronic excitations can then be generated from it. Accurate treatment of some systems such as biradicals may require the use of multireference methods. In multi-configuration self-consistent field method, a set of coefficients of both the determinants and the basis functions are varied to obtain optimal total electronic wavefunction. Since multireference methods have not been used in any of the papers included in this thesis, they will not be treated further here.

The second major approximation regards the basis-set expansion, in which each one-electron spin orbital is expressed as a linear combination of basis functions f_j:

$$\phi_i(\mathrm{r}_i) = \sum_{j=1}^{m} c_{i,j} f_j(\mathrm{r}_i) \tag{2.5}$$

where $c_{i,j}$ are called orbital expansion coefficients. A brief introduction regarding basis set concept is presented in a Section 2.3.5.

The solution of the electronic wavefunction is based on the variational principle, which states that any approximate solution to the Schrödinger equation has an energy above or equal to the exact energy (see *e.g.* [82]). Thus, the set of coefficients $c_{i,j}$ that give the best approximation to the true ground-state energy and wavefunction are those that minimize the energy, so that for every $c_{i,j}$

$$\frac{\partial E}{\partial c_{i,j}} = 0 \tag{2.6}$$

Application of the variational principle to a single-determinant wavefunction leads to a set of Hartree-Fock equations, which for practical calculations must be converted into the Roothan-Hall equations. In a matrix form these are

$$\mathbf{FC} = \mathbf{SCE} \tag{2.7}$$

where **C** is the matrix of orbital expansion coefficients (see equation 2.5), **E** is a diagonal matrix containing the orbital energies ε_i, and **F** and **S** are called the Fock and overlap matrixes, respectively.

However, as the wavefunction and energy of each electron is dependent on the wavefunction and energy or every other electron, the Roothan-Hall equations must be solved iteratively, starting out from some initial guess trial wavefunction. The trial wavefunction can be used to compute a new, improved set of orbital expansion coefficients and a new **F** matrix. Repeating the process is done until convergence yields the Hartree-Fock energy and wavefunction. In most applications, the Roothan-Hall equations are not solved in straightforward fashion. Instead, various sophisticated algorithms are used to reduce the number of iterations (or the computational time and/or memory) required for convergence. In practice the scaling factor (the factor by which the computational cost grows as a function of the system size) of the Hartree-Fock methods is usually close to N^3 (N is the number of basis functions) [82], what can be considered moderate.

As the HF approach assumes that each electron moves in the average potential of the other electrons, the correlation between the electrons is neglected, because the effect of the n–1 electrons on the electron of interest is treated in an averaged way. The electron correlation can be divided into dynamical correlation (caused by Coulomb repulsion between the electrons) and static correlation, which is related to systems which cannot be described correctly by a single determinant. While the correlation accounts for only a small fraction of the total energy, it is vitally important for accurate simulations of chemical reactions and bonding.

Several methods have been developed to include correlation within wavefunction theory: configuration interaction (CI), Møller-Plesset (MP) perturbation theory and coupled-cluster theory (CC). Despite their deep theoretical difference, all methods work in a similar way in terms of the wavefunctions. First, a Hartree-Fock calculation yields a set of occupied and virtual orbitals. Second, a set of additional Slater determinants is formed by substituting one or more occupied orbitals for virtual orbitals in the original Hartree-Fock determinant, and calculation continues. The number of simultaneous substitutions per Slater determinant is determined by the level of the method: singly excited Slater determinants contain only one substitution, doubly excited ones contain two and so on. Physically, this corresponds to exciting a number of electrons to higher energy levels.

In configuration interaction calculations the ground- or excited-state wavefunction for a specific state is represented as a linear combination of n-electron Slater determinants. Full CI corresponds to allowing all possible excitations, however, it scales as $N!$, and in practice the CI is restricted to single, double and triple excitations, for the CIS, CISD and CISDT methods, respectively. It should be noted that the CIS energy does not represent an improvement over the HF method. The truncated CI methods are not size-consistent, meaning that the energy calculated for a system is not equal to the sum of energies of its isolated parts. For this reason, CI methods are seldom used in energy calculations.

Møller-Plesset (MP) perturbation theory [86] is based on treating electron correlation as a small perturbation of the HF Hamiltonian:

$$\hat{H}_{M-P} = \hat{H}_{HF} + \lambda(\hat{V}_{ee} - 2\langle\hat{V}_{ee}\rangle) \qquad (2.8)$$

where $\hat{H}_{HF}$ is the Hartree-Fock Hamiltonian operator, λ is an arbitrary constant, $\hat{V}_{ee}$ is the potential energy operator corresponding to electron-electron interactions (see equation 2.2) and the "$\langle\quad\rangle$" brackets indicate an expectation value. The expression for the n-th order perturbative energy and wavefunction can be obtained from perturbation theory. The methods are indexed as MPn by the level of perturbation. It can be shown that, just like for CI, the first real improvement over the ground state HF energy is given by the second order correction energy. MP2 scales as N^5, recovers around 90% of the correlation energy [82], and is the most cheap (and probably the most popular) correlated *ab initio* method. MP3 does not usually significantly improve upon the MP2 result. The only other perturbation-based method that is commonly used, MP4, recovers about 98% of the correlation energy, however it scales already as N^6.

Coupled-cluster methods [82] are based on the assumption that the wavefunction can be described as

$$\Psi_{CC} = e^{\hat{T}}\Phi_{HF} \qquad (2.9)$$

where Φ_{HF} is the HF reference configuration (the Slater determinant of equation 2.4) and cluster operator $\hat{T}$ is defined as $\hat{T} = \hat{T}_1 + \hat{T}_2 + \hat{T}_2 + \ldots + \hat{T}_n$, with $\hat{T}_1$ corresponding to single excitations, $\hat{T}_2$ to double excitations and so on. In practice, the cluster operator expanded in a Taylor series is truncated at some point by neglecting higher-order terms. The level of truncation is indicated by letter indexes. For example, CCD contains only double, CCSD both single and double, and CCSDT single, double and triple excitation operators. When HF wavefunction is a good basis, CCSD(T) (where the triple excitations are evaluated non-iteratively) is considered to be the state-of-the art method.

Unlike CI the CC methods and MP theory are size-consistent. The fraction of the correlation energy recovered (and the accuracy of the results) is significantly higher for CC than for MP methods of same order. Unfortunately, coupled cluster calculations are computationally expensive and extremely time consuming, with N^7 scaling. The studied water clusters are therefore clearly too large for these methods to be used, and the wavefunction-based methods are usually limited to MP2 at best. Alternatively, DFT methods proved to be cheap but still good solution, with scaling around N^3.

2.3.4 Density functional theory

The central tenet of the theory is the assumption that for an arbitrary system of electrons, moving in an external potential $V_{ext}(\mathrm{r})$, the ground state electron density $\rho(\mathrm{r})$ uniquely determines the external potential. Since the electron density also determines the total amount of electrons

$$N = \int \rho(\mathrm{r})\, d\mathrm{r} \tag{2.10}$$

it also determines the Hamiltonian of the system and thus its full ground-state wavefunction. The ground-state energy is therefore also a functional of $\rho(\mathrm{r})$. Since the functional for the ground-state energy is unknown, the electron density has to be expressed in terms of one-electron orbitals analogously to equation (2.4):

$$\rho(\mathrm{r}) = \sum_{i=1}^{N} |\phi_i(\mathrm{r})|^2 \tag{2.11}$$

with the one-electron orbitals further expanded in terms of a basis set just like in equation (2.5). The idea of expressing the electron density in terms of an orbital basis was first proposed by Kohn and Sham [85]. Analogously to ab initio methods, DFT methods can be either restricted or unrestricted depending on the treatment of electron spin. In the latter case the total density is expressed as a sum of two components, $\rho(\mathrm{r})_\alpha$ and $\rho(\mathrm{r})_\beta$.

Next the energy functional $E[\rho(\mathrm{r})]$ is expressed as

$$E[\rho(\mathrm{r})] = E_{ext} + E_{kin} + E_{coul} + E_{xc} \tag{2.12}$$

where the first term accounts for the interaction between the nuclei and the electrons, the second term is the kinetic energy of a noninteracting system of electrons with density $\rho(\mathrm{r})$, and the third term is the Coulombic repulsion between the electrons. $E_{xc}[\rho(\mathrm{r})]$ accounts for the exchange and correlation interactions, and it is the only unknown term in the functional. There is no systematic way to develop or even improve the exchange-correlation functionals in DFT; so various approximate forms similarly to HF calculation have to be used. Similarly to the variational principle, Hohenberg and Kohn [84] proved that the true ground-state density corresponds to a minimum value for the energy. According to Kohn and Sham, the best approximation to the ground-state density and energy is obtained by minimizing the energy with respect to the expansion coefficients of the Kohn-Sham orbitals. This leads to the set of *N* Kohn-Sham equations. In computational applications, the Kohn-Sham equations are solved like the Hartree-Fock equations–self-consistently, using linear algebraic techniques.

According to classification by Perdew [82, 87], exchange-correlation functionals can be divided into five rungs, according to the types of terms they contain as follows:

I. The first rung corresponds to LDA, the local density approximation, where $E_{XC}[\rho(\mathrm{r})]$ is approximated by the exchange-correlation energy of a homogeneous electron gas. While the performance of LDA is satisfactory for some metallic systems, it is useless for modelling gas-phase molecules.

II. The next step up are the generalized gradient approximation, or GGA, functionals, which in addition to terms proportional to $\rho(\mathrm{r})$ also contain gradient terms proportional to $\nabla\rho(\mathrm{r})$. GGA functionals are very popular, as they are relatively simple to evaluate and may provide near-chemical accuracy (often defined as an accuracy of 1 kcal mol^{-1} with respect to the reaction or binding energies of molecular systems).

III. The third rung corresponds to the meta-GGA functionals, which in addition to terms proportional to $\rho(\mathrm{r})$ and $\nabla\rho(\mathrm{r})$ also contain the second derivative of the density (or some related term), which is obtained from the occupied Kohn-Sham orbitals. This increases the computational cost, but may improve the correspondence with higher-level *ab initio* results or experimental data.

IV. The fourth rung presented by hybrid DFT functionals, which contain the Hartree Fock exchange interaction in addition to the above-mentioned components. Most hybrid functionals (such as the extremely popular B3LYP functional) contain both HF and DFT exchange components, with the exact fraction of each determined for example by fitting to experimental results.

V. In the classification the fifth rung corresponds to DFT functionals that include terms containing the unoccupied (virtual) Kohn-Sham orbitals. This allows the treatment of dispersion (non-local correlation) effects, which are underrepresented in level 1–4 functionals (see *e.g.*[88]). Alternatively dispersion effects may be included in form of dispersion correction schemes [89] and long-range corrections, as done for example in CAM-B3LYP [90].

2.3.5 Basis sets

The basis set is the set of mathematical functions from which orbitals are constructed. Several different types of basis functions have been developed for various tasks, but the most common choice is use of gaussian type orbitals (GTO)

$$f_{\zeta,n,l,m}(\mathrm{r},\theta,\varphi) = N_c Y_{l,m}(\theta,\varphi)\mathrm{r}^{(2n-2-l)}e^{-\zeta\mathrm{r}^2} \tag{2.13}$$

where N_c is a normalization constant, n, l and m are quantum numbers (see *e.g.* [81]), $Y_{l,m}(\theta,\varphi)$ is a spherical harmonic function and ζ is a constant. The co-ordinate system in equation (2.13) is normally atom-centered, and each atom type is normally represented by a certain number of basis functions. Slater-type functions, which resemble gaussian functions except that the exponential term is proportional to $-r$ instead of $-r^2$, are also used. Numerical grids fitted to the appropriate exact atomic wavefunctions, or plane waves, are also commonly used as basis sets, though they are rarely used for molecular cluster studies. Slater-type functions are exact solutions to the Schrödinger equation for isolated one-electron atoms. They show correct behaviour at the nucleus and a correct exponential decay with increasing r, and are therefore much more accurate *per basis function* than GTO. However, Gaussian functions are computationally much more efficient, therefore the majority of quantum chemical studies on gas-phase molecular systems use gaussian basis sets. A common procedure to reduce the errors appearing from the incorrect behaviour of the $-r^2$ - exponential term is to group several GTOs to form contracted Gaussian functions. Each contracted Gaussian is taken to be a fixed linear combination of the original or primitive Gaussian functions, centered on the same atomic nuclei.

The simplest type of basis set is a minimal basis set in which a single function is used to represent each electron pair or an electron. In most studies requiring accuracy, the basis set has to be larger than minimal, and two kinds of one-electron spin orbitals are generated: occupied and virtual. The virtual orbitals are used in the treatment of electron correlation.

The way to improve basis set is to increase the number of basis functions per atom. Double-ζ basis set contains two basis functions per electron pair, triple-ζ contains three, *etc*. Next, the basis functions describing valence orbitals involved in chemical bonding need more flexibility than basis functions for core orbitals. Thus additional basis functions are often added for the valence electrons only, while each inner-shell atomic orbital is represented by a single basis function, which leads to the valence double-ζ, valence triple-ζ, *etc*. Widely used basis sets arising from the group of John Pople can be presented as *X-YZg* for split-valence double-zeta basis set or *X-YZWg* for split-valence triple-zeta basis sets (*e.g.* 6-31G and 6-311G, consequently).

When bonds form in molecules, atomic orbitals are distorted (polarized) by adjacent atoms. Split valence basis sets allow orbitals to change size, but not to change shape. To improve the description of chemical bonding, polarization functions (corresponding to orbitals with higher values of the angular momentum quantum number) need to be added to the basis set. The addition of these polarization functions to *e.g.* double-ζ basis set results in a double-ζ plus polarization basis set. For common applications the number of polarization functions varies between one and four per atom. For accurate descriptions of weakly bound clusters, diffuse functions (corresponding to low values of ζ) are also often added to the basis set. Diffuse functions can be visualized as corrections for the too fast decay of the $e^{-\mathrm{r}^2}$ term in the gaussian basis functions far away from the nucleus as compared to the real $e^{-\mathrm{r}}$ decay of the exact one-electron orbitals. The corresponding erroneous behaviour of GTOs close to the nuclei is corrected for by the contraction procedure described above.

At this point it would be useful to discuss in more details the two most popular families of basis sets based on contracted GTOs: those of Pople and Dunning. The Pople style basis sets first include the STO-3G basis set, [91] a single-ζ basis set where each contracted GTO consists of 3 primitive Gaussian functions. As already mentioned, split-valence basis sets developed by Pople *et al.* include 3-21G, 6-21G, 4-31G, 6-31G and 6-311G where the first number indicates the number of primitives used in the contracted core functions and the numbers after the hyphen state the numbers of primitives used in the valence functions so two and three numbers indicate a valence double-zeta and triple-zeta basis set, respectively. Polarization functions are quoted by a star (*), diffuse functions by a plus (+), *e.g.* 6-311+G*. The second widely-used family of basis sets are the correlation consistent polarized valence *n*-zeta (cc-pVnZ) basis sets of Dunning and co-workers where *n* ranges over D (double) [92], T (triple) [93], Q (quadruple), *etc*. Correlation consistent implies that the exponents and contraction coefficients were optimised not only for HF calculations but also for use in calculations including electron correlation methods. In the Dunning family of *cc-pVnZ* basis sets, diffuse functions on all atoms are indicated by prefix "*aug*".

2.3.6 Practical considerations on quantum chemistry simulations

The level of theory needed for a computation depends both on the property of interest and the accuracy required [82]. Simple Hartree-Fock calculations with small basis sets are often enough to produce qualitatively reliable molecular geometries. For covalently bound systems, third- or fourth- generation density functionals with polarized valence double-ζ basis sets often give qualitatively very reliable molecular geometries and energies, though valence triple-ζ basis sets with multiple polarization functions may be required for quantitative accuracy. For weakly bound systems (such as the molecular clusters), pure DFT methods are less reliable, and dispersion corrections or correlated *ab initio* methods are sometimes needed. Unfortunately, post-Hartree–Fock methods have a very unfavourable scaling of the computational cost, while accurate energy calculations with correlated methods may require basis sets as large as quadruple-ζ or higher. On the other hand, in case of *ab initio* methods increasing the basis set will always increase the reliability of the results. This does not necessarily apply for DFT methods–there is no guarantee that the largest basis set corresponds to the best result. Indeed, as many DFT functionals have been parameterized using computations with modest basis sets, it is believed that medium-size basis sets are preferable for many DFT calculations.

The goal of a computational study is to obtain the maximum possible accuracy of the properties of interest with the lowest possible computational effort. The main task is then to choose the model chemistry (*i.e.* a combination of method and basis set) based on experience and knowledge of its strengths and weaknesses.

2.4 Cluster ions in the laboratory and calculations

Molecular clusters are highly interesting in their own right, since they represent an edge between single molecules and bulk. By using clusters as model systems, it is possible to study stepwise solvation mechanisms of ions, and to extract information on thermodynamic properties and dynamics. Kebarle [94] and Castleman [95] provided important chemical thermodynamic information about water clusters. The stability of charged water clusters in a given size range can be probed with molecular beam experiments.

Proton exchange reactions represent a special class of chemical reactions. Because of its fundamental importance as a model for ion- or ligand-exchange reactions [96] and in atmospheric chemistry [97] proton exchange in the gas phase as well as in bulk water has been thoroughly studied employing various experimental and theoretical approaches.

The present chapter opens with Section 2.4.1 that deals with size distributions of water-containing molecular clusters and discontinuities in them–magic numbers. Then we continue by discussing ion-molecular reactions with D_2O and a concept of proton/deuterium exchange (Section 2.4.2). Finally, we finish with a section on proton transfer, as studied by experimental and theoretical means (Section 2.4.3).

2.4.1 Clusters distributions, magic numbers

An abundance spectrum presents essentially a measure of abundances of clusters of different sizes in a produced distribution. Cluster abundances can be produced and measured in different experimental setups, and the distribution can have different properties. Figure 4 shows an abundance spectrum of pure protonated water clusters $H^+(H_2O)_n$, produced in the QTOF2 instrument (see Chapter 3). A distribution of water clusters like this one is formed by successive evaporation of water molecules from larger clusters.

Total intensity and overall shape of the reported cluster distributions—the width, height and curvature of the mass spectrum—are dependent upon experimental conditions: the cluster source conditions, instrument settings, concentration of the solution, *etc.*), *e.g.* [98]. In contrast, the fine structure of the distribution as well as "magic numbers" are dependent upon the properties of the specific clusters themselves; they appear in different experimental sessions and seem to persist under all experimental conditions used.

The question concerning the structure of ionic clusters has received a lot of attention, as evident from the many experimental and theoretical studies [40]. For example, the tetramer of protonated water, $H^+(H_2O)_4$, has a particularly stable trigonal structure corresponding to each of the three waters acting as hydrogen bond acceptors for the three hydrogens of the central hydroxonium ion. Evaporation of H_2O from $H^+(H_2O)_4$ therefore requires considerable energy, and Figure 4 reveals no peaks below $n = 4$, in agreement with this simple reasoning.

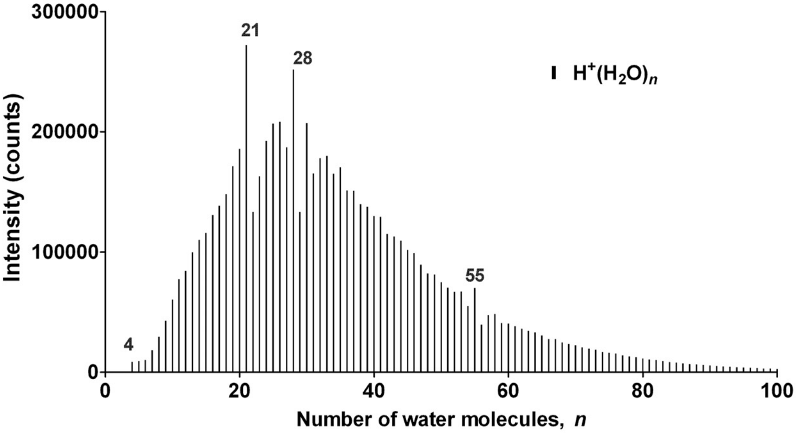

Figure 4. Abundance spectrum for pure water clusters $H^+(H_2O)_n$. The clusters with specific n are marked.

Next, the fine structure in the abundance spectrum of protonated water clusters in Figure 4 includes the so called "magic numbers", or ionic cluster signals with reproducible enhanced intensities with respect to the neighbouring intensities, with the most famous representative at $n = 21$. Magic number clusters are generally assumed to be thermodynamically or kinetically more stable than the average and less likely to fragment, which would make for their higher abundance. The magic number cluster $H^+(H_2O)_{21}$ was first noted by Lin [99], later confirmed in a large number of experiments, and has been the subject of high scientific interest since then. Experiments, even though confirming the anomalous behaviour and enhanced stability of the $n = 21$ cluster, gave no information about its structure. Originally it was treated in terms of a particularly stable dodecahedral clathrate structure of 20 water ligands around a central hydronium ion, with each of 20 oxygen atoms located in the corners of the ideal structure [100, 101]. This concept became the standard explanation for magic numbers in mass spectra of ionic water clusters, and has frequently been used to explain the magic numbers in the mass spectra of hydrated metal ions [102-104]. Further, reactions of the preformed protonated water clusters have shown that the $n = 21$ species can bind up to 10 dimethylamine molecules, presumably attached to the 10 dangling O–H bonds, in consistence with the proposed dodecahedral structure [105].

Upon closer look the "clathrate" dodecahedral structure explanation appears less convincing. Although water is well known to form clathrate solids with cage-like cavities, this enclosing of a "guest" occurs only under high pressure. Further, the "guests" in these clathrates are hydrophobic species, while the hydronium ion prefers to form strong bonds specifically to three water ligands. Lastly, quantum chemical studies have found that for $H^+(H_2O)_{21}$ a distorted dodecahedral structure is indeed stable, however, with several other compact structures at essentially the same energy and with all of them exhibiting 10 dangling O–H bonds [106].

Only recently, experimental studies and theoretical methods became powerful enough to provide interesting insights into the problem of the geometric structure of hydrated ions. Infrared spectroscopic studies of the free O–H stretching vibration of protonated water clusters have revealed that for the $n = 21$ magic number cluster, the frequency is the same for all water molecules, indicating that they are all bound in equivalent positions. However, the $n = 22$ cluster shows the same signature, and does not exhibit special stability [107, 108]. Iyengar *et al.* performed atom-centered density matrix propagation dynamics at the DFT level and showed that the proton is not attached to a water molecule encapsulated inside the dodecahedron but is integrated into the surface of the cage, while the ideal dodecahedron arrangement is significantly distorted [109]. *Ab initio* investigation performed by Kus *et al.* has indicated that in addition to the dodecahedron structure, other equally stable and relevant energy structural forms may also exist [110]. When discussing preferred geometrical configurations, it is important to remember that it is difficult to make a clear distinction between the structural and fluctuant dynamical features due to the low energy constraints for rapid rearrangement of the hydrogen bond network between the energetically allowed forms [109, 111]. In addition, the increased abundance of $H^+(H_2O)_{21}$ can to some degree be explained by decreased dissociation energy of the next larger cluster $H^+(H_2O)_{22}$ which will then have a larger tendency to evaporate and form the magic number entity [112].

Extending the hydrated proton studies to larger clusters has clearly revealed a distribution anomaly for the $n = 55$ cluster, which is almost as clear and prominent as that of the $n = 21$ structure (Figure 4). Any proposal of a concrete structure of the $H^+(H_2O)_{55}$ ion would naturally be speculative. As a note, relatively large amplitude of the abundance variations around $n = 55$ for the negatively charged water $OH^-(H_2O)_n$ clusters is also clearly observed [113].

Strong magic number behaviour among alkali-ion–water clusters [102, 103, 114], for instance stability of $M^+(H_2O)_{20}$ (with M = Li, K–Rb) has also been observed. A usual explanation, formation of cage inclusion compounds, in particular a dodecahedron of water molecules surrounding the cation for $n = 20$ appears to be inapplicable [115]. In the paper by Schulz and Hartke [116], the global minimum energy configurations of hydrated alkaline cations $M^+(H_2O)_n$, with M = Na, K, Cs, have been optimized. Among other structures, the authors do observe dodecahedral cages as local minima, but they do not explain the occurrence of magic numbers. For example, authors [117] completely reject the dodecahedron hypothesis, stating that, on the basis of global optimization using genetic algorithms and the TIP4P/OPLS model potential, the magic number $n = 20$ (but also others) observed in $K^+(H_2O)_n$ and $Cs^+(H_2O)_n$ are due to several different lowest-energy cage structures that are less susceptible to dissociation and association reactions, therefore having longer observed lifetime. Further, remarkable lack of magic numbers of $Na^+(H_2O)_n$ clusters, as compared to other alkali-metal–water clusters, according to experimental and theoretical investigations [118, 119], is believed to be due to unique structural features of these clusters. For instance, according to the results [117], due to the stronger "structure breaking" effect of sodium cation, the stable cage structures collapse quickly to very different off-centered structures. These three-dimensional networks follow totally different build-up principles in the case of $Na^+(H_2O)_n$ and hence do not show the magic number pattern of the other alkali-metal–water clusters, that favour formation of cage structures.

2.4.2 Cluster ions reacting with D_2O, H/D exchange

Gas-phase reactions of clusters with various other molecules have been extensively studied. Comprehensive information about the properties and reactivity of water clusters can be found in Refs. [40, 115, 120]. Ion-molecular reactions with H_2O, although appealing and promising for providing interesting insights, do not allow the detection of products, and reactions involving isotopic labelling are commonly used instead. Reactions with heavy water are particularly interesting and informative because they provide data on H/D isotope exchange. Fortunately the molecules D_2O and H_2O are similar from several points of view to consider any results of mentioned reactions as interchangeable with H_2O.

The experimental studies presented in this thesis mainly focus on the reactions between ionic aqueous clusters with ammonia and heavy water, performed in a cluster beam experiment.

The cross section is a concept that is related to the probability of collision or reaction between two interacting species in the gas phase, in our case between a molecule and a cluster. The cross section for collision between a cluster and a gas molecule can be written

$$\sigma = -\ln(I/I_0)/(cL) \qquad (2.14)$$

where I/I_0 is the ratio of the cluster abundance exiting and entering a volume, c is the concentration of the gas in the volume, and L is the length of the cluster's path through the volume (see *e.g.* [121]).

In case of the reaction of aqueous cluster ions with heavy water, the products formed have masses that are one or two atomic mass units (u) greater than the reactant ion, depending on whether one or two protiums are exchanged for deuterium. In an experiment, where the products are detected by their difference in mass-to-charge ratio relative the parent ion, it is convenient to refer to the abundance of a specific product as $I(m/z + x)$, where m/z is the mass-to-charge ratio of the parent ion, and x is the shift in mass-to-charge ratio of the product. We define the fraction of exchange to be the sum of normalized product intensities due to the reaction channels, $\Phi = \sum_x I(m/z + x)$.

A few comments may be in order at this point. In the physical meaning the cross section refers to the effective area perpendicular to the path of a photon, molecule or particle that constitutes the target for collision. The cross section is a somewhat abstract property depending not only on actual size of the target of the collision; it can also depend on other properties of both colliding particles. It should also be mentioned that there is a difference between the collision cross section, *i.e.* the probability of collision between two species, and the reaction cross section, *i.e.* the probability to have a reaction between the two, since a collision does not necessarily mean that a reaction will occur.

The first detailed account of proton transfer reactions within water clusters was given probably by Ryan *et al.* [96] who reported occurrence of H/D isotope exchange in ion/molecule reactions between H_3O^+ and D_2O in a crossed beam experiment. For example, they observed formation of H_2DO^+, an indication of that the encounter intermediate is capable of facilitating several proton/deuteron transfers to occur. Anicich and Sen [122] observed similar isotopic exchange in their Fourier transform ion cyclotron resonance experiments. Smith *et al.* [97] studied small protonated clusters $H(H_2O)_n^+$ ($n = 1–3$) reacting with heavy water in a selected ion flow tube instrument. They reported complete statistical distribution of H and D amongst the product ions and neutrals (H/D scrambling), however, as the result of successive cluster-ion/D_2O collisions rather than in one single encounter. Honma and Armentrout [123] performed energy resolved guided ion beam experiments of the types $H(H_2O)_n^+ + D_2O$ and the "mirror" system $D(D_2O)_n^+ + H_2O$ ($n = 1–4$), reporting extensive H/D exchange within systems studied. Yamaguchi *et al.* [124] using a similar experimental setup found that the cross section for H/D exchange decreases with collision energy for $n = 1–11$. Further, an FT-ICR study of proton transfer in ionic water clusters [125] confirmed statistical isotopic distribution for $H^+(H_2O)_n$, but reported absence of proton transfer in related water clusters, $(H_2O)_n^-$, $O_2(H_2O)_n^-$.

The reaction between the cluster and heavy water occurs involving a short-lived reaction intermediate [123, 124]. Addition of a D_2O molecule to the cluster leads to release of binding energy, which elevates the temperature of reaction intermediate. As a consequence, the reaction intermediate will decompose by evaporation of a molecule [126]. For a cluster of type $X^\pm(H_2O)_n$ the reaction can be written:

$$X^\pm(H_2O)_n + D_2O \rightarrow [X^\pm(H_2O)_n(D_2O)]^* \qquad (2.15)$$

The formed reaction intermediate decomposes in less than 1 μs [126]:

$$[X^\pm(H_2O)_n(D_2O)]^* \rightarrow X^\pm(H_2O)_n + D_2O \qquad (2.16)$$

$$[X^\pm(H_2O)_n(D_2O)]^* \rightarrow X^\pm(H_2O)_{n-1}(HDO) + HDO \qquad (2.17)$$

$$[X^\pm(H_2O)_n(D_2O)]^* \rightarrow X^\pm(H_2O)_{n-1}(D_2O) + H_2O \qquad (2.18).$$

While the first reaction pathway gives back the original reactants, the second and third pathways results in product clusters that have exchanged one or two of their protium atoms for deuterium, producing a mass increase in the product clusters of 1 u and 2 u respectively. Obviously, the reaction pathway (2.17) requires the formation of HDO molecules inside the cluster intermediate, and is a result of O–H bond activation and an intermolecular H/D exchange mechanism catalysed by the presence of a free H^+ or a proton hole in the cluster ([126] and Paper I, II). This process is believed to progress through a series of fast individual rearrangement steps on the time scale of 50–500 ps [111]; the barriers for rearrangements are quite low, and the rate coefficients appear to be nearly constant in the temperature range 150–300 K. If the lifetime of the intermediate is sufficiently long compared to the time scale of the intermolecular H/D rearrangements, a complete isotopic randomization may be achieved with respect to hydrogen. As a result when water molecule leaves, all three possible products—H_2O, HDO and D_2O—can be formed by this process. The expected abundances of for example product HDO can easily be calculated with combinatorics (Figure 6). For a cluster with $2n + 1$ protium atoms—like a pure protonated water cluster—the randomized abundance is $2/(2 + n)$.

The Reaction 2.18 can also occur in the absence of a free proton or hydroxide ion in the cluster, without any H/D rearrangements. The product is then formed through intact ligand exchange mechanism where D_2O enters the cluster and H_2O evaporates to form $X^{\pm}(H_2O)_{n-1}(D_2O)$. Since Reaction 2.18 can happen through both the H/D exchange mechanism and the ligand exchange mechanism, but Reaction 2.17 only by H/D exchange, it is possible to compare the relative abundance of the two products to the values predicted for a completely randomized intermediate, and determine which of the two exchange mechanisms is active in the reaction in question. In the present work, this is done by calculating the ratio κ_{HDO} relation of abundance of products from Reaction 2.17 and the products from Reaction 2.18. The κ_{HDO} ratio can be expressed as

$$\kappa_{\mathrm{HDO}} = \frac{I(m/z + 1)}{I(m/z + 1) + I(m/z + 2)} \tag{2.19}$$

If there are clusters of certain size allowing for complete hydrogen scrambling in the reaction intermediates, *i.e.* they do not react through ligand exchange, then the experimentally obtained value of κ_{HDO} will be the same as the one calculated from the probabilities for random emissions of molecules, *e.g.* Figure 6. If a fraction of the clusters reacts via ligand exchange, then the measured abundance of products from Reaction 2.17 will decrease and the measured abundance of products from Reaction

2.18 will increase, with the consequence that the value of κ_{HDO} will be lower than the randomized one. The κ_{HDO} value thus varies from 0 (for a cluster that reacts solely through ligand exchange (swapping a H_2O for a D_2O), up to a maximum value that corresponds to the κ_{HDO} for emission of a water molecule with random isotopic composition. The measured values for κ_{HDO} can then be used to gain some insight into, for instance, the proton mobility in the specific clusters. Honma and Armentrout [123] showed in experiments on the mirror reaction $D^+(D_2O)_n + H_2O$, for $n = 1$–4, that there were no indications of an isotope effect on the branching ratio of reaction pathway (2.17) to (2.18). Further, the authors of Ref. [126] performed careful theoretical analysis of possible contributions in isotope shifts, and reported that these factors must be negligible.

The methodology described above was used to interpret outcome of reactions of various ionic clusters with D_2O. Andersson *et al.* [126], using a modified QTOF mass spectrometer, reported the outcome of low energy (0.1 eV) collision reactions between $H^+(H_2O)_n$ ($n = 2$–30) and D_2O. It was observed that H/D randomization becomes close to statistically complete for larger clusters, while this is not the case for $n < 8$. This can be seen in Figure 5 by comparing the experimental curve for $H^+(H_2O)_n$ with the curve corresponding to a statistical loss of a water molecule from a cluster with complete H/D scrambling. On the basis of RRKM calculations this behaviour was attributed to a rapid increase in the lifetime of the intermediate $[H(D_2O)(H_2O)_n{}^+]^*$ with size, in agreement with results of Honma and Armentrout [123]. At the size of $n = 10$ the lifetime was estimated to be 1 µs, allowing for numerous H/D exchange reactions to occur within the cluster before it dissociates. On the basis of the RRKM estimates one obtain a rate coefficient of the order 10^8 s^{-1} for this process. In the same paper, H/D exchange in ammonia-containing protonated water-clusters reacting with heavy water was also investigated. For any value of n, the total cross sections for reaction of D_2O with $NH_4(H_2O)_{n-1}{}^+$ or $H(H_2O)_n{}^+$, were essentially the same. However, the former cluster reacted mainly by ligand exchange (intact H_2O for D_2O). The absence of H/D exchange in the ammonia containing clusters was attributed to the lack of movable protons resulting from the persistence of an $NH_4{}^+$ core.

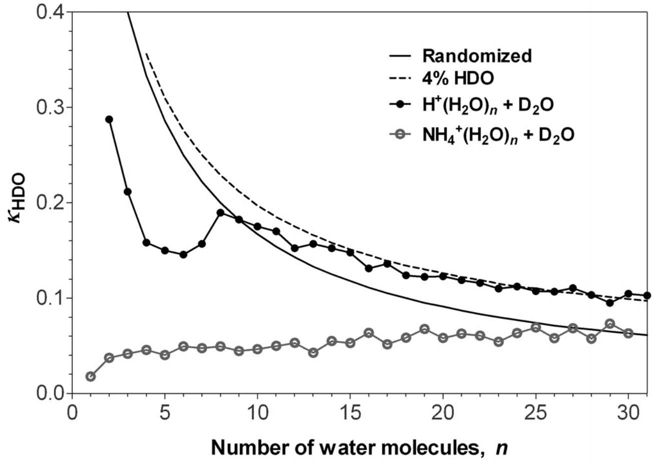

Figure 5. The ratio κ_{HDO}, being the fraction of products where a HDO molecule leaves the reaction intermediate after addition of D_2O to the clusters $H^+(H_2O)_n$ and $NH_4^+(H_2O)_n$. The statistical line corresponds to the expected value for a cluster having complete hydrogen scrambling, also corrected for background contaminations in the collision gas. Based on data from [126]

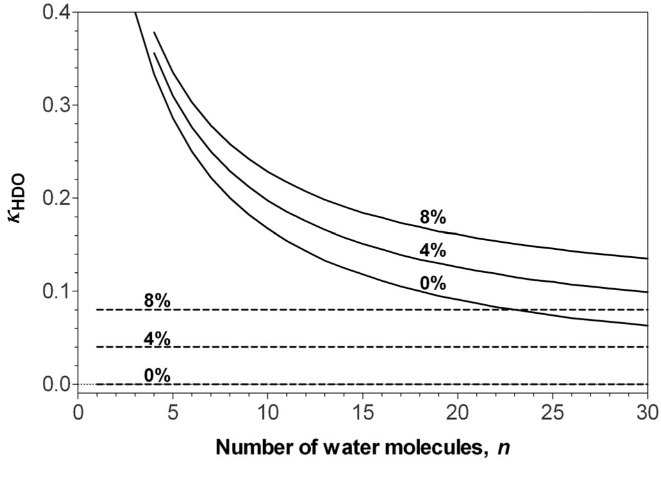

Figure 6. Values of κ_{HDO} for protonated water clusters reacting with D_2O through: H/D exchange mechanism (solid lines), and ligand exchange mechanism (dashed lines) calculated for 0%, 4%, and 8% HDO contamination in the D_2O collision gas. Courtesy of Dr. M. J. Ryding.

When performing experiments $X^{\pm}(H_2O)_n$ + D_2O, main concern is possible contamination of the D_2O gas by HDO. The presence of HDO makes it difficult to discriminate between proper H/D exchange due to O–H bond activation according to Reaction 2.17 and ligand exchange according to the reaction $X^{\pm}(H_2O)_n + HDO \rightarrow X^{\pm}(HDO)(H_2O)_{n-1} + H_2O$. The measured κ_{HDO} value will increase from its actual value to a value reflecting the degree of contamination. In case of a cluster that reacts by ligand swap, if 4% of the gas phase D_2O molecules are in fact HDO, then 4% of the abundance $I(m/z + 2)$ will be detected as $I(m/z + 1)$ and the κ_{HDO} value will be 0.04. For the type of cluster that supports complete hydrogen scrambling, expected values for κ_{HDO} can be estimated using combinatorics for different degrees of contamination, as can be seen in Figure 6.

Other issue that must be considered is the possibility of double collisions. It is clear from Reactions 2.15-2.18 that the experiment assumes that the cluster experiences only one reaction with D_2O. However, it is in principle possible for the product clusters of Reactions 2.16-2.18 to collide with another molecule on their flight through collision cell. As will be explained in the Chapter 3.1, the pressure of D_2O can be kept low in order to minimize double collisions. In short terms, using same combinatorics it is possible to show that the majority of clusters experiencing a second collision will not influence the κ_{HDO} value in the way it is estimated in our work.

In essence the reaction between the ionic aqueous cluster and D_2O can be seen from the viewpoint of different timescales. The relationship between the H/D rearrangement timescale (which is of the order of 10^2 picoseconds [111]) and the intermediate lifetime (of microsecond order [126]) serves to establish possibility of occurrence of a complete hydrogen scrambling before evaporation. H/D rearrangement timescale may include several individual proton transfers, which occur on femtosecond scale [127]. Another consideration concerns the evaporation of the cluster, which should be slow enough process, compared to the intermediate lifetime, or the experiment (Reactions 2.15-2.18) would otherwise be meaningless by this design. On the other hand, the intermediate's lifetime should also be so short that evaporation will occur during the experimental timescale, since detection of the intact reaction intermediate would not yield information on the degree of hydrogen scrambling. Experimental timescale (time from selection of a particular cluster size to detection of products) is of the order of 10^2 μs.

Since the cluster velocity through the cell varies as the square root of the reduced mass when the center-of-mass energy is kept constant, the experimental timescale is essentially the same for all cluster sizes in the investigated range.

2.4.3 Proton transfer from experiment and calculations

Historical retrospective shows that experimental and theoretical methods may be exceptionally useful in rationalizing proton transfer events both in bulk systems and in clusters. In one of the first endeavours in the field, Goldschmidt and Udby proposed that the extra proton is attached to a water molecule [128], in the form of H_3O^+ now known as the hydroxonium ion. Mann *et al.* fulfilled the first experimental verification of the idea of hydroxonium ion in the gas phase in 1940 [129]. Since then, a large number of studies on behaviour of H_3O^+ and its associations with water have been performed. Eigen suggested the importance of proton migration dynamics and the role of the three waters of the first hydration shell around the hydroxonium ion [130], while Zundel suggested the central role of the proton bonded dimer on the basis of spectroscopic evidence [131].

However, the molecular details of fast proton migration in water were outlined much earlier by Grotthuss in 1806 [132], although in an intuitive manner. The Grotthuss mechanism can be defined as “a sequence of proton transfer reactions (proton hops) between water molecules”. It is described as “structural diffusion of excess protons (protonic charge defects) in a hydrogen-bonded network”, which can not be fully described as an individual entity (*e.g.* H^+, H_3O^+ or OH^-) migrating through the network [127, 133]. The idea that proton transfer occurs through a hydrogen bond network has been elaborated over many times since then.

The mechanism deduced from experiments [133] and observed in the simulations [134] can be presented as incoherent step-by-step proton migration from one water molecule to the next and involves a “special pair dance” of water molecules in the solvation shell of the proton. According to this mechanism the motion of the proton more resembles gliding than hops between water molecules. The elementary process is initiated by the rupture of a hydrogen bond in the second solvation shell and detachment of single water molecule followed by addition of another molecule to the second solvation shell from the other side. As a result, the proton is displaced from the original central H_3O^+ and transferred to the neighbour H_2O. This type of process involves oscillation between Eigen ($H_9O_4^+$) cations through Zundel ($H_5O_2^+$) cations as an intermediate. Proton transfer characterized by this mechanism was estimated to occur at a rate corresponding to a characteristic lifetime of 1 ps [135, 136].

In spite of the fact that Grotthuss mechanism is strongly modified nowadays [133, 134, 137], the mechanism in its original form still may provide a formal model useful for proton transfer rationalization [138], especially in acid–base chemistry [139, 140]. For ionic reactions occurring in the isolated gas phase it has been shown that water molecule rearrangements are related to reactions like proton transfer [141-143]. In addition, a reaction may be catalysed by water mediated proton transfer from one local site having lower proton affinity than water to one having higher. Elementary steps of proton transfer process can be studied by applying suitable mass spectrometric methods to ionic water clusters, in combination with analysis of cluster size trends in hydrogen/deuterium isotope exchange rates.

Theoretical work by Mella and Ponti shows how reactions with D_2O can be used to gain insight into proton transfer phenomena. Molecular-dynamics simulations done using the OSS2 force field propose the mechanistic details of the H/D exchange process during an encounter between the reacting species [111], a process summarised as:

$H(H_2O)_n^+ + D_2O \leftrightarrows [H(H_2O)_n(D_2O)]^* \rightarrow H(HDO)(H_2O)_{n-1}^+ + HDO$.

The following order of events was observed in the simulations upon reaction (Figure 7): a) formation of the collision intermediate $[H^+(H_2O)_nD_2O]^*$; b) consecutive molecular shifts that eventually integrate the D_2O molecule in the region of the proton containing cluster core in the form of an Eigen tetramer $(H_2O)_3(HD_2O)^+$ or a Zundel dimer $(D_2O\text{–}H\text{–}OH_2)^+$; c) additional molecular shifts and displacement of a D^+ from the $(HD_2O)^+$ core to a neighbour H_2O molecule; d) successive molecular shifts bringing a HDO molecule to the periphery of the cluster; e) loss of the HDO molecule.

Two very interesting points of this mechanism is the fact that the shifts that occur by a single water molecule swinging from one position to the next (always being connected via at least one hydrogen bond) have small activation energies, and that the key proton/deuteron transfer hardly require any significant activation energy. Regarding the latter, it is a well-known fact that in the Zundel dimer the proton is mid-way between the two oxygen atoms. This observation is in good accord with Car–Parrinello simulations of proton migration in bulk water [144]. Furthermore, the simulations of Mella and Ponti indicate that isomerisation due to water shifts occur on the time scale 50–500 ps at room temperature, thereby not always allowing for full statistical energy randomization [111]. The rate of water shifts was found to increase upon increasing the size of the cluster.

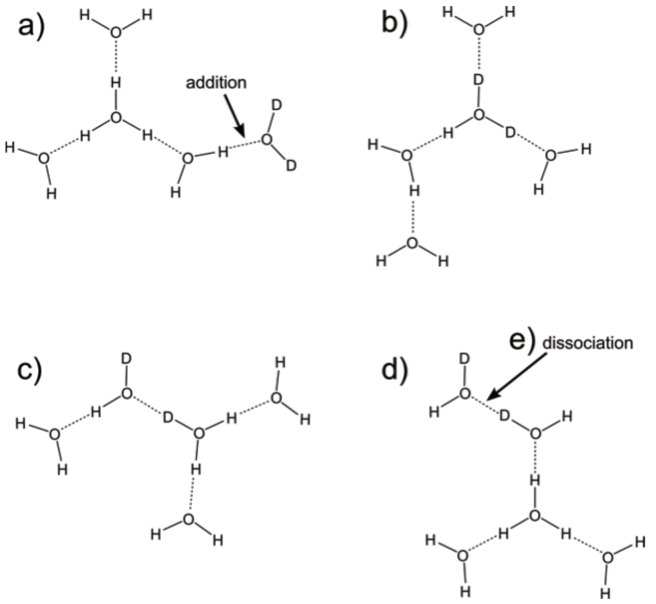

Figure 7. Intra-cluster rearrangements leading up to loss of a HDO molecule from the reaction intermediate. Details in text. Courtesy of Dr. M. J. Ryding, based on Mella and Ponti [111].

As already indicated, the H_3O^+ core is primarily stabilized by interaction with the three nearest neighbours of the first solvation shell, the Eigen cation. However, the positive charge is effectively dispersed also to the second solvation shell and probably beyond that, as demonstrated by Swanson and Simons [145] on the basis of a *ab initio* energy decomposition analysis under dynamical as well as static conditions.

In a conclusion, study of proton transfer is a relatively young and rapidly growing subdivision of physical chemistry, with many discoveries still to be made. Furthermore, understanding the occurrence of proton transfer in finite clusters is of principal importance for our qualitative picture of the chemistry of water clusters and their relation to bulk aqueous solution.

3 Methods

The work presented in this thesis is mainly concerned with different types of charged clusters where the main component is water; more specifically clusters of the type $X^{\pm}(H_2O)_n$, where $X^{\pm}$ can be various positively or negatively charged ions.

For the experimental part of the study we employed ESI-QTOF spectrometer (described in Chapter 3.1). The methods that were used for the quantum chemical modelling are briefly discussed in Chapter 3.2.

3.1 Experiments

The instrument is a modified mass spectrometer QTOF 2 from Micromass/Waters, Manchester UK. A schematic overview of the instrument can be seen in Figure 8. Cluster ions are produced by the electrospray source, and enter the main chamber through an orifice. A specific cluster size can be selected by the quadrupole mass filter and transferred to the collision chamber, where the clusters may react with a gaseous sample. The products are analysed by the time-of-flight mass analyser.

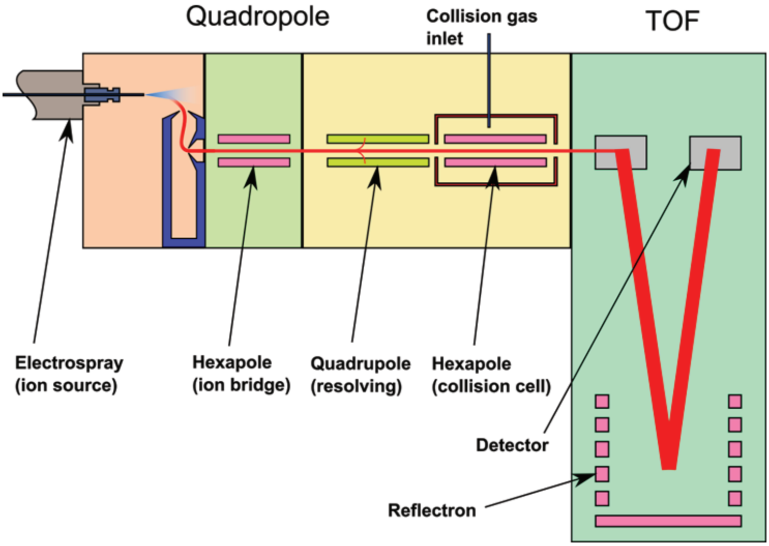

Figure 8. Schematic of the QTOF 2 mass spectrometer.

The general operation principles of the electrospray unit (Section 3.1.1), linear quadrupole analyser (Section 3.1.2), collision cell compartment (Section 3.1.3), and time-of-flight unit (Section 3.1.4) are summarized from Refs. [146, 147]. This account is followed by description of experimental procedure and experimental data treatment routine (Section 3.1.5).

3.1.1 Electrospray ion source

Electrospray ionization is a soft ionization technique, and is particularly useful for producing both ions of macromolecules and charged aqueous clusters. The introduction of this technique to mass spectrometry in the 1970s and 1980s made a wide range of studies of the properties and structures of large weakly bound water systems possible. Electrospray ionisation is an excellent tool for producing both pure and, by introducing different solutes (*e.g.* ammonia, pyridine, bisulfate, alkali metals, halogen ions), mixed water clusters. Although electrospray ionization has become a very important technique in many areas, the exact details of the ion production mechanisms in the electrospray sources are still unclear.

ESI is produced by applying a strong electric field, under atmospheric pressure, to a thin jet of liquid exiting under pressure from a small orifice (capillary). Commonly a syringe feeds the solution at a typical rate of 5–20 μl min^{-1} with help of a syringe pump. The field induces charge accumulation at the liquid surface located at the end of the capillary, which as a result will break to form highly charged aerosol particles. These droplets then pass either through a curtain of heated inert gas, often nitrogen, or through a heated capillary to remove the excess solvent molecules. Droplets experience consecutive desolvation, ion evaporation and coulombic explosion events until most of the solvent is removed and one gets the charged species of interest.

The electrospray design can also use other gas streams, for instance nebulizer gas (coming from behind the needle) which enables higher flow of solvent (Figure 9). It is usually possible to heat the desolvation gas and different parts of the electrospray, like the capillary. Conversely, if desired, the desolvation of the ions can be left incomplete, which useful for production of the clusters studied in this work. The operating parameters of the source can be optimized for production of a wide distribution of charged molecular clusters containing both the solvent and the solute. In contrast to the operating conditions typically employed for biomolecular applications, in our work we lowered the drift field of the ion source to reduce desolvation, which resulted in enhanced survival of larger clusters. Upon leaving the ion source region and entering the high vacuum region of the apparatus, the cluster ions are no longer heated by collisions, but continue to decompose spontaneously (evaporative ensemble).

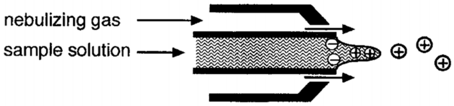

Figure 9. Illustration of an electrospray capillary [146].

The spray produced in this fashion is then transferred to the low-pressure compartments of the source through a series of skimmers or capillaries. Clogging of small opening of capillary or skimmer can be a problem, especially if the sprayed solution contains inorganic salts. To reduce this problem, the QTOF 2 used in this work is fitted with an electrospray with the so-called z-spray configuration. In such a configuration, a skimmer is placed orthogonal to the spray plume and extracts the charged droplets with the help of the electric field between the needle and the skimmer, while the rest of the plume containing mostly solvent is removed. Behind the first skimmer is a second skimmer positioned orthogonal to the first skimmer, again extracting part of the spray, which further transported to the ion optics in the high vacuum region and proceeds to mass analyser unit.

3.1.2 Linear quadrupole mass filter

The quadrupole analyser is a device, which uses the stability of the trajectories in oscillating electric fields to separate ions according to their m/z. A quadrupole has several attractive properties: high scan speed, high throughput of ions, compact design and low price. A linear quadrupole consists of 4 perfectly parallel metallic rods (each usually 1–2 cm in diameter and 15–25 cm in length) placed symmetrically around the axis traversed by the ion beam (z-axis). A voltage applied to the each opposite pairs of rods consists of a DC part (U) and an AC part, the latter typically varying with a radio frequency (RF) as $V\times\cos(wt)$, where $w/(2\pi)$ is the frequency of oscillation (Figure 10).

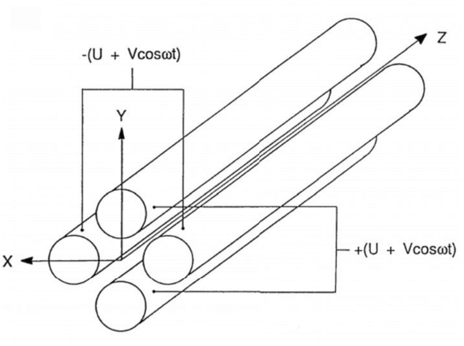

Figure 10. Schematic of a linear quadrupole mass filter [146].

The voltages result in time varying electric fields in the quadrupole, causing the path of an ion moving between rods to oscillate around the z-axis. In case the motion is stable, and depending on the amplitude of the oscillations, the ion will either discharge on the rods or exit the quadrupole on the other side. So the quadrupole acts as a mass filter with properties determined by the applied voltages. Increasing U and V at constant U/V ratio allows the ions with the higher *m/z* ratio to pass through. The width of a window around *m/z* in which ions have stable trajectories is determined by the ratio U/V. Increasing U relative to V results in a narrower window, *i.e.* higher resolution. But a relatively high resolution can only be achieved at the cost of significantly reduced transmission. Therefore, a typical quadrupole is operated at a resolution sufficient to separate ions with a unit difference in mass, *m/z* ± 0.5 u, *i.e.* unit resolution.

Another useful quality of the quadrupole is possibility to use it as a high pass filter by setting the DC voltage U to zero, which is referred to as RF-only mode, in which essentially all ions are transmitted.

3.1.3 Collision cell

In some cases characterization of the ions is facilitated by means of activating or reactive collisions within the mass spectrometer. For instance, by colliding the beam of ions with argon at high collision energies, fragmentation of the ions is observed, allowing to obtain additional information about the composition and structure of the ions.

The collision cell is a 16 cm long compartment situated inside the QTOF 2 along the path of the ion beam right after the quadrupole mass analyser. A hexapole ion guide inside the collision cell is used to transport the ions through the cell. A collision gas inlet tube connected to the cell allows for a reactant to be introduced into the compartment. In the instrument used, the gas inlet may be fitted with a small stainless steel container containing high purity D_2O. The water container is cooled by an ice/water mixture to obtain a constant vapour pressure above the D_2O sample. Stainless steel tubing connects the container to an ultra-high vacuum leak valve that regulates the flow of D_2O into the collision cell. Also connected is a baratron manometer, used to monitor the vapour pressure, and a rotary pump that can be used to evacuate the gas. In the experiments where ammonia is used as reactant gas, the D_2O container is replaced by a gas cylinder containing high purity NH_3.

One of the biggest practical problems is water (and other molecules) adsorbing on metal surfaces, resulting in contaminants covering the walls of the collision chamber. These contaminants can react with the clusters or with the collision gas forming new impurities. An example of this is formation of HDO from H_2O and D_2O complicating interpretation of experimental results (Section 2.4.2). The presence of contaminants can be reduced by conditioning of the collision cell with a comparably high flow of pure D_2O vapour for a period of few days.

3.1.4 TOF mass analyser

The TOF analyser is used to separate the ions after their initial acceleration by a strong electric field according to their velocities during their drift in a free-field region. The ion accelerates as the potential energy of the ion in the field is converted to kinetic energy. After exiting the electric field, the velocity of the ion on the drift in a free-field region is related to its mass. Thus, ions can be separated in time according to their mass-to-charge ratio *m/z* if they move along a certain distance at constant velocity. For a flight length l the time-of-flight of the ion becomes: $t = (m/z)^{1/2} \times l/(2eU)^{1/2}$, *i.e.* the time-of-flight depends on the square root of the mass-to-charge ratio of the ion. At the end of the flight path the ions are detected, and the recorded time-of-flight values are then converted to an *m/z* spectrum.

The ions in the beam will have a kinetic and spatial distribution that will lead to a lower mass resolution, due to a spread in flight times of ions with the same *m/z*. As was mentioned in Section 2.2.2, many TOF instruments include a reflectron, which in essence is a series of concentric rings perpendicular to the flight path (Figure 8). In the reflectron, the ion flight is reversed by a retarding field. Ions with higher kinetic energies will spend longer times in the reflectron as they can penetrate deeper into the field, thus reducing the velocity spread and improving the overall resolution.

In the case of an orthogonal acceleration TOF instrument (Figure 8), part of a focused continuous ion beam is orthogonally pushed into the top part of the time of flight unit. The separated part of the beam is then accelerated through the drift tube by a continuous field (typically 5–10 kV), which is orthogonal to the original beam path and parallel to the pulsed field. However, the ions still keep their velocity component in the original direction, leading to the flight path of a shape that reminds of the letter "V".

A high vacuum is essential for operating a TOF unit in order to avoid adsorption of water and other vapours on the detector, since this could cause degrading and possibly electric discharge. The pressure also influences the probability of ions colliding with the background gas molecules. The mean free path of the gas molecules at the typical TOF operating pressure is about 1 km, which by far exceed a couple of meters of the flight tube.

The TOF possesses several attractive properties: the mass range is in principle unlimited, and the mass resolution is relatively high. Resolution is often given as $m/\Delta m$, FWHM (Full Width at Half Maximum), where $m/\Delta m$ is the ratio between the ion mass and the width of the peak measured at half the height of the peak. A typical resolution obtained in our studies is $m/\Delta m = 5000$ (FWHM), which is sufficient for most purposes. For the unit resolution often used by quadrupoles (Section 3.1.2) the width of the ion separation is always unity, meaning that the resolution is $m/\Delta m = 200$ for ions of mass 200 u, $m/\Delta m = 500$ for ions of mass 500 u, and so on.

3.1.5 Experimental procedure

The following Section relates the procedure by which the experiments presented in Paper I, II, VI and VII were performed utilizing the QTOF 2 mass spectrometer described in the preceding sections.

The cluster ions were produced by the electrospray ion source, using various aqueous solutions that were fed to the electrospray through a capillary connected through a syringe in a syringe pump (flow rate 5–20 µl min^{-1}). Careful conditioning of the syringe and connecting capillary by washing it with solvent or solution was required before and after experiments or when switching solutions. Some corrections to the typical settings of an electrospray were necessary to produce a wide distribution of water-containing clusters. Typically, the electrospray was operated without heating of the capillary or the desolvation gas. The cone gas was turned off and the desolvation gas flow was low, especially when dealing with the largest water clusters. Special attention to the adjustment of the nebulizer gas was necessary, as production of cluster ions was very sensitive to this gas flow.

After production, the ions entered the QTOF 2 high vacuum region. In the quadrupole mass filter either a broad mass range (0–1500 u) was allowed to pass through in order to record an abundance spectrum, or a single cluster size was selected to be reacted with the reactant gas. In the latter case, the number of water molecules in the clusters studied ranged from 0–38, depending on the specific cluster. The voltages on the quadrupole mass filter were set to allow for selection of a given *m/z* value corresponding to a particular cluster at a mass resolution high enough to avoid passage of ions with *m/z* ± 1.

In a part of experiments, after passing the quadrupole, size selected clusters entered the collision cell and were reacted with high grade D_2O or NH_3. The clusters selected in this way were decelerated to a common center-of-mass collision energy (E_{com}) 0.1 eV. Alternatively, in cases where the cluster mass was less than 100 u, collision energy in the lab-frame (E_{lab}) was kept at 0.6 eV, due to the notable loss in beam intensity for lab-frame energies lower than 0.6 eV. Residence times in the collision cell were between 110 and 160 µs for these energies. The pressure of the reactant gas was kept so that the number of clusters reacting was less than 10%. On the one hand, a low concentration of collision gas reduces the number of multiple collisions between gas and clusters. On the other hand, a too low gas pressure will lead to lower product intensity, so problems may arise due to poor signal-to-noise ratio of the mass spectrum product peaks thereby increasing the uncertainties of the measured abundances.

Conditioning of collision cell included several steps. The day before heavy water was introduced, all vacuum lines were heated up to ~100^0C for several hours and evacuated using the supplementary rotary pump. After liquid D_2O was added to the container in the external gas inlet, cycles of freezing, pumping and heating were performed repeatedly on the container to evacuate any dissolved gases from the heavy water. To condition the collision cell and remove impurities, the cell was flushed with D_2O vapour for about 2–3 days. As mentioned above (Section 3.1.3) contamination of the collision gas in the form of HDO still was expected. When using ammonia as reactant gas, a gas cylinder containing high purity NH_3 was fitted to the gas-inlet system. For the measurements performed with an empty collision cell, all connections from the gas-inlet system were closed, ensuring sufficient time to allow the collision cell to be evacuated.

Upon exiting the collision cell, the reaction products and remaining reactants were accelerated before entering the orthogonal acceleration TOF unit operating in single-V mode, using a 9.1 kV acceleration voltage pulse for positive ions and –7 kV for negative ions. Flight times for ions of mass 55–700 u in the TOF were 10–37 μs. The resolution of the TOF was set to $m/\Delta m$ = 5000 (FWHM). A pair of chevron microchannel plates was used for the detection of ions in the TOF. The settings of the detector were adjusted beforehand so that it was sensitive enough to correctly reproduce a wide range of peak intensities without giving too much noise to the signal and discriminating relative intensities. To check if the dynamic range of the detector was acceptable, pure sodium chloride clusters were produced from a 17 mM solution and used for calibration. For each $Na^+(NaCl)_n$ or $Cl^-(NaCl)_m$ cluster a distribution of peaks arising from the chlorine isotopes were observed. By comparing the ratio of detected intensities in the distribution to values calculated using literature natural isotopic abundances [148], it is possible to estimate detection bias towards smaller or larger peaks.

Upon impact of an ion on the detector, there is a relaxation time in the detector system during which no other ion can be detected—so called "dead-time". While this time is small (5 ns) it can distort the measured intensity of peaks, since only one of several ions arriving at the same time is detected. The software platform that comes with the QTOF 2 (MassLynx MS v 4.0) can compensate for this effect. The correction was minor and essentially only affected the parent ion peak. To avoid pulse pile-up the electrospray source voltages were adjusted to keep the ion count of the parent ion peak at below 300 counts per second during the sampling time of typically 2 min. If major peak intensity was lower than 300 counts, acquisition times much longer than 2 minutes had to be used.

Throughout the experiments, reference measurements were performed regularly (typically each 7th or 10th measurement). In our experiments, $H^+(H_2O)_{11}$, $OH^-(H_2O)_{10}$ or H^+(pyridine)$(H_2O)_{11}$ ion was used as reference substance. Analysis of the reference ion spectra can be used to compensate for varying reactant gas pressure in the collision cell, which normally had a slow exponential decay with time towards a constant value. On a separate occasion a background measurement was performed for each cluster, with an empty collision cell. The reported abundance spectra were also measured with empty collision cell.

The spectra from the experiments with size selected cluster ions were first treated using the program MassLynx MS, and dead-time correction was made. The spectra from MassLynx MS were processed by a Matlab program that allowed us to calculate the total number of ions detected during the sampling time for a number of specified peaks in the spectrum. Alternatively, in cases when mass identification was complicated, spectra were processed in similar fashion by hand.

Spectra obtained in different measurements were normalized to the total ion intensity in each spectrum, calculated as sum of all peaks in spectrum. The reference experiments were analyzed and corrections were made to compensate for the slow variation in collision gas pressure if the slow exponential decay was considered to be non-negligible. For each peak the corresponding normalised intensity in the background measurement was deducted. The abundance spectra that were measured were analyzed using MassLynx MS by combining the peak intensities of all scans, and correcting for dead-time intensity loss. Finally, the evaporation of water molecules from the clusters was calculated from the background measurements.

3.2 Calculations

The chapter provides brief account on computational methods and procedure (Section 3.2.1) used in quantum chemical calculations. This is followed by a discussion on accuracy and performance of computational methods of choice (Section 3.2.2).

3.2.1 Computational procedure

Quantum chemical calculations were carried out using the program suites GAUSSIAN 03 and GAUSSIAN 09 [149]. All relevant structures (reactants, transition structures, and products) of ionic or neutral water clusters were characterised by complete geometry optimisation using MP2 (Paper I), B3LYP (Paper I, II), CAM-B3LYP (Paper VI). These levels of theory were used in conjunction with the 6-31G(d) and 6-311+G(d,p) (Paper I), B3LYP/6-311++G(2d,2p) (Paper II), aug-cc-pVDZ (Paper VI) basis sets. MP2 is short for Møller-Plesset perturbation theory to second order (Section 2.3.3), a quantum chemical post-Hartree–Fock ab initio method. B3LYP denotes hybrid density functional (Becke, three-parameter, Lee-Yang-Parr), an exchange-correlation functional, consisting of weighted combination of various density functionals together with a fraction of exact (Hartree-Fock) exchange. The three fitted parameters define the hybrid functional, specifying how much of the exact exchange is mixed in. This is one of the most popular density functionals, known to give rather reliable results for systems of different nature. Lastly, CAM-B3LYP functional developed by Handy and co-workers [90] presents a long range corrected version of B3LYP functional; correction is performed using the Coulomb-attenuating method.

Various basis sets have been employed in our studies, both of the Dunning and Pople type. Well-known that polarization is important aspect of bonding, especially for description of hydrogen bond, so typically polarized functions have to be used as a part of common basis sets. The name 6-31G(d) indicates that polarized d functions were added to heavy atoms to improve the 6-31G basis set. Another polarized basis set 6-311+G(d,p) adds p functions to hydrogen atoms in addition to the d functions on heavy atoms. Further, diffuse functions are important for negative ions, molecules with lone pairs and other systems where electrons are relatively far from the nucleus. It also known to improve description of large, "soft" molecular systems and systems with weak bonds, like molecular clusters. The 6-311+G(d,p) and aug-cc-pVDZ basis sets are respectively the 6-311G(d,p) and cc-pVDZ sets with added diffuse functions. Additional set of diffuse functions on hydrogen atoms like in 6-311++G(2d,2p) basis set usually do not make significant difference in accuracy of results, but are relatively cheap to include into the calculation anyway. Finally, basis sets like 6-311++G(2d,2p) add multiple polarization functions per atom and are practical for many uses, for example they improve description of electron correlation. Also, basis sets like cc-pVnZ include polarized functions by design.

For previously well-known clusters (see Chapter 4), starting geometries could be taken from the plentiful of computational studies. The generation of initial geometries for other kinds of clusters was done by hand based on the number and types of hydrogen bonds in the cluster as well as the arrangement of the molecules within the cluster. Up to 50 different geometries were generated this way and submitted for geometry optimization. In several cases it turned out that the same minimum structure is obtained from different initial geometries. The proton transfer energy barriers were probed by performing transition state calculation with the same computational method as employed for geometry optimization. The character of each stationary point (transition structure or minimum energy structure) was identified from vibrational analysis, and relative energies for each point were corrected by including unscaled zero-point vibrational energies (ZPVE). Furthermore, intrinsic reaction coordinate calculations for each transition structure was performed to ensure that they connect the actual minimum-energy structures. When the IRC routine occasionally failed numerically, we were careful to verify the connections not only on the basis of the vibrational motion of the reaction coordinate at the TS but also by showing that extrapolation in the forward and backward directions, respectively, led to geometries that upon minimization gave the indicated minima.

3.2.2 Method validation procedure

The main purpose of our computational efforts was to see if it was possible to establish models of the observed experimental trends, which first would require the search for the global potential minimum for each aqueous cluster size. Undoubtedly this is a tedious task involving geometry optimizations from a rather large set of realistic isomeric trial structures.

As discussed in Chapter 2.3, for large systems DFT is the method of choice for including electron correlation where post-Hartree–Fock methods are too expensive or simply impossible. In light of the huge computational efforts, involving the treatment of molecular systems as large as for example $HSO_4^-(H_2O)_{11}$, use of density functional theory based methods is attractive due to practicability and computational economy.

Use of DFT-based method is computationally efficient and is capable of providing qualitative results, although the accuracy of any functional in predicting a given molecular property requires careful validation. For this reason, in our work we tried to avoid heavily parameterized functionals constructed by extensive parameter fitting to molecular datasets (*e.g.* M06-family or mPW-functionals), since their accuracy is suspicious, if one is to calculate some substance or property beyond the fitting database of those parameters. An alternative approach would have been to employ a semi-empirical or molecular mechanical potential and perform simulated annealing molecular dynamics runs to locate candidate structures for subsequent DFT geometry optimization. However, this idea was abandoned in the absence of sufficiently accurate potentials (Section 2.3.1). Further, assessment of density functionals and basis sets used in Papers I, II and VI is described.

First we will discuss the performance of B3LYP/6-311+G(d,p) used in many calculations in Paper I and B3LYP/6-311++G(2d,2p) employed in Paper II. Widely used hybrid functional B3LYP in conjunction with a sufficiently large basis set was suggested to provide rather accurate structures and dissociation energies for water clusters compared to a benchmark calculations and experimental results [16, 150, 151]. To probe these assumptions, test calculations of $OH^{-}(H_2O)_n$, H_2SO_4 and $H_2SO_4(H_2O)$ systems were performed in order to obtain information with regard to the accuracies that can be expected for the clusters of interest (Paper II). The results show that B3LYP/6-311++G(2d,2p) method underestimates dissociation energies by *ca.* 20 % but that bond lengths and angles of test systems as well as cluster size variability are well reproduced. "Calibration" of B3LYP/6-311+G(d,p) (Paper I) has also been done (although on a smaller set of test subjects, namely $(H_2O)_n$, $n = 1$–5), and the accuracy of this model chemistry is very similar, since, as was discussed in Section 2.3.6, DFT methods are to some degree insensitive to quality of basis set. Nonetheless, diffuse and polarized functions were considered to be important for correct description of structure of most of clusters studied and were added to basis sets when necessary, as described in Section 3.2.1.

A possible reason for the discrepancy between B3LYP and accurate CCSD(T)/CBS [150] dissociation energies could lie in improper description of dispersion interactions in the B3LYP functional, resulting for example in poor description of weak hydrogen bonds [152-154]. Therefore, the long-range corrected version of B3LYP, CAM-B3LYP [90] along with augmented double-zeta basis set, recently shown to give good results for aqueous clusters [155], was also tested. The increase in computational cost going from B3LYP to CAM-B3LYP is relatively small. However, the computationally predicted trends with regard to size-variability are rather consistent for both functionals. In addition, we tested CAM-B3LYP/aug-cc-pVDZ on a dataset from Paper II; it was found that error in dissociation energies was reduced at least by a factor of two. All these attractive features made CAM-B3LYP/aug-cc-pVDZ the method of choice in Paper VI.

In light of this discussion, we consider B3LYP/6-311+G(d,p), B3LYP/6-311++G(2d,2p) and CAM-B3LYP/aug-cc-pVDZ to provide reasonable structural and energetic insights of sufficient accuracy for the present purposes, in particular for reproducing qualitative trends. It should be mentioned that in order to reach the necessary accuracy required for reproducing the weak size variation observed in the experimental evaporation data, values better than ± 2 kJ mol^{-1} are required, which appears to be impractical and unrealistic. In addition to the method accuracy considerations, it is important to note that entropic factors are not accounted for in the computed set. It is not possible to provide accurate estimates of entropy from standard ab initio calculations based on the rigid rotor/harmonic oscillator approximation since anharmonicity must be accounted for if quantitatively reliable formation free energies are desired. In conclusion, on the basis of the immense computational cost of calculation of anharmonic vibrational frequencies, especially for water clusters with up to $n = 11$, entropy effects are ignored in all of the calculations presented in this thesis.

As a note, the performance of MP2/6-31G* method used in some calculations in Paper I, was never tested in our work. We may speculatively estimate its accuracy as rather unreliable due to large basis set superposition error, a consequence of insufficiently large basis set. MP2 method in conjunction with reasonably big basis set proven to be much more accurate method (*e.g.* [16]), but we considered it to be too computationally demanding for studies of large water clusters.

4 Results and discussion

Present chapter summarizes the experimental results that are given in the papers attached to this thesis. Chapter 4.1 deals with the unimolecular decomposition of the selected clusters as presented in Papers I–IV, VI and VII, including the findings of the quantum chemical calculations regarding the cluster structures and stability. The results of cluster reactions with heavy water are covered in Chapter 4.2. The same chapter contains the results of the computational studies aimed at unravelling the proton transfer mechanism in the clusters studied in Papers I, II, VI and VII. Chapter 4.3 describes cluster reactions with ammonia (Papers III–IV), as well as application of the results to kinetic modelling for atmospheric ion composition. Finally, Chapter 4.3 also deals with magic numbers of pyridine-containing water clusters.

4.1 Cluster distributions and structures

The chapter provides mass-spectrometric observations on cluster distributions and evaporation patterns (Section 4.1.1 and 4.1.2, respectively) with special interest in magic numbers. This is followed by description of theoretical investigation of cluster hydration (Section 4.1.3).

4.1.1 Abundance spectra

Abundance spectra for all cluster ions studied were collected using the ESI-QTOF instrument (Chapter 3.1) with an empty collision cell. The quadrupole mass filter was operated in the RF-only mode.

A typical abundance spectrum from Paper I is shown in Figure 11. $H^+(\text{pyridine})_m(H_2O)_n$ clusters with $m = 1–3$ and $n = 0–80$ were produced using a 100 mM pyridine solution. The signals for $H^+(\text{pyridine})_1$, $H^+(\text{pyridine})_2$, $H^+(\text{pyridine})_3$ and $H^+(\text{pyridine})_3(H_2O)$ ions have high intensity. Li *et al.* [156] observed similarly high intensities of the clusters with $m = 3$ and $n = 1$ to that seen in Figure 11. The other pyridine clusters exhibit weak intensity variations with size, although it would be difficult to assign particular magic numbers within the series, resulting in a rather smooth size distribution.

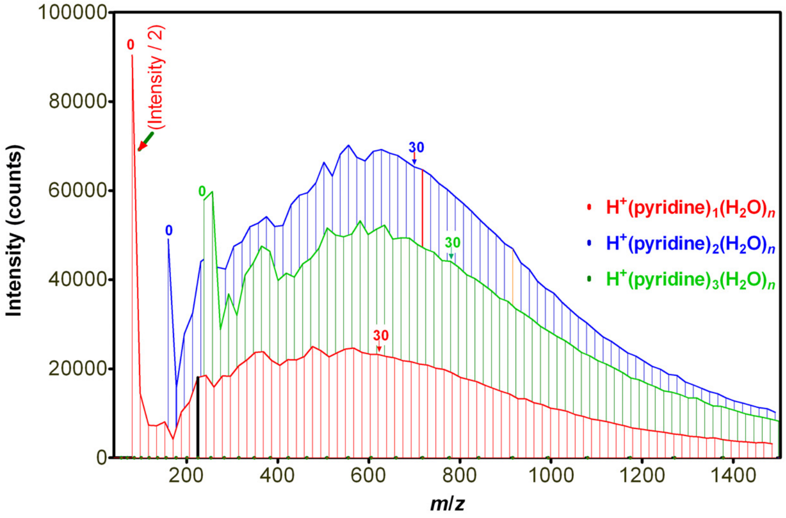

Figure 11. Abundance spectrum from Paper I, $H^+(pyridine)_1(H_2O)_n$, $H^+(pyridine)_2(H_2O)_n$ and $H^+(pyridine)_3(H_2O)_n$ clusters are shown. $n = 0$ and 30 are marked for all cluster types. The lines between the peaks are drawn to guide the eye.

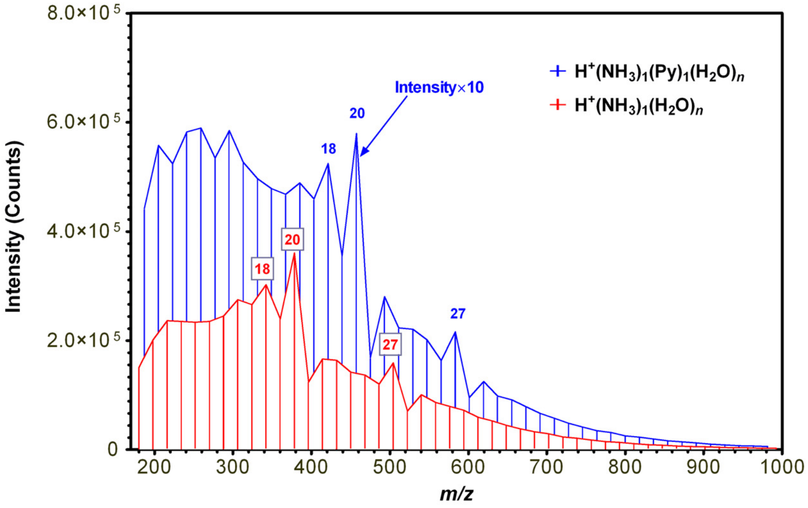

Figure 12. Abundance spectrum of $H^+(NH_3)_1(H_2O)_n$ and $H^+(NH_3)_1(pyridine)_1(H_2O)_n$ clusters (Paper IV). The $H^+(NH_3)_1(pyridine)_1(H_2O)_n$ clusters are shown with the intensity increased by a factor of 10 to improve readability. Some peaks in the series are labelled indicating the number of water molecules in the cluster.

Next, the abundance spectrum (Figure 12) was obtained by electrospraying solution containing 30 mM ammonia and 2.5 mM pyridine (Paper IV). Only the $H^+(NH_3)_1(H_2O)_n$ and $H^+(NH_3)_1(pyridine)_1(H_2O)_n$ are shown, and the other ions are ignored. In agreement with previous studies [126, 157] magic number clusters are observed for $H^+(NH_3)_1(H_2O)_n$ with $n = 18$, 20, and 27, displaying the characteristic z-shaped kink in the curve with their larger neighbour having lower than expected abundance. Interestingly, clusters containing both ammonia and pyridine, $H^+(NH_3)_1(pyridine)_1(H_2O)_n$, show magic numbers for the same number of water molecules as the $H^+(NH_3)_1(H_2O)_n$ clusters. We observe that the addition of a pyridine molecule to $H^+(H_2O)_n$ and $H^+(NH_3)_1(H_2O)_n$ [126] cluster types results in $H^+(pyridine)_1(H_2O)_n$ and $H^+(NH_3)_1(pyridine)_1(H_2O)_n$, respectively, where the former loses its magic numbers and the latter retains them. This feature will be discussed further in Section 4.3.2.

Figure 13 (Paper II) shows the abundance spectrum of $HSO_4^-(H_2O)_n$, $OH^-(H_2O)_n$ and $SO_4^{2-}(H_2O)_n$ clusters obtained from a solution of 15 mM $NaHSO_4$ and 15 mM crown ether. Addition of the crown ether was supposed to suppress sodium-containing ions, thus enhancing intensity of bisulfate series. Use of sulphuric acid solution for production of bisulphate series was avoided for fear of damaging the instrument. In addition to the exceptionally high abundance displayed by the bisulfate molecular ion and its hydrate, weak magic numbers could be implied by the increased intensity for $n =$ 5, 12, 14, 20, 26 and 28. The $OH^-(H_2O)_n$ abundance in Figure 13 shows peaks that might be considered as weak magic numbers: $n = 11$, 13, 17, 21 and 30, which is in reasonable agreement with previously published data [113, 158]. The clusters containing SO_4^{2-} show an odd/even effect with alternating higher and lower intensities due to overlap with a water cluster series containing an unidentified singly-charged ion. This unfortunate pattern made further studies of this ion series possessing a wide spectrum of appealing properties ([159-162]) impossible. It should be noted that due to the fact that $SO_4^{2-}(H_2O)_n$ clusters carry double charge, their actual mass is twice that of the other cluster series in the spectrum. Also, the mass spectrum recorded in the negative mode usually exhibits large variety of $X^{Z-}(H_2O)_n$ ions [40], as can be seen in inset to Figure 13. These "chemical noise" peaks originate from $O^-(H_2O)_n$, $O_2^-(H_2O)_n$, $HO_2^-(H_2O)_n$ and various water clusters containing nitrogen and carbon compounds. For this reason special care had to be taken when analysing and attributing peaks in the negative mode.

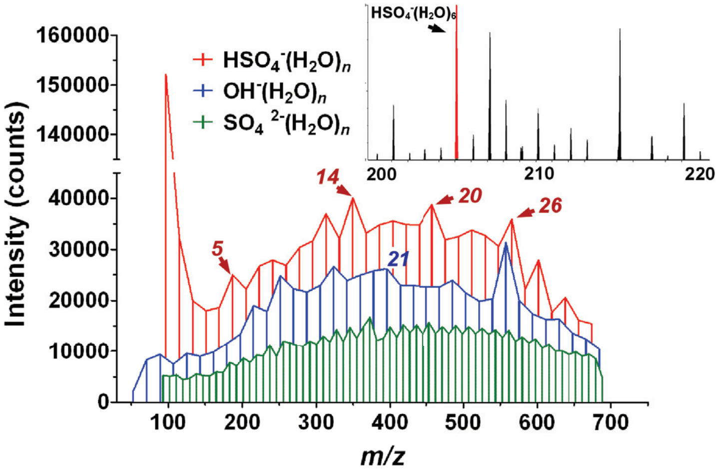

Figure 13. Abundance spectrum from Paper II, showing $HSO_4^-(H_2O)_n$, $OH^-(H_2O)_n$ and $SO_4^{2-}(H_2O)_n$ clusters. The numbers above the peaks indicate the amount of water molecules in the clusters. The inset shows a magnified region of the spectrum.

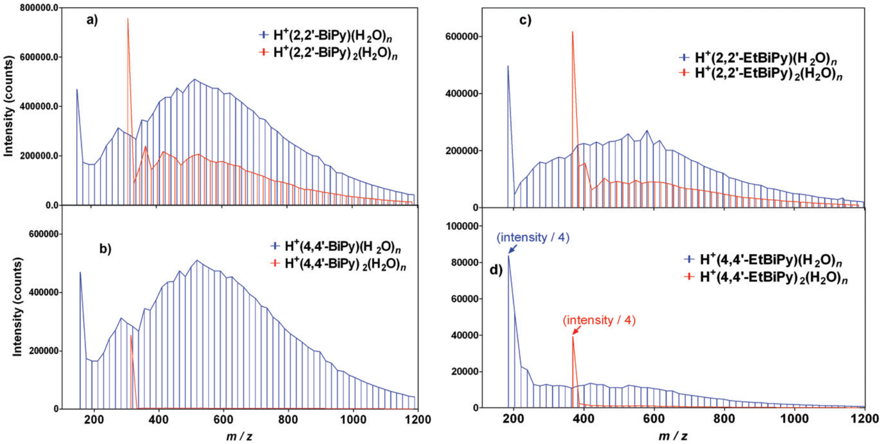

Figure 14. Abundance mass spectra obtained by electrospray ionization of solutions containing a) 2,2’-bipyridine, b) 4,4’-bipyridine, c) 2,2’-ethylenebipyridine or d) 4,4’-ethylenebipyridine; the collision cell was empty. The intensities of some peaks have been reduced for clarity.

Figure 14 provides cluster distributions obtained by electrospray ionization of 5 mM aqueous solutions of 2,2’-bipyridine, 4,4’-bipyridine, 2,2’-ethylenebipyridine or 4,4’-ethylenebipyridine. While there are some intensity variations with size, no clear "magic numbers" can be seen. Molecular ions of each substance give strong signals in the spectra, while ions M_2H^+ sometimes being the dominant signal. In the spectrum of 4,4’-ethylenebipyridine, the intensity of the protonated monomer and dimer had to be decreased by a factor 4 for the sake of readability. Dimer water clusters $M_2H^+(H_2O)_n$ are generally lower in intensity compared to $MH^+(H_2O)_n$ and are exceptionally low in case of the 4,4’-species.

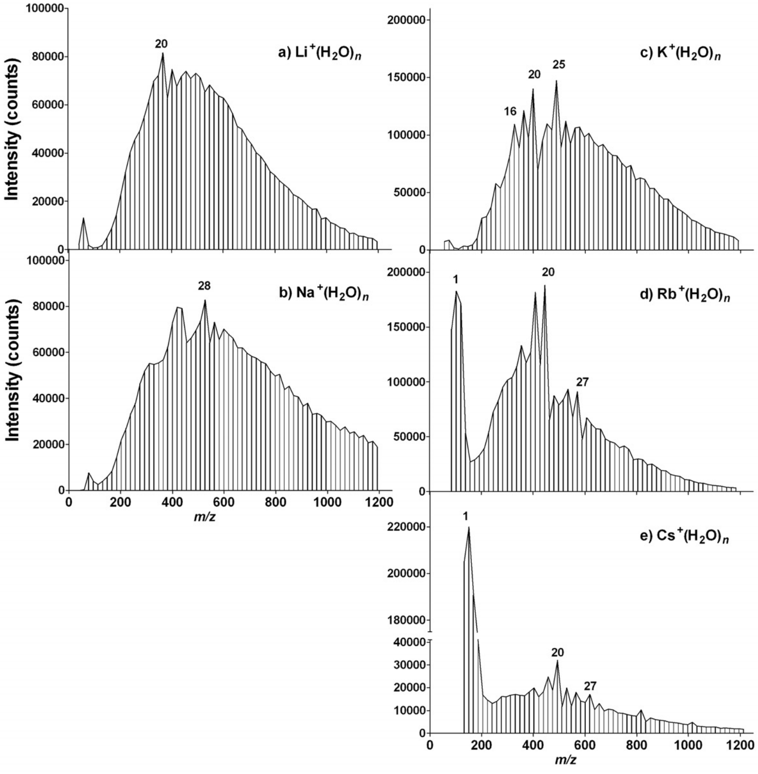

Figure 15. Abundance spectra of water clusters with alkali metal core-ions, $M^+(H_2O)_n$. Lines between peaks are drawn only to guide the eye. The numbers above the spectra correspond to the number of water molecules in the cluster.

Lastly, the abundance spectra reproduced in Figure 15 (Paper VI) for $M^+(H_2O)_n$ (with M = Li, Na, K, Rb or Cs) reveal distinct and reproducible sets of magic numbers for ions K–Cs. For $n < 30$ the observed patterns are in general in good agreement with previous studies [102, 103] despite the different methods used for cluster production and mass analysis. For $30 < n < 60$, the size range unique to our study, where intensity variations with size are also present but are less pronounced than for the smaller clusters.

4.1.2 Water evaporation patterns

The unimolecular decomposition of size-selected clusters during flight through an empty collision cell was studied. Except for the smallest clusters ($m/z < 100$) examined at a fixed lab collision energy ($E_{\mathrm{lab}} = 0.6$ eV), mass-selected clusters were decelerated to a center-of-mass collision energy (E_{com}) of 0.1 eV. This setting also ensured that the flight time is virtually the same for all cluster sizes (see Section 2.4.2). What presented is essentially the ratio between the signal intensity of the product of evaporation ion and that of the reactant ion of size-selected clusters as a function of n (Figures 16–18). The general trend for the relative intensity of the loss of one H_2O molecule from the cluster, regardless a nature of an ion, is that the tendency for evaporation of a water molecule increases with cluster size in a nearly linear fashion. This would be expected if the rate for H_2O loss were independent of cluster kind and all water molecules in a cluster were equally likely to evaporate. In general, the evaporation patterns displayed in Figures 16–18 clearly mirror the abundance spectra in that evaporation is suppressed for a magic number and is enhanced for the clusters being one size larger than a magic one.

Figure 16a shows the fraction of $H^+(\text{pyridine})_{1\text{–}3}(H_2O)_n$ cluster ions (Paper I) giving evaporation of one water molecule during their flight through the QTOF 2 instrument collision chamber. No clear magic numbers are indicated for these pyridine-containing clusters, in agreement with the abundance spectrum. In addition to a mentioned general size trend of linear enhancement of evaporation with the number of water molecules n in the clusters, evaporation also increases with the number of pyridine molecules present in the cluster. Virtually no evaporation of pyridine molecules was observed for any of the $H^+(\text{pyridine})_m(H_2O)_n$ clusters with $n > 0$, even from clusters with as many as three pyridine molecules.

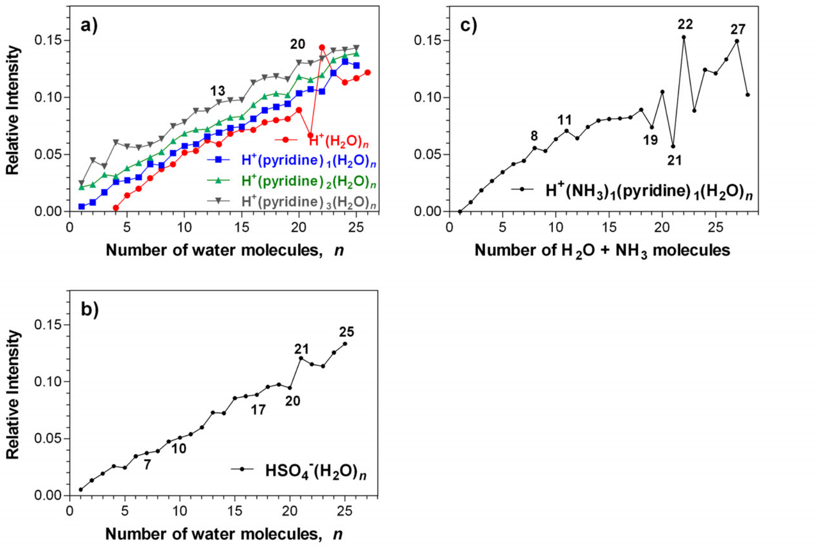

Figure 16. The relative abundance of clusters that have lost one water molecule when passing through the empty collision cell. a) $H^+(pyridine)_{0–3}(H_2O)_n$ as function of the number of H_2O in the cluster. b) $H^+(NH_3)_1(pyridine)_1(H_2O)_n$ as function of the number of H_2O and NH_3 molecules in the cluster. c) $HSO_4^-(H_2O)_n$ as a function of the number of H_2O in the cluster.

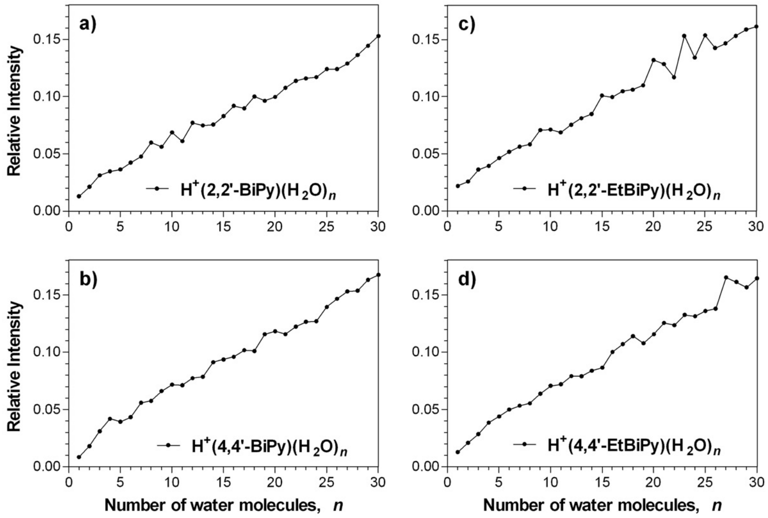

Figure 17. The relative abundance of $MH^+(H_2O)_n$ clusters that have lost one water molecule when passing through the empty collision cell. Shown are clusters containing a) 2,2'-bipyridine, b) 4,4'-bipyridine, c) 2,2'-ethylenebipyridine or d) 4,4'-ethylenebipyridine.

The loss of H_2O from the $H^+(NH_3)_1(\text{pyridine})_1(H_2O)_n$ cluster (Paper IV) is presented in Figure 16b as a function of the total number of molecules in the cluster, H_2O or NH_3. A marked decrease in evaporation is evident for clusters having 19, 21 and 28 water or ammonia molecules, in agreement with the findings from the abundance spectrum.

The unimolecular decomposition pattern of $HSO_4^-(H_2O)_n$ clusters shown in Figure 16c again complement the abundance spectrum (Figure 13), although the deviations from the straight line due to magic numbers are relatively small. For example, there are shallow dips for n = 5, 14 and 20 observed in Figure 16c that correspond to the increased intensity for these clusters in the abundance spectrum.

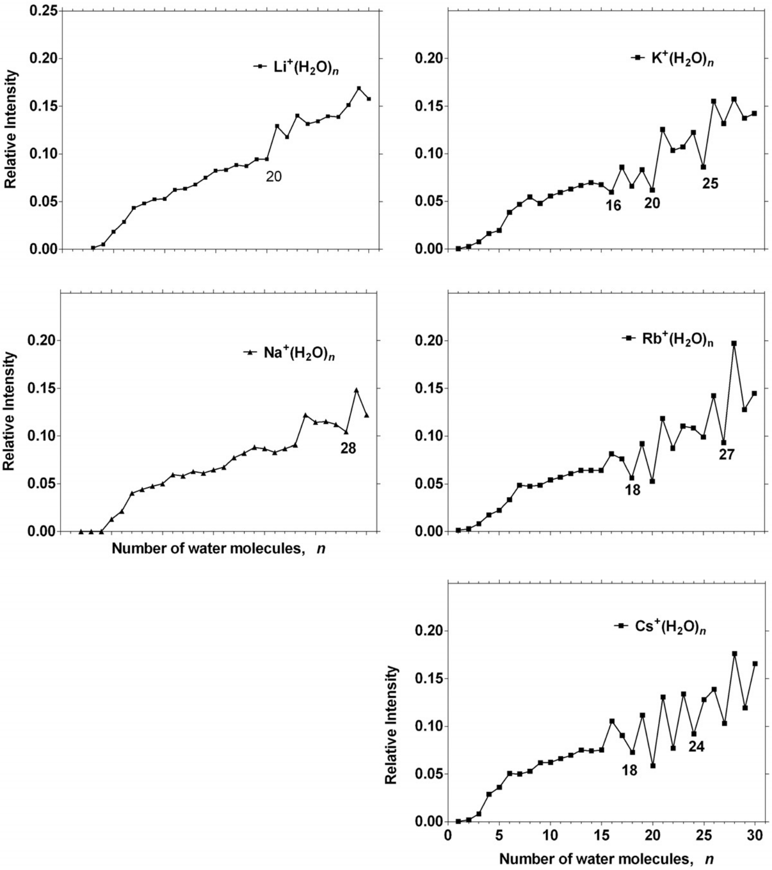

Figure 18. The relative abundance of size-selected $M^+(H_2O)_n$ clusters that evaporate one water molecule during passage through the empty collision cell.

Figure 17 provides the evaporation measurements of size-selected water clusters $MH^+(H_2O)_n$ (with M = 2,2’–BiPy, 4,4’–BiPy, 2,2’–EtBiPy or 4,4’–EtBiPy) as a function of *n* during flight through mass spectrometer. Inspection of Figure 17 reveals no major fine-structure features; abundance spectra (Figure 14a–d) are featureless either.

Figure 18 shows the loss of H_2O from size-selected clusters $M^+(H_2O)_n$ (with M = Li, Na, K, Rb or Cs) as a function of *n.* As for any other studied system, the over-all curve shapes appear to be proportional to cluster size, with an approximately linear dependence. Being no exception, alkali-metal–water clusters show consistent agreement between the abundance spectra and the corresponding evaporation patterns.

4.1.3 Cluster structures

The most favourable geometrical configuration found for each cluster size for $H^+(\text{pyridine})_m(H_2O)_n$ (m = 1, 2 and n = 0–6), $HSO_4^-(H_2O)_n$ (n = 1–10) and $A(H_2O)_n$ (A = H_2O, Li^+, Na^+, n = 3–8) clusters are reported in Papers I, II and VI.

A careful search for the global potential minimum for the smallest $H^+(\text{pyridine})_m(H_2O)_n$ clusters revealed that only a limited number of stable isomers exist. All structures in general had easily recognizable binding motifs, all having in common the tendency for maximizing the number of hydrogen bond interactions, although usually preferring formation of 4-membered rings over more tight or more loose formations. On this basis it became easier to locate the presumed global minima as well as gave valuable hints for the larger structures. A few examples of geometrical structures of most stable isomers are displayed in Figure 19. In all instances, pyridine essentially acted as a Brønsted base, strongly binding the extra proton. This was the case even when the initial geometry for complete optimization contained the proton on a water molecule. For m = 1, the water molecules form an interconnected network of hydrogen bonds associated with a pyridinium central ion through a hydrogen bond (Figure 19). For clusters containing two pyridines (m = 2) the two pyridine molecules are separated by bridge of one or two water molecules, which are surrounded by extra water molecules in larger clusters (Figure 19). Cluster structures with the two pyridines directly connected by a proton bridge (proton bonded dimer) with the water molecules surrounding the ionic core are disfavoured by having high total energies.

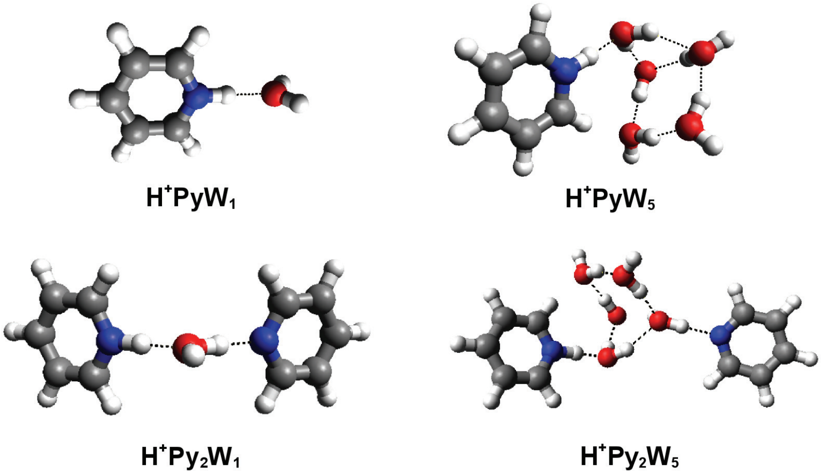

H^+PyW_1 H^+PyW_5

$H^+Py_2W_1$ $H^+Py_2W_5$

Figure 19. The selected most stable water/pyridine clusters, obtained with B3LYP/6-311+G**. In the labelling scheme of the clusters Py is pyridine and W is water.

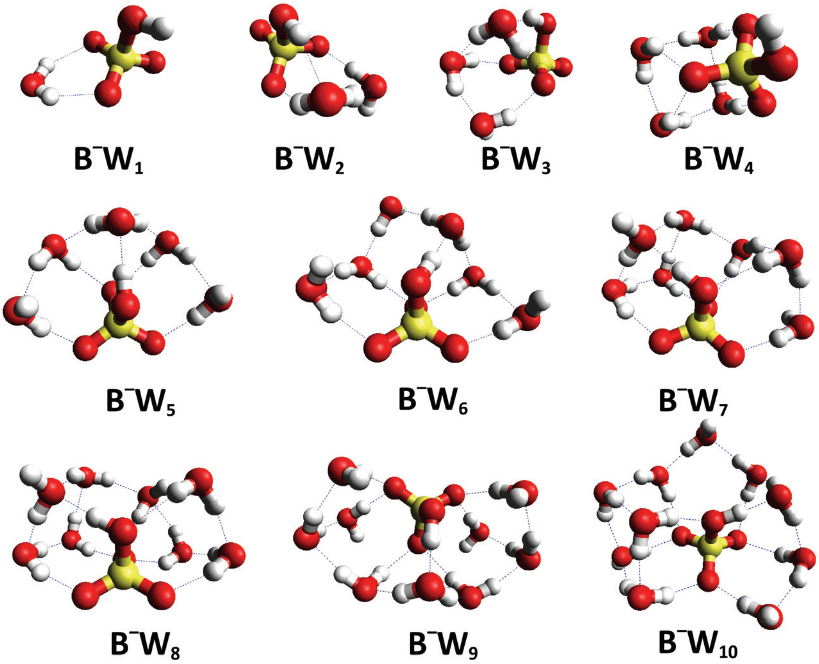

B^-W_1 B^-W_2 B^-W_3 B^-W_4

B^-W_5 B^-W_6 B^-W_7

B^-W_8 B^-W_9 B^-W_{10}

Figure 20. The most stable isomers found for $HSO_4^-(H_2O)_n$, calculated with B3LYP/6-311++G(2d,2p). B = bisulfate and W = water.

The search for the most stable isomer for each of the $HSO_4^-(H_2O)_n$ clusters resulted in configurations displayed in Figure 20. The smallest $HSO_4^-(H_2O)_n$ structures (n = 1–5) were reproduced from those obtained in earlier studies [16, 163, 164]. In all instances, the water molecules form an interconnected hydrogen-bonded network centered at a HSO_4^- ion, in agreement with, *e.g.* [165]. No evidence of protolysis giving $(SO_4^{2-})(H_3O^+)(H_2O)_n$ clusters could be obtained in our calculations, although a similar event is known to occur [166].

4.2 Reactions of clusters with D_2O and hydrogen exchange

This section describes the outcome of reactions of the clusters containing H^+(pyridine)$_{1–3}$, protonated bipyridines, bisulfate or alkali metal ions with heavy water, analyzed in terms of value of fraction of exchange (Section 4.2.1) and the κ_{HDO} ratio (Section 4.2.2). Definitions of these quantities are given in Chapter 2 and 3. Computational study of proton transfer mechanism is discussed in Section 4.2.3.

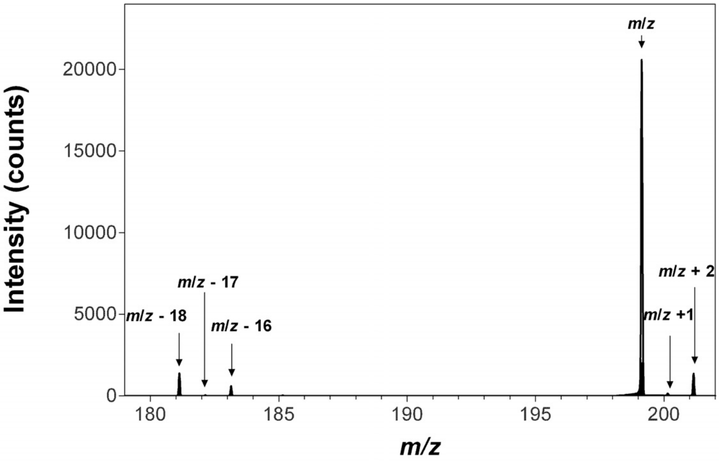

Figure 21. Peaks observed for the hypothetical reaction $M^+(H_2O)_n$ + D_2O. Peaks are indicated by their mass relative the parent ion peak *m/z*.

Figure 21 shows a constructed partial mass spectrum of the typical product peaks resulting from the hypothetical reaction $M^+(H_2O)_n$ + D_2O. As seen in the figure, the mass spectrum is dominated by the parent ion (*m/z*), the *m/z* – 18 peak is the product of evaporation from the reactant cluster. The *m/z* + 1 and *m/z* + 2 peaks represent the exchange products; in this case *m/z* + 1 is comparably small, indicating that cluster reacts mainly by ligand exchange. The post reaction evaporation results in loss of intensity from the *m*/*z* + 1 and *m*/*z* + 2 product peaks for the *m*/*z* – 17 and *m*/z – 16 peaks, respectively.

4.2.1 The fraction of exchange and relative cross section

Regarding the reaction of a cluster ion with D_2O the fraction of exchange for the selected cluster reads: $\Phi = I(m/z + 1) + I(m/z + 2)$ (Section 2.4.2). As mentioned previously, post reaction evaporation of water molecules from a product cluster reduces the observed fraction of exchange. Adding the intensities of the *m/z* – 17 and *m*/z – 16 peaks to the fraction of exchange Φ yields the corrected fraction of exchange

$\Phi_{\text{corr}} = I(m/z + 1) + I(m/z + 2) + I(m/z - 17) + I(m/\text{z} - 16)$

Since the D_2O pressure in the collision cell is not accurately known, only a relative cross section can be obtained. This was done by normalizing the cross sections for a water clusters of interest to a cross section for reference cluster: $OH^-(H_2O)_{10}$ or $H^+(H_2O)_{11}$ reacting with D_2O under the same conditions. The relative cross section becomes

$$\sigma_{\text{r}}(i) = \frac{\sigma(i)}{\sigma(r)} = \frac{A(i)}{A(r)} \tag{4.1}$$

where the absorbance $A = -\ln(I/I_0)$, *i* denotes a cluster of interest and *r* denotes the reference cluster. Further, the entity I/I_0 can be expressed through the fraction of clusters that react in the collision cell $I/I_0 = 1 - \Phi$, and $-\ln(1 - \Phi) \approx \Phi$, as generally in our studies $\Phi \leq 0.1$. The relative cross section provides a consistent measure of the cross sectional size dependence, and makes it possible to compare cross sections between different cluster types and experiments.

Since the general trends of corrected relative cross sections are similar for the cluster ions studied (although actual values and slope of the line may differ), only an example from Paper I is given. Figure 22 presents the relative cross section corrected for post reaction evaporation for an experiment where $H^+(\text{pyridine})_{0\text{–}3}(H_2O)_n$ clusters react with

D_2O at $E_{\text{com}} = 0.1$ eV. The cross sections are given relative to the uncorrected cross section of the $H^+(H_2O)_{11}$ cluster measured repeatedly during same experimental session.

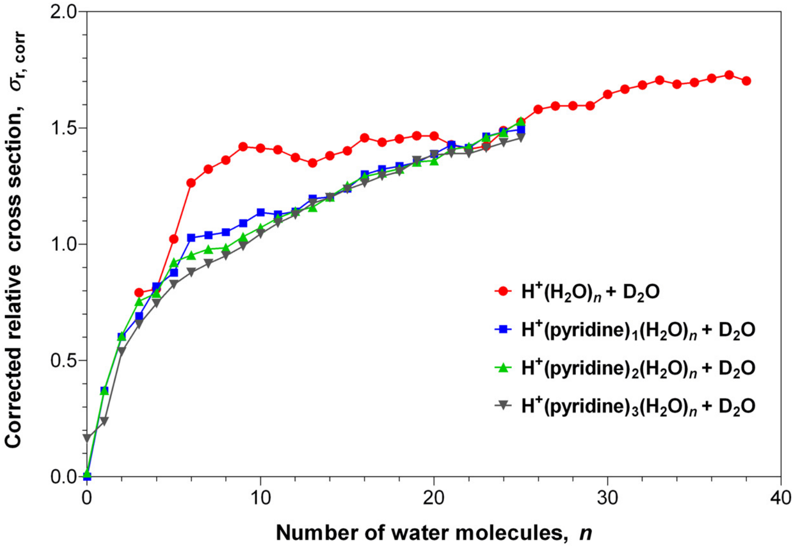

Figure 22. Relative cross sections for the reaction between clusters $H^+(\text{pyridine})_{0\text{–}3}(H_2O)_n$ and D_2O at 0.1 eV reduced collision energy.

The general trend is that the cross sections increase with the number of water molecules. The number of pyridine molecules in the cluster seems to have little effect for a given number of water molecules. Generally speaking, similar behaviour of the cross-section values is a common tendency for all studied species, and is an indication of a structural resemblance and broadly similar energetics of binding.

It is interesting that none of our studies gave any indication of correlation of the relative abundance of magic-number clusters neither with relative cross section nor with the degree of H/D exchange observed. It remains possible that such an influence might emerge in the limit of a comparably short reaction intermediate lifetime, where changes in cluster stability associated with magic numbers could allow for additional H/D rearrangement steps. Next, as discussed in Chapter 2.4.1, idea of a firm cluster structure is of limited value in this connection, since the clusters are floppy, allowing low energy routes for water molecule rearrangements and proton transfer. The occurrence of magic numbers has to invoke the entropic factor as well as the detailed kinetics of water evaporation during cluster formation, which was discussed by Hansen *et al.* [113] It appears that only two requirements that have to be fulfilled for efficient H/D exchange is a chemically favourable mechanism for proton migration plus a sufficiently long lifetime of the collision intermediate.

4.2.2 The κ_{HDO} ratio and H/D exchange

In order to obtain a quantitative measure of the amount of single proton (H/D) exchange events relative to intact water ligand exchange, we analysed all cluster series measured based on the ratio (Equation 2.19). The ratio κ_{HDO} is expected to vary from 0 (for a cluster with no H/D exchange) to a value representing evaporation of a random water molecule from a cluster with a completely random H/D distribution. Alternatively, as discussed previously (Section 2.4.2), in the presence of HDO contamination the "bottom" line for κ_{HDO} is shifted from 0 upwards.

Figure 23 shows the results of H/D exchange in reactions between size-selected clusters $H^+(\text{pyridine})_{0\text{–}3}(H_2O)_n$ and D_2O (Paper I) studied at $E_{\mathrm{com}} = 0.1$ eV ($E_{\mathrm{lab}} = 0.6$ eV was used for clusters ≤ 100 u). Also shown are the two theoretical curves corresponding to a purely randomized protium/deuterium exchange for an aqueous cluster containing $2n + 1$ hydrogens reacting with pure D_2O, and with D_2O having an impurity of HDO, estimated to be around 4%. As seen in Figure 23, the $H^+(\text{pyridine})_1(H_2O)_n$ clusters in reactions with D_2O behave similarly to the $H^+(NH_3)_1(H_2O)_n$ clusters [126], allowing one to assume that the proton is immobile in this cluster. This can be explained on the basis of the high basicity of pyridine as in the case of ammonia. This also agrees with results of theoretical investigation of $H^+(\text{pyridine})_1(H_2O)_{1\text{–}6}$ given in Section 4.1.3, with regard to the extra proton being strongly bound to the nitrogen site.

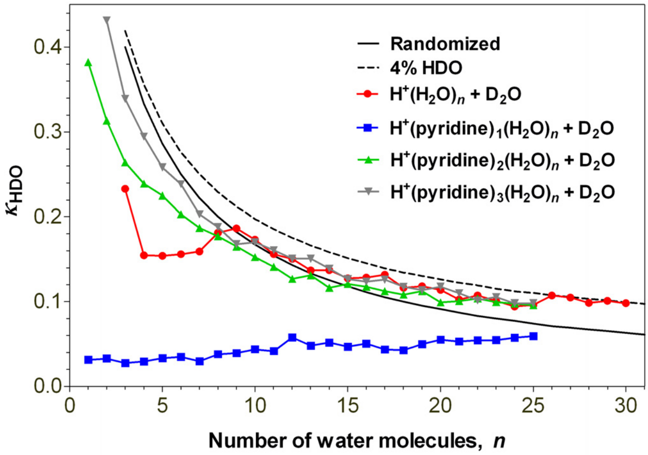

Figure 23. κ_{HDO} for clusters $H^+(H_2O)_n$ and $H^+(pyridine)_{1–3}(H_2O)_n$ reacting with D_2O. Also included are curves representing expected κ_{HDO} values for a water cluster with a completely randomised hydrogen distribution in the case of 0% and 4% HDO contamination.

The most remarkable result of the present study is that the protonated clusters containing two or three pyridine molecules exhibit complete hydrogen scrambling in the same way that $H^+(H_2O)_n$ clusters do [126]. At first sight this appears surprising, since chemical intuition would predict that the presence of an extra basic molecule would decrease acidity, thereby suppressing the acid catalysed H/D exchange process even more. This result may indicate that the proton in $H^+(pyridine)_{2–3}(H_2O)_n$ clusters becomes free to move around, thereby inducing H/D rearrangements in the reaction intermediate.

Next, the κ_{HDO} for the reaction between $MH^+(H_2O)_n$ (M = bipyridine, n = 1–30) clusters and heavy water are given in Figure 24 (Paper VII). This set of species is meant to resemble $H^+(pyridine)_2(H_2O)_n$ structurally, and may exhibit similar H/D-exchange characteristics. First, the fraction of exchange reactions leading to loss of HDO for clusters containing 4,4’-BiPy or 4,4’-EtBiPy is systematically low (see Figure 24). On the other hand, according to the data presented in Figure 24, water clusters with 2,2’-BiPy and 2,2’-EtBiPy exhibit significant activity for H/D exchange, particularly for the latter.

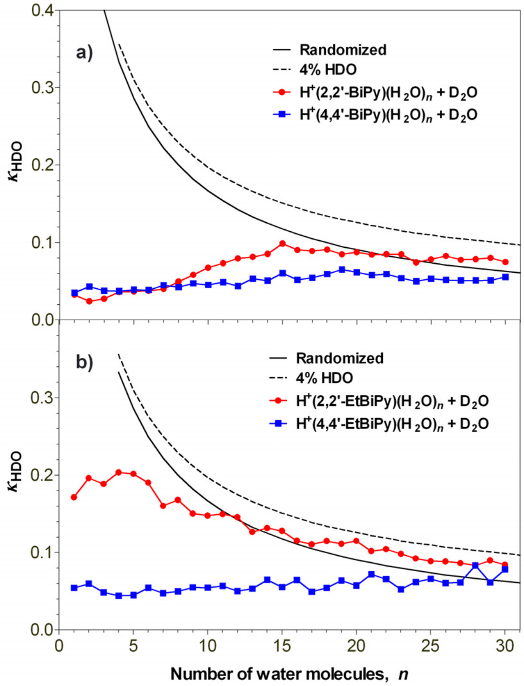

Figure 24. The fraction of exchange-reactions leading to loss of HDO from the reaction intermediate (κ_{HDO}) for the reaction between $MH^+(H_2O)_n$ (M = 2,2'-BiPy, 4,4'-BiPy, 2,2'-EtBiPy, 4,4'-EtBiPy) with D_2O. The solid line represents the theoretical κ_{HDO} curve for a cluster with $2n + 1$ protons and 2 deuteriums after complete H/D scrambling. The dashed line is corrected for the 4% HDO contamination of the heavy water in the collision cell.

Figure 25 depicts the κ_{HDO} ratios measured for the bisulfate containing water clusters $HSO_4^-(H_2O)_n$ (Paper II). Inspection of the plot reveals that the κ_{HDO} ratio is initially small, however it increases in the transition region $n = 8$–13, and then seems to follow statistically randomized line for the larger clusters. Thus, the experiments suggest that hydrogen rearrangements are ineffective in $HSO_4^-(H_2O)_n$ clusters, unless the degree of hydration reaches a specific level.

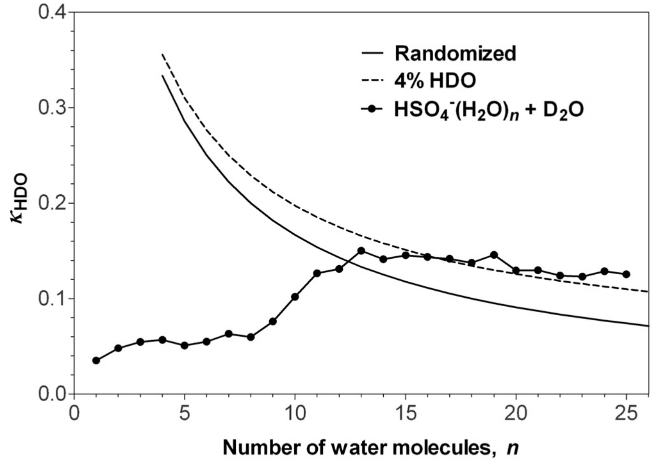

Figure 25. The κ_{HDO} ratios for the bisulfate-containing clusters $HSO_4^-(H_2O)_n$ reacting with D_2O. The solid line represents the theoretical κ_{HDO} curve, the dashed line is corrected for the 4% HDO contamination.

Given features of proton transfer in water clusters containing pyridine, bipyridine and bisulfate ions will be discussed in the next section on the basis of quantum chemical simulations in terms of relation between proton transfer properties of this particular group of clusters and the intrinsic properties of the central ion.

4.2.3 Quantum chemical calculations of proton transfer mechanisms

With regard to the H/D-experiments described above it would be useful to get insight into the energy requirements for proton transfer from one site to another within cluster. As discussed, swift proton mobility within the reaction intermediates is a requirement for H/D exchange to take place [111, 123, 124].

A set of quantum chemical calculations was done on small pyridine-containing clusters (Paper I) to interpret the experimental observations regarding the reactions with D_2O. As discussed in Section 4.1.3, the most stable cluster structures for $H^+(pyridine)_1(H_2O)_{1-6}$ have the extra proton firmly bonded to the nitrogen atom, which explains the absence of proton transfer within the intermediates. As such, the proton is not free to facilitate H/D exchange reactions, and these clusters will consequently react with D_2O mainly by ligand exchange, resulting in consistently low values for κ_{HDO}. Thus, the quantum chemical observations and experimental results are in good agreement at this point.

Our next aim was to explain the unexpected activity of $H^+(pyridine)_2(H_2O)_n$ in H/D transfer reactions. The experiments indicate particularly high κ_{HDO} values for the smallest clusters with two pyridine molecules, which is an evidence for enhanced proton mobility, while the calculations indicate that there are no stable structures with the extra proton attached to a water molecule (Section 4.1.3). Although all optimum structures found for $H^+(pyridine)_2(H_2O)_n$ clusters have the proton bound to one of the pyridine cores (just like for $H^+(pyridine)_1(H_2O)_n$ clusters), a search for a mechanism of proton transfer through the water network of the cluster was performed. It is known that protons transfer quickly along hydrogen bond wires [133]. This picture seems to be realized for the transition structures depicted in Figure 26, where the proton is relocated from one pyridine onto another by a pronounced relay mechanism.

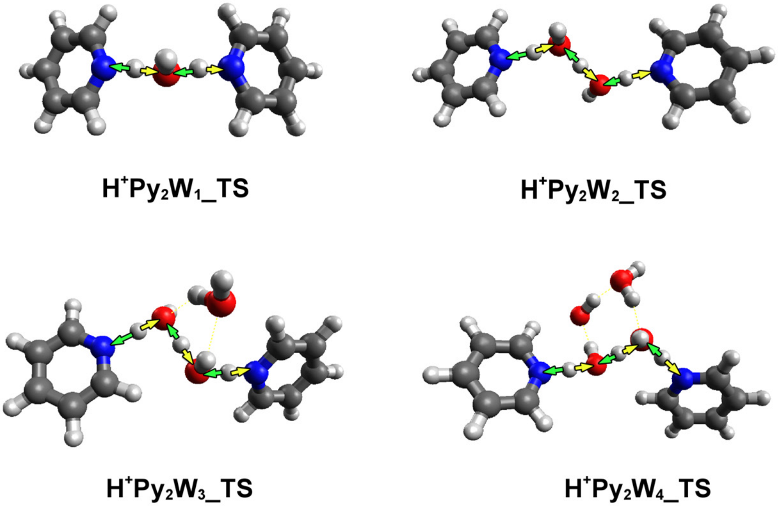

$H^+Py_2W_1$_TS **$H^+Py_2W_2$_TS**

$H^+Py_2W_3$_TS **$H^+Py_2W_4$_TS**

Figure 26. Transition structures (TS) for reversible relay proton transfer in clusters with 2 pyridine molecules (Py) and 1–4 H_2O (W). The arrows indicate proposed reaction coordinate.

The results show that for a $H^+(pyridine)_2(H_2O)_1$ cluster the barrier for reversible transfer of protonation between the two nitrogen atoms is essentially zero. Increasing the length of the wire to two molecules results in an increased value of the barrier height, although the barrier is still permeable (Table 1). This means that the proton in a cluster containing two pyridines is sufficiently free to support a complete H/D randomization, exhibiting itself in the high values of κ_{HDO} observed for $H^+(\text{pyridine})_2(H_2O)_n$ clusters.

Table 1. Barrier heights (energy difference between TS and minimum energy structure, in kJ mol^{-1}) for proton transfer in $H^+(\text{pyridine})_2(H_2O)_n$, calculated with B3LYP/6-311+G**.

n	Label (Figure 26)	Barrier height
1	$H^+Py_2W_1$_TS	*-1.6*
2	$H^+Py_2W_2$_TS	*5.9*
3	$H^+Py_2W_3$_TS	8.0
4	$H^+Py_2W_4$_TS	14.9

At this point it is useful to revisit the results of H/D experiments on bipyridine water clusters mentioned in Section 4.2.2. In the experiments with D_2O it was found that for 4,4’-bipyridines only a small portion of the reactions is likely to involve O–H bond activation and intra-cluster H/D rearrangements during the lifetime of the reaction intermediate. This can be understood from the fact that the two nitrogen atoms in the 4,4’-bipyridines are spatially separated, and unable to effectively support the above-mentioned relay mechanism through a short bridge of water molecules. In other words, in line with the conclusions of the previous studies (Ref. [126] and results from Paper I) we propose that the low proton exchange observed in these clusters is likely due to hindered proton migration; a consequence of the unfavourable steric arrangement of the nitrogen atoms in 4,4’-BiPy and 4,4’-EtBiPy.

On the other hand, the high activity of 2,2’-bipyridines in H/D exchange reactions is most likely a consequence of the ease of formation of hydrogen bond wires enabled by the favourable spatial arrangement of nitrogen atoms in these clusters. The wires, in turn, serve as a perfect medium for proton migration. Generally lower κ_{HDO} values of 2,2’-BiPy compared to 2,2’-EtBiPy can be explained in terms of the cavity that exists between the nitrogen atoms, which in the case of 2,2’-BiPy is unlikely to be wide enough to effectively accommodate one or two water molecules. The flexible ethylene bridge in 2,2’-EtBiPy most likely enables the molecule to adjust the size of the cavity to comfortably house water molecules in a conformation that allows proton hopping between the nitrogen atoms, and thus hydrogen exchange. Inspection of simple molecular models using standard values for bond distances and angles shows that this is possible (Figure 27).

The results present strong support for the proposed mechanism of concerted proton migration through a wire of water molecule hydrogen bonds bridging the two basic centers.

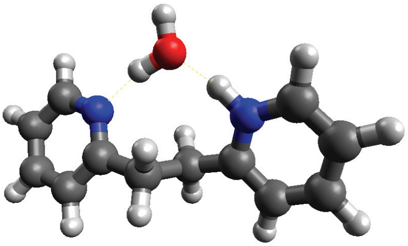

Figure 27. Schematic presentation of a cluster consisting of 2,2’-ethylenebipyridine, one water molecule, and a proton, built with Avogadro 1.0.3 molecule editor.

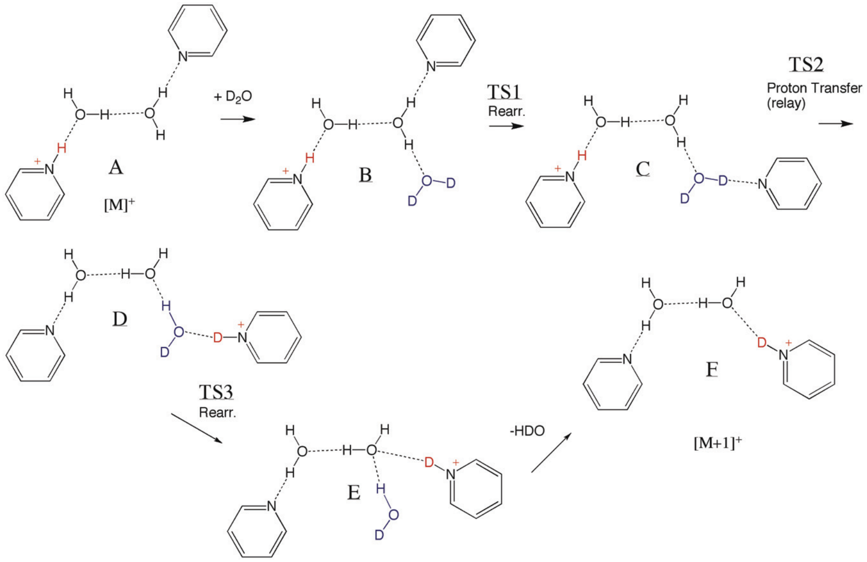

Figure 28. Proposed mechanism for H/D exchange in water clusters containing two pyridine molecules.

On the basis of the structural and energetic findings reported above, we can propose a general mechanism for H/D exchange during the existence of the intermediate formed upon encounter between $H^+(\text{pyridine})_2(H_2O)_n$ and D_2O. The mechanism is sketched in Figure 28, and is in full agreement with the results obtained from the quantum chemical calculations (Paper I).

The search for a similar H/D exchange mechanism for bisulfate-containing clusters was also performed (Paper II). The transition state geometries are presented in Figure 29. According to the calculations, the transfer process in clusters $n = 2–10$ generally involves a common structural motif consisting of a hydrogen bond bridge of two water molecules and the bisulfate molecule. The proton is transferred from HSO_4^- through a water wire and back to the bisulfate ion according to pendular variant of the Grotthuss mechanism. The barrier height values for these transition structures (the difference between energies of the transition structure and the most stable structure) are given in Table 2. The size dependency of the barrier heights for proton transfer according to this relay mechanism has a noticeable decreasing feature, implying that effectiveness of this transfer mechanism should increase for larger clusters, $n = 9$ and 10. It appears that H/D exchange is promoted in large clusters relative to small; thus the model explains the size-dependence of proton mobility observed experimentally for the bisulfate-containing clusters.

Interestingly, the energy barrier for this mechanism (Table 2) reaches its minimum value for $n = 9$, exactly the size where transition to higher κ_{HDO} in Figure 29 happens. Also, energy requirement for concerted proton migration for $HSO_4^-(H_2O)_{9–10}$ is around just 15 kJ mol^{-1}, which is notably close to barrier height observed in similar calculations on $H^+(\text{pyridine})_2(H_2O)_{2–4}$ in Paper I (taking into account the slightly different computational methods used and margin of errors). It therefore seems that proton transfer processes with barrier height below 15–20 kJ mol^{-1} are likely to be highly effective and observed in the reaction results and *vice versa*. However, this is just an observation, requiring careful validation.

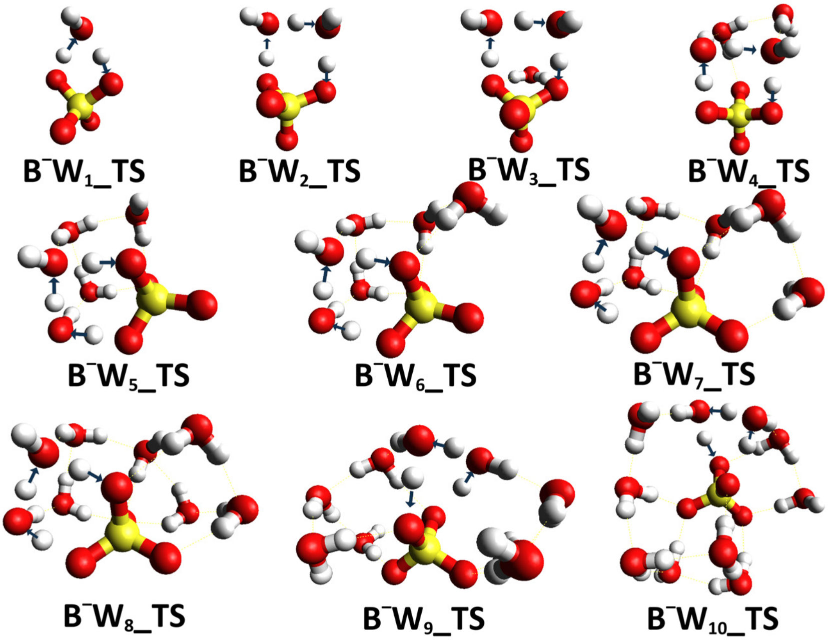

Figure 29. Transition states for proton transfer in bisulfate-containing clusters, from Paper II. Labelling: B = HSO_4, W = water.

Table 2. Barrier height (at 0 K) for the transition structures in Figure 29, as calculated in Paper II. Values are given in kJ mol^{-1} for a variable number of water molecules in the cluster, *n*.

n	1	2	3	4	5	6	7	8	9	10
barrier height	43.1	49.2	60.3	39.8	39.2	34.3	31.8	30.5	15.1	17.4

4.2.4 Alkali metal clusters. HDO contamination correction

Finally, the results of a separate study on H/D exchange in reactions between size-selected $M^+(H_2O)_n$ (M = Li, Na, K, Rb and Cs, n = 1–30) clusters and heavy water are presented. Figure 30 shows κ_{HDO} for all the clusters studied in Paper VI. The fraction of exchange-reactions leading to loss of HDO for all the studied clusters is systematically low. This indicates that the great majority of the exchange reactions come from intact ligand swap resulting in loss of H_2O molecules from $[M^+(H_2O)_nD_2O]^*$ intermediates.

A series of quantum-chemical calculations provides insight. Geometries of $A(H_2O)_n$ ($A = H_2O$, Li^+, Na^+, $n = 3–8$) clusters, studied in Paper VI adapted from [167-171] and recalculated at CAM-B3LYP/aug-cc-pVDZ, allow one to make an important observation. In the pure water clusters the water molecules form interconnected networks of hydrogen bonds, while in the small $M^+(H_2O)_n$ clusters (M = Li, Na) the alkali metal ion occupies the central position, thereby disrupting the network. Only for larger clusters, above $n = 4$, the water molecules in the solvation shell are sufficiently free to form hydrogen bonds.

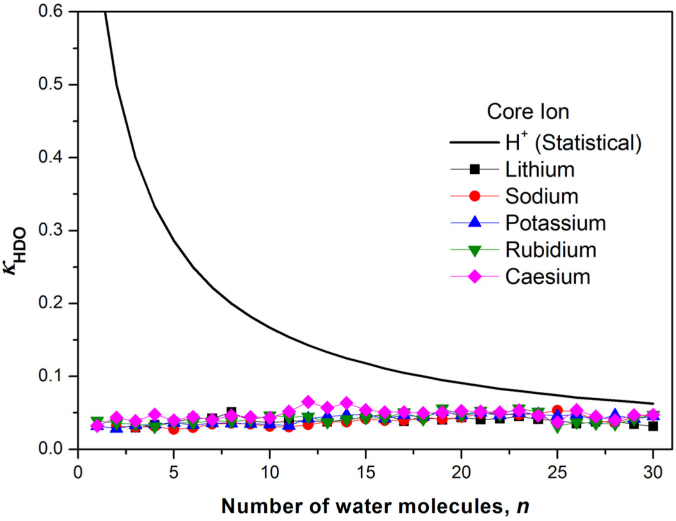

Figure 30. The κ_{HDO} ratio for alkali-metal–water clusters $M^+(H_2O)_n$ reacting with D_2O.

On the basis of our results on pyridinium and bisulfate water clusters (results from Papers I and II), we decided to search for the most likely mechanism for synchronous transfer of protons along preformed wires of water molecules interconnected by hydrogen bonds. It turned out that this, at least in principle, can be found in ring structures consisting of four or five water molecules.

The lowest energy transition structures located for each cluster size according to this relay mechanism are shown in Figure 31 for $(H_2O)_n$ and for $Li^+(H_2O)_n$. The geometries for $Na^+(H_2O)_n$ are closely similar to those for $Li^+(H_2O)_n$ and not shown. The corresponding barrier heights are given in Table 3. For water clusters containing alkali-metal ions the barrier height is significantly higher than in pure water clusters of the same size, especially for the smallest clusters. These trends are caused by the fact that in order to form the ring structures necessary to promote the relay mechanism, water molecules need to move out of the inner solvation shell of the alkali-metal ion. By increasing the size of the $M^+(H_2O)_n$ cluster up to $n = 7$ the barrier height decreases and approaches that of pure water clusters since it is no longer necessary to adjust the inner solvation shell. Although we do not claim high accuracy in the figures listed in Table 3, the trends appear clear since our findings agree well with the isotope exchange experiments (Figure 30). H/D exchange is catalysed by the presence of free protons, since the barrier height for proton transfer in a protonated water cluster is about 10 kJ mol^{-1} [111, 127, 133]. Judging by huge values of barrier height (Table 3), alkali metal ions do not promote isotope exchange to any degree. On the other hand, based on relatively high values for barrier height for $(H_2O)_n$ clusters (Table 3), it is likely that these clusters appear to be a less favourable medium for proton transfer reactions than protonated water clusters and for example clusters containing 2 pyridine molecules.

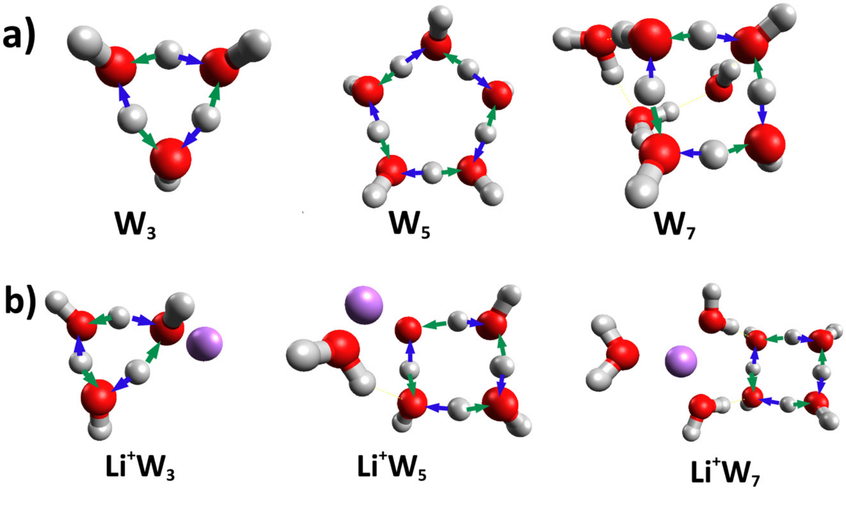

Figure 31. Proton transfer transition structures for clusters a) $(H_2O)_n$ and b) $Li^+(H_2O)_n$ as calculated with CAM-B3LYP/aug-cc-pVDZ. The hydrogens displacing along the reaction co-ordinate are indicated. In the labelling W stands for water.

Table 3. Barrier heights $E^{\#}$ (0 K), in kJ mol^{-1} for proton transfer within $M^+(H_2O)_n$ and $(H_2O)_n$.

$(H_2O)_n$		$Li^+(H_2O)_n$	
n	$E^{\#}$	n	$E^{\#}$
3	86.2	3	186.9
4	67.3	4	143.5
5	61.3	5	121.9
6	55.8	6	86.7
7	55.2	7	67.4
8	57.7	8	68.2

From the experiment the κ_{HDO} ratio was estimated for all alkali-metal–water cluster series measured. However, the measurements were all performed at slightly different conditions, most notably the level of HDO contamination of the D_2O reactant gas varied from experiment to experiment. If ligand exchange is the only exchange mechanism possible within a cluster then the apparent κ_{HDO} should increase linearly with the actual amount of HDO impurity, *i.e.* a contamination level of 5% will increase the measured κ_{HDO} value by 0.05. By calculating the κ_{HDO} value of the reference cluster ($H^+(H_2O)_{11}$) measured throughout the series at regular intervals and comparing to the expected value for a cluster with full hydrogen scrambling at 0% HDO contamination an effective degree of contamination could be estimated at certain points along the series $n = 1–30$. These points were then linearly interpolated, creating a curve with the degree of HDO contamination as a function of n. The contamination curve was subtracted from the measurements, producing a “normalized” κ_{HDO} curve. Some data points were removed due to having a too low signal-to-noise ratio, and the selected resulting datasets for each core ion are shown in Figure 30.

As seen, even with the correction for varying levels of HDO contamination, the curves are found to lie slightly above the zero level. This might be due to a number of reasons, in principle including the possibility that the clusters actually exhibit H/D exchange to some degree. However, it should be noted that the reference cluster used in all these measurements, $H^+(H_2O)_{11}$, tends to fall closer to the statistical 0% HDO curve than to the corresponding curve corrected for the HDO contamination [126]. That is, use of this particular reference cluster is likely to result in underestimating the calculated HDO contamination level. Contamination-corrected κ_{HDO} values for alkali-cluster series can further be used as benchmarks in further studies of H/D-exchange reactions.

4.3 Reactions of clusters with NH_3

This chapter brings the most important findings from our experiments with NH_3 *as reactant gas done using the QTOF mass spectrometer. The investigated species are:* $H^+(H_2O)_n$, $H^+(pyridine)_1(H_2O)_n$, $H^+(pyridine)_2(H_2O)_n$ *and* $H^+(NH_3)(pyridine)_1(H_2O)_n$. *First, the results for clusters with n up to 15 were used to improve a comprehensive model of ion concentrations in the troposphere (Section 4.3.1). Then size range of n = 16–27 was thoroughly investigated to unify findings with regard to magic cluster numbers (Section 4.3.2).*

4.3.1 Reactions with NH_3 and kinetic modelling

Reactions between pyridine containing water cluster ions, $H^+(\mathrm{pyridine})_{0\text{–}2}(H_2O)_n$ and $H^+(NH_3)(\mathrm{pyridine})_1(H_2O)_n$ (n up to 15) with NH_3 have been studied experimentally.

According to the model of Beig and Brasseur [45], pyridine-containing clusters are of possible substantial importance for the chemistry of the lower troposphere. The authors suggested two reaction pathways for the formation of these pyridinated cluster ions from protonated water clusters. The reactions are given below, where X represents pyridine, picoline or lutidine.

Pathway A

$$H^+(H_2O)_n + mNH_3 \rightarrow H^+(NH_3)_m(H_2O)_n \qquad (4.2)$$

$$H^+(NH_3)_m(H_2O)_n + X \rightarrow H^+(X)_1(NH_3)_{m-x}(H_2O)_{n-y} + xNH_3 + yH_2O \qquad (4.3)$$

Pathway B

$$H^+(H_2O)_n + X \rightarrow H^+(X)_1(H_2O)_{n-1} + xH_2O \qquad (4.4)$$

$$H^+(X)_1(H_2O)_n + mNH_3 \rightarrow H^+(NH_3)_m(H_2O)_n + X \qquad (4.5)$$

$$H^+(NH_3)_m(H_2O)_n + X \rightarrow H^+(X)_1(NH_3)_{m-x}(H_2O)_{n-y} + xNH_3 + yH_2O \qquad (4.6)$$

The rate of Reaction (4.5) is unknown, therefore the experimental investigation of Paper III aimed to identify its products and to find the reaction rate coefficient for it. The other reactions presented above have been studied by Viggiano *et al.* for X = pyridine [70, 172].

The relative reaction rate coefficients determined in the experiments in Paper III are given in Figure 32 as a function of the number of water molecules in the cluster, *n*. They were measured at a center-of-mass collision energy of 0.085 eV (8 kJ mol^{-1}) and are all expressed relative to the total rate coefficient for $H^+(H_2O)_4 + NH_3$ from [70]. Overall, the obtained rate coefficients increase rapidly for $n = 1–4$ and level off at $n = 5$ for any cluster type.

It was found that addition reaction between the clusters and ammonia led to subsequent loss of water molecules: 2–3 H_2O in the case of pure water clusters and generally 2 H_2O for pyridine-containing clusters. Our experiments have not indicated any significant degree of evaporation of pyridine from clusters. The estimated maximum relative rate coefficient for loss of pyridine was 50 times lower than the rate assumed in [45]. Further, we have not seen any indication that clusters containing two pyridine molecules should be less stable than clusters with one pyridine.

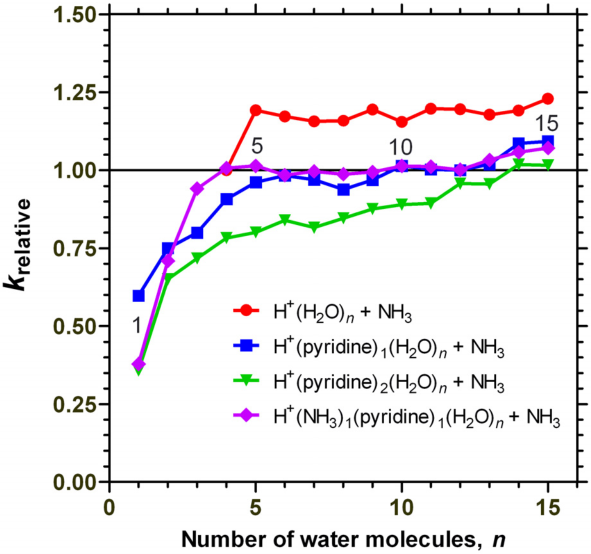

Figure 32. Relative rate coefficients for the clusters $H^+(pyridine)_m(H_2O)_n$ (with $m = 0$ to 2) and $H^+(pyridine)_1(NH_3)_1(H_2O)_n$ reacting with NH_3 normalized to the rate coefficient for $H^+(H_2O)_4 + NH_3$.

The results obtained from this study were used to construct a kinetic model for the growth rates and abundances of cationic clusters at ground level (see details for Model

A in Paper III). The model is a modification of one employed by Beig and Brasseur [45], and includes two adjustments based on experimental results. Firstly, Reaction (4.5) was replaced with the reaction $H^+(X)_1(H_2O)_n + NH_3 \rightarrow H^+(NH_3)_1(X)_1(H_2O)_n$, for which the experimentally determined rate coefficient was used. Secondly, we included reactions leading to clusters containing two amines (pyridine, picoline and lutidine).

The modelling results (Figure 33) were in good agreement with those of Beig and Brasseur with regards to the modelled concentration of pyridinated clusters. However, the model of Beig and Brasseur only allowed for a single pyridine in a cluster. While from Figure 33 it is clear that more than one pyridine molecule may be present in the cluster ions in the atmosphere for the high pyridine concentrations. According to the measurements, the pyridine concentration can be as high as 7×10^7 cm^{-3} at 298 K [49]. Our modelling work suggests that at these pyridine concentrations clusters containing two pyridine molecules could be the dominant cluster ion in the troposphere.

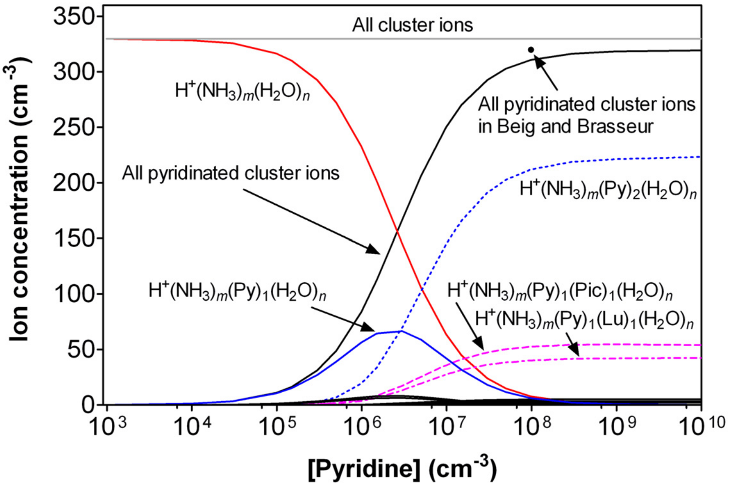

Figure 33. Results from the tropospheric cation model for ground level conditions from Paper III (Model A): concentration of cluster ions given as a function of the tropospheric pyridine concentration.

4.3.2 Branching ratios and magic numbers

The abundance spectra and evaporation patterns (Sections 4.1.1 and 4.1.2) show that $H^+(NH_3)_1(\text{pyridine})_1(H_2O)_n$ clusters have magic numbers for the same number of water molecules observed for $H^+(NH_3)_1(H_2O)_n$ clusters, and may share similarity with the magic numbers for $H^+(H_2O)_n$ [126]. However, $H^+(\text{pyridine})_m(H_2O)_n$ clusters do not exhibit any magic-number behaviour. Measurement of branching ratios for cluster reactions with NH_3 allowed us to investigate this matter further.

As discussed in Paper III and IV, there may be overlapping peaks in mass spectra between product ions due to the fact that parent ion can lose several water molecules before reaction. It is possible to correct the measured branching ratios for the contribution of evaporation of water prior to reaction. However, for the sake of consistency with Paper III, where no such correction was performed, Figure 34(a–d) shows the uncorrected branching ratios for reactions with NH_3 for all clusters investigated: $H^+(H_2O)_n$, $H^+(\text{pyridine})_1(H_2O)_n$, $H^+(\text{pyridine})_2(H_2O)_n$ and $H^+(NH_3)_1(\text{pyridine})_1(H_2O)_n$ (n = 16–27) calculated from the peak intensities measured in the experiments and shown on a linear scale. It is evident from Figure 34 that the magic numbers have a big effect on branching ratios for evaporation.

Addition of NH_3 to pure water clusters (Figure 34a) results in the loss of two or three water molecules. However, several irregularities attract attention: for example for the $H^+(H_2O)_{22}$ cluster, formation of $H^+(NH_3)_1(H_2O)_{20}$ is clearly preferred over formation of $H^+(NH_3)_1(H_2O)_{19}$. The branching ratios are significantly enhanced for reaction channels leading to the magic cluster ion $H^+(NH_3)(H_2O)_{20}$, for example, both $H^+(H_2O)_{22}$ and $H^+(H_2O)_{23}$ mainly give $H^+(NH_3)(H_2O)_{20}$ upon reaction with ammonia. In addition, the fact that the $H^+(H_2O)_{21}$ cluster is itself a magic number cluster does not seem to influence the branching ratios. The branching ratios are in agreement with the results obtained from the abundance spectra and the evaporation patterns for $H^+(NH_3)_1(H_2O)_n$ [126].

From Figure 34b–c we see that reactions between clusters containing one and two pyridine molecules and ammonia for $n \leq 22$ are dominated mainly by pick-up of ammonia and loss of two water molecules. However, remarkably high branching ratios are found for reaction channels leading to $H^+(NH_3)(\text{pyridine})_m(H_2O)_n$, with n = 18, 20, 22, *i.e.*, for the channels producing the magic numbers. For example, for reaction

$H^+(pyridine)_{1–2}(H_2O)_{20} + NH_3$ the $–2H_2O$ branching ratio is greatest, showing formation of the $H^+(NH_3)_1(pyridine)_{1–2}(H_2O)_{18}$ cluster. Further, $–3H_2O$ is the dominant product for the reaction $H^+(pyridine)_{1–2}(H_2O)_{23} + NH_3$, indicating formation of a magic number cluster for $H^+(NH_3)_1(pyridine)_{1–2}(H_2O)_{20}$ (Figure 12).

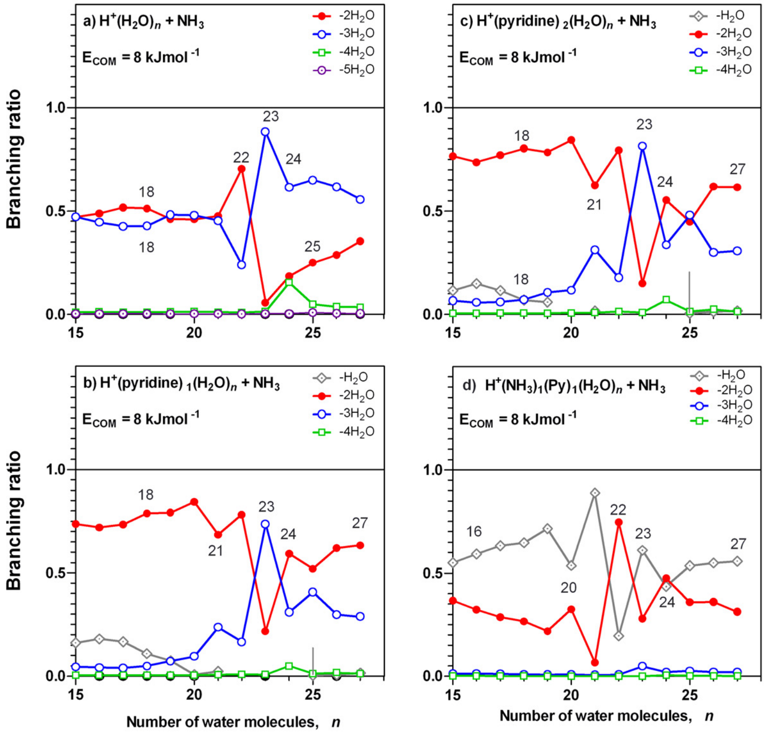

Figure 34. Branching ratios for clusters reacting with NH_3 as measured in the experiments, without correction for the peak intensity.

The reaction $H^+(NH_3)_1(pyridine)_1(H_2O)_n + NH_3$ (Figure 34d) mainly leads to the loss of one or two water molecules. The trends in the branching ratios again show enhanced branching ratio for the reaction channel forming clusters with $n = 18$, 20 and 22, while the adjacent reaction channel is suppressed. However, in this case, the product magic clusters all contain two NH_3 molecules.

The computational results of Paper I show that in $H^+(pyridine)_m(H_2O)_n$ clusters the proton is attached to the nitrogen of one of the pyridine molecules, while a separate network of water molecules is attached to the pyridinium ion by a hydrogen bond (Section 4.1.3). It could therefore be possible that the removal of the proton from the water network is responsible for the loss of magic numbers in pyridinated cluster ions.

On the other hand, quantum chemical calculations (Paper IV) indicate that protonated water clusters containing one ammonia and one pyridine molecule have the general formula (pyridine)$(NH_4^+)(H_2O)_n$, stabilized by hydration of the ammonium core. This would also explain the reoccurrence of magic numbers; the proton is now back in the hydrogen-bonded network, attached to NH_3 molecule. However, it is necessary to note that proton-free alkali-metal–water clusters with pronounced magic-number behaviour (M = K–Cs) do not fit into this simple speculation.

5 Conclusions

The occurrence of magic number peaks in the mass spectra has been investigated for all clusters of interest. No clear magic numbers were observed for H^+(pyridine)$_{1\text{-}3}$(H_2O)$_n$ clusters or clusters containing bipyridines, except there is increased intensity of the molecular ion signal. However, magic numbers were observed for clusters of the type $H^+(NH_3)_1$(pyridine)$_m$(H_2O)$_n$ (m = 1, 2) and for clusters of the type $H^+(NH_3)_2$(pyridine)$_1$(H_2O)$_n$. Furthermore, these magic numbers coincide with the magic numbers for $H^+(NH_3)_1(H_2O)_n$, previously found for n = 18, 20 and 27 [126].

A proposed explanation for the difference in terms of magic numbers between H^+(pyridine)$_m$(H_2O)$_n$ and $H^+(NH_3)_1$(pyridine)$_m$(H_2O)$_n$ is the possible difference in structure between these closely related species. According to calculations H^+(pyridine)$_m$(H_2O)$_n$ has the proton attached to the pyridine molecule—outside the hydrogen bonded water network. The pattern of the observed magic numbers and results of high-level ab initio calculations of small protonated pyridine/ammonia/water clusters suggest that $H^+(NH_3)$(pyridine)(H_2O)$_n$ have structures consisting of a $NH_4^+(H_2O)_n$ core with the pyridine molecule hydrogen-bonded to its surface, in analogy with $H^+(H_2O)_n$ and $H^+(NH_3)_1(H_2O)_n$ clusters.

Reactions of water-containing clusters with D_2O indicate how easily various clusters are able to transfer proton between different protonation sites. Inclusion of basic compound like ammonia [126] or pyridine prevents hydrogen scrambling in water clusters, due to tight bonding of the extra proton to a basic molecule. However, addition of a second or even third pyridine molecule provides two equally attractive sites of protonation and returns proton mobility to a level corresponding to a completely statistical composition of the leaving water molecule. Proton transfer capability was evidenced from the emission of HDO from the reaction intermediate and is supported and explained by a quantum chemical study. Quantum chemical calculations also suggest that proton mobility in clusters containing two pyridine molecules is due to a relay mechanism whereby the site of protonation is transferred from one nitrogen atom to the other along a pre-aligned wire of hydrogen bonds. A similar mechanism was suggested to play a role in H/D-exchange activity of 2,2'-bipyridines, maintaining proton transfer through a preformed wire of water molecules. In accord with expectations, 4,4'-bipyridines show little to no proton mobility in reactions with D_2O, probably due to steric complications in forming a wire of water molecules between nitrogen atoms.

A relay mechanism was also suggested as the explanation for the proton scrambling taking place in bisulfate-containing clusters, $HSO_4^-(H_2O)_n$. In present case the same bisulfate ion provides both termini for proton transfer. Bisulfate-water clusters exhibit full hydrogen scrambling only when the degree of hydration reaches a level $n = 8$ and higher. This size coincides with changes in the energy barrier associated with the proton transfer mechanism, which drops from 50–30 kJ mol^{-1} to around 16 kJ mol^{-1} for $n = 9$ and 10.

Reactions of size-selected $M^+(H_2O)_n$ ($n = 1$–30, M = Li, Na, K, Rb or Cs) with D_2O show that the rates of protium/deuterium exchange, when properly corrected for contamination of the D_2O, are consistently extremely low. These results support the fact that alkali-metal–water clusters are essentially inert in H/D exchange reactions with water, making them ideal for benchmarking in future studies.

The degree of hydrogen scrambling or reaction cross section was not affected by magic numbers in any experiment. However, the magic numbers did influence the degree to which clusters lost additional water molecules after fragmentation of the reaction intermediate.

Results from cross section measurements for the reaction of protonated pyridine/water clusters with NH_3 were used to improve an existing kinetic cluster ion model under tropospheric conditions [45]. The improved model indicates that the positive cluster-ion spectrum at ground level may be dominated by clusters containing more than one pyridine molecule, in addition to water and ammonia.

6 Acknowledgements

First of all, I would like to thank Prof. Einar Uggerud, the leader of the **Physical Chemistry** group and the principal supervisor of this thesis, for his support and interest. He has been a constant source of advice and guidance in my activities. Also I thank my subsidiary supervisors, Trygve Helgaker and Svein Samdal for their assistance and co-operation.

I am extremely grateful to Mauritz Ryding and Patrik Andersson. Almost from my very first day in Oslo I was pleased by their support, patience in answering countless questions and willingness to teach me everything they knew.

Osamu Sekiguchi and John Vedde deserve special thanks for their help and constant technical assistance. All collaborators and colleagues as well as members of the CTCC group are also gratefully acknowledged for their help and co-operation.

Last but not least, I would like to thank Anton Simakov and Vladimir Rybkin for support and for help with proofreading, your valuable comments are greatly appreciated.

7 References

[1] IPCC, Summary for Policymakers, in Climate Change 2007: The Physical Science Basis. Contribution of Working Group I to the Fourth Assessment Report of the Intergovernmental Panel on Climate Change, in: S. Solomon, D. Qin, M. Manning, Z. Chen, M. Marquis, K.B. Averyt, M. Tignor, H.L. Miller (Eds.), 2007.
[2] R.P. Wayne, Chemistry of Atmospheres, 3rd ed., Oxford University Press: Cambridge, United Kingdom and New York, NY, USA, 2000.
[3] O.E. Allen, Planet Earth: Atmosphere, Alexandria, Va.: Time-Life Books Inc., 1983.
[4] F.K. Lutgens, E.J. Tarbuck, Atmosphere, The: An Introduction to Meteorology, 11th ed., Prentice Hall, 2010.
[5] W.C. Hinds, Aerosol Technology, 2nd ed., John Wiley & Sons, 1999.
[6] B.J. Finlayson-Pitts, J.N. Pitts, Chemistry of the Upper and Lower Atmosphere, Academic Press: San Diego, USA, 2000.
[7] M. Kulmala, How Particles Nucleate and Grow, Science, 302 (2003) 1000-1001.
[8] U. Pöschl, Atmospheric Aerosols: Composition, Transformation, Climate and Health Effects, Angew. Chem. Int. Ed., 44 (2005) 7520-7540.
[9] P. Hoet, I. Bruske-Hohlfeld, O. Salata, Nanoparticles - known and unknown health risks, J. Nanobiotechnology, 2 (2004) 12.
[10] C.A. Pope, M. Ezzati, D.W. Dockery, Fine-Particulate Air Pollution and Life Expectancy in the United States, N. Engl. J. Med., 360 (2009) 376-386.
[11] S. von Klot, A. Peters, P. Aalto, T. Bellander, N. Berglind, D. D'Ippoliti, R. Elosua, A. Hormann, M. Kulmala, T. Lanki, H. Lowel, J. Pekkanen, S. Picciotto, J. Sunyer, F. Forastiere, H.S. Grp, Ambient air pollution is associated with increased risk of hospital cardiac readmissions of myocardial infarction survivors in five European cities, Circulation, 112 (2005) 3073-3079.
[12] C.A. Pope, R.T. Burnett, M.J. Thun, E.E. Calle, D. Krewski, K. Ito, G.D. Thurston, Lung cancer, cardiopulmonary mortality, and long-term exposure to fine particulate air pollution, JAMA, 287 (2002) 1132-1141.
[13] K.B. Metzger, P.E. Tolbert, M. Klein, J.L. Peel, W.D. Flanders, K. Todd, J.A. Mulholland, P.B. Ryan, H. Frumkin, Ambient air pollution and cardiovascular emergency department visits, Epidemiology, 15 (2004) 46-56.
[14] A.G. Russell, B. Brunekreef, A Focus on Particulate Matter and Health, Environ. Sci. Technol., 43 (2009) 4620-4625.
[15] S.P. Newman, W.W. Busse, Evolution of dry powder inhaler design, formulation, and performance, Respiratory medicine, 96 (2002) 293-304.
[16] T.C. Kurtén, M. Noppel, H. Vehkamäki, M. Salonen, M. Kulmala, Quantum chemical studies of hydrate formation of H_2SO_4 and HSO_4^-, Boreal Environ. Res., 12 (2007) 431-453.
[17] E.R. Lovejoy, J. Curtius, K.D. Froyd, Atmospheric ion-induced nucleation of sulfuric acid and water, J. Geophys. Res.: Atmos., 109 (2004).
[18] J. Duplissy, M.B. Enghoff, K.L. Aplin, F. Arnold, H. Aufmhoff, M. Avngaard, U. Baltensperger, T. Bondo, R. Bingham, K. Carslaw, J. Curtius, A. David, B. Fastrup, S. Gagné, F. Hahn, R.G. Harrison, B. Kellett, J. Kirkby, M. Kulmala, L. Laakso, A. Laaksonen, E. Lillestol, M. Lockwood, J. Mäkelä, V. Makhmutov, N.D. Marsh, T. Nieminen, A. Onnela, E. Pedersen, J.O.P. Pedersen, J. Polny, U. Reichl, J.H. Seinfeld, M. Sipilä, Y. Stozhkov, F. Stratmann, H. Svensmark, J. Svensmark, R. Veenhof, B.

Verheggen, Y. Viisanen, P.E. Wagner, G. Wehrle, E. Weingartner, H. Wex, M. Wilhelmsson, P.M. Winkler, Results from the CERN pilot CLOUD experiment, Atmos. Chem. Phys., 10 (2010) 1635-1647.

[19] M. Kulmala, H. Vehkamäki, T. Petäjä, M. Dal Maso, A. Lauri, V.M. Kerminen, W. Birmili, P.H. McMurry, Formation and growth rates of ultrafine atmospheric particles: a review of observations, J. Aerosol Sci., 35 (2004) 143-176.

[20] C.A. Brock, P. Hamill, J.C. Wilson, H.H. Jonsson, K.R. Chan, Particle Formation in the Upper Tropical Troposphere: A Source of Nuclei for the Stratospheric Aerosol, Science, 270 (1995) 1650-1653.

[21] R.J. Weber, G. Chen, D.D. Davis, R.L. Mauldin, D.J. Tanner, F.L. Eisele, A.D. Clarke, D.C. Thornton, A.R. Bandy, Measurements of enhanced H_2SO_4 and 3-4 nm particles near a frontal cloud during the First Aerosol Characterization Experiment (ACE 1), J. Geophys. Res.: Atmos., 106 (2001) 24107-24117.

[22] M. Sipilä, T. Berndt, T. Petäjä, D. Brus, J. Vanhanen, F. Stratmann, J. Patokoski, R.L. Mauldin, A.P. Hyvärinen, H. Lihavainen, M. Kulmala, The Role of Sulfuric Acid in Atmospheric Nucleation, Science, 327 (2010) 1243-1246.

[23] J. Kirkby, J. Curtius, J. Almeida, E. Dunne, J. Duplissy, S. Ehrhart, A. Franchin, S. Gagné, L. Ickes, A. Kürten, A. Kupc, A. Metzger, F. Riccobono, L. Rondo, S. Schobesberger, G. Tsagkogeorgas, D. Wimmer, A. Amorim, F. Bianchi, M. Breitenlechner, A. David, J. Dommen, A. Downard, M. Ehn, R.C. Flagan, S. Haider, A. Hansel, D. Hauser, W. Jud, H. Junninen, F. Kreissl, A. Kvashin, A. Laaksonen, K. Lehtipalo, J. Lima, E.R. Lovejoy, V. Makhmutov, S. Mathot, J. Mikkila, P. Minginette, S. Mogo, T. Nieminen, A. Onnela, P. Pereira, T. Petäjä, R. Schnitzhofer, J.H. Seinfeld, M. Sipilä, Y. Stozhkov, F. Stratmann, A. Tome, J. Vanhanen, Y. Viisanen, A. Vrtala, P.E. Wagner, H. Walther, E. Weingartner, H. Wex, P.M. Winkler, K.S. Carslaw, D.R. Worsnop, U. Baltensperger, M. Kulmala, Role of sulphuric acid, ammonia and galactic cosmic rays in atmospheric aerosol nucleation, Nature, 476 (2011) 429-433.

[24] J. Jung, P.J. Adams, S.N. Pandis, Regional Air Quality–Atmospheric Nucleation Interactions. Nucleation and Atmospheric Aerosols, in: C.D. O'Dowd, P.E. Wagner (Eds.), Springer Netherlands, 2007, pp. 871-877.

[25] M. Ehn, H. Junninen, T. Petäjä, T.C. Kurtén, V.M. Kerminen, S. Schobesberger, H.E. Manninen, I.K. Ortega, H. Vehkamäki, M. Kulmala, D.R. Worsnop, Composition and temporal behavior of ambient ions in the boreal forest, Atmos. Chem. Phys., 10 (2010) 8513-8530.

[26] I.K. Ortega, T.C. Kurtén, H. Vehkamäki, M. Kulmala, The role of ammonia in sulfuric acid ion induced nucleation, Atmos. Chem. Phys., 8 (2008) 2859-2867.

[27] R. Zhang, I. Suh, J. Zhao, D. Zhang, E.C. Fortner, X. Tie, L.T. Molina, M.J. Molina, Atmospheric New Particle Formation Enhanced by Organic Acids, Science, 304 (2004) 1487-1490.

[28] A.B. Nadykto, F. Yu, Strong hydrogen bonding between atmospheric nucleation precursors and common organics, Chem. Phys. Lett., 435 (2007) 14-18.

[29] T.C. Kurtén, B. Bonn, H. Vehkamäki, M. Kulmala, Computational Study of the Reaction between Biogenic Stabilized Criegee Intermediates and Sulfuric Acid, J. Phys. Chem. A, 111 (2007) 3394-3401.

[30] T.C. Kurtén, V. Loukonen, H. Vehkamäki, M. Kulmala, Amines are likely to enhance neutral and ion-induced sulfuric acid-water nucleation in the atmosphere more effectively than ammonia, Atmos. Chem. Phys., 8 (2008) 4095-4103.

[31] V. Loukonen, T.C. Kurtén, I.K. Ortega, H. Vehkamäki, A.A.H. Pádua, K. Sellegri, M. Kulmala, Enhancing effect of dimethylamine in sulfuric acid nucleation in the presence of water - a computational study, Atmos. Chem. Phys., 10 (2010) 4961-4974.

[32] M. Kulmala, V.-M. Kerminen, On the formation and growth of atmospheric nanoparticles, Atmos. Res., 90 (2008) 132-150.

[33] C.D. O'Dowd, J.L. Jimenez, R. Bahreini, R.C. Flagan, J.H. Seinfeld, K. Hameri, L. Pirjola, M. Kulmala, S.G. Jennings, T. Hoffmann, Marine aerosol formation from biogenic iodine emissions, Nature, 417 (2002) 632-636.

[34] F. Yu, R.P. Turco, Ultrafine aerosol formation via ion-mediated nucleation, Geophys. Res. Lett., 27 (2000) 883-886.

[35] S.-H. Lee, J.M. Reeves, J.C. Wilson, D.E. Hunton, A.A. Viggiano, T.M. Miller, J.O. Ballenthin, L.R. Lait, Particle Formation by Ion Nucleation in the Upper Troposphere and Lower Stratosphere, Science, 301 (2003) 1886-1889.

[36] F. Yu, Nucleation rate of particles in the lower atmosphere: Estimated time needed to reach pseudo-steady state and sensitivity to H_2SO_4 gas concentration, Geophys. Res. Lett., 30 (2003) 1526.

[37] A. Hirsikko, T. Nieminen, S. Gagné, K. Lehtipalo, H.E. Manninen, M. Ehn, U. Hõrrak, V.M. Kerminen, L. Laakso, P.H. McMurry, A. Mirme, S. Mirme, T. Petäjä, H. Tammet, V. Vakkari, M. Vana, M. Kulmala, Atmospheric ions and nucleation: a review of observations, Atmos. Chem. Phys., 11 (2011) 767-798.

[38] M. Kulmala, I. Riipinen, M. Sipilä, H.E. Manninen, T. Petäjä, H. Junninen, M.D. Maso, G. Mordas, A. Mirme, M. Vana, A. Hirsikko, L. Laakso, R.M. Harrison, I. Hanson, C. Leung, K.E.J. Lehtinen, V.-M. Kerminen, Toward Direct Measurement of Atmospheric Nucleation, Science, 318 (2007) 89-92.

[39] H. Svensmark, E. Friis-Christensen, Variation of cosmic ray flux and global cloud coverage-a missing link in solar-climate relationships, J. Atmos. Sol. Terr. Phys., 59 (1997) 1225-1232.

[40] G. Niedner-Schatteburg, V.E. Bondybey, FT-ICR Studies of Solvation Effects in Ionic Water Cluster Reactions, Chem. Rev., 100 (2000) 4059-4086.

[41] M.D. Perkins, F.L. Eisele, First Mass Spectrometric Measurements of Atmospheric Ions at Ground Level, J. Geophys. Res., 89 (1984) 9649-9657.

[42] F.L. Eisele, Identification of tropospheric ions, J. Geophys. Res., 91 (1986) 7897-7906.

[43] P. Schulte, F. Arnold, Pyridinium ions and pyridine in the free troposphere, Geophys. Res. Lett., 17 (1990) 1077-1080.

[44] H. Junninen, M. Ehn, T. Petäjä, L. Luosujärvi, T. Kotiaho, R. Kostiainen, U. Rohner, M. Gonin, K. Fuhrer, M. Kulmala, D.R. Worsnop, A high-resolution mass spectrometer to measure atmospheric ion composition, Atmos. Meas. Tech., 3 (2010) 599-636.

[45] G. Beig, G.P. Brasseur, Model of tropospheric ion composition: A first attempt, J. Geophys. Res., 105 (2000) 22671-22684.

[46] G. Beig, Global change induced trends in ion composition of the troposphere to the lower thermosphere, Ann. Geophys., 26 (2008) 1181-1187.

[47] G. Beig, S. Walters, G. Brasseur, A Two-Dimensional Model of Ion Composition in the Stratosphere 2. Negative Ions, J. Geophys. Res., 98 (1993) 12775-12781.

[48] F.L. Eisele, Natural and Anthropogenic Negative Ions in the Troposphere, J. Geophys. Res., 94 (1989) 2183-2196.

[49] D.J. Tanner, F.L. Eisele, Ions in Oceanic and Continental Air Masses, J. Geophys. Res., 96 (1991) 1023-1031.
[50] T. Schindler, C. Berg, G. Niedner-Schatteburg, V.E. Bondybey, Heterogeneously catalyzed hydrolysis of chlorine nitrate: Fourier-transform ion cyclotron resonance investigations of stratospheric chemistry, J. Chem. Phys., 104 (1996) 3998-4004.
[51] F.L. Eisele, E.R. Lovejoy, E. Kosciuch, K.F. Moore, R.L. Mauldin, J.N. Smith, P.H. McMurry, K. Iida, Negative atmospheric ions and their potential role in ion-induced nucleation, J. Geophys. Res.: Atmos., 111 (2006).
[52] F.L. Eisele, D.J. Tanner, Identification of ions in continental air, J. Geophys. Res.: Atmos., 95 (1990) 20539-20550.
[53] J. Kazil, R.G. Harrison, E.R. Lovejoy, Tropospheric new particle formation and the role of ions, Space Sci. Rev., 137 (2008) 241-255.
[54] L. Laakso, T. Anttila, K.E.J. Lehtinen, P.P. Aalto, M. Kulmala, U. Hõrrak, J. Paatero, M. Hanke, F. Arnold, Kinetic nucleation and ions in boreal forest particle formation events, Atmos. Chem. Phys., 4 (2004) 2353-2366.
[55] F.L. Eisele, First tandem mass spectrometric measurement of tropospheric ions, J. Geophys. Res., 93 (1988) 716-724.
[56] A.W. Castleman, S. Wei, Cluster Reactions, Annu. Rev. Phys. Chem., 45 (1994) 685-719.
[57] M. Yamashita, J.B. Fenn, Electrospray ion source. Another variation on the free-jet theme, J. Phys. Chem., 88 (1984) 4451-4459.
[58] S.J. Gaskell, Electrospray: Principles and Practice, J. Mass Spectrom., 32 (1997) 677-688.
[59] G. Scoles, Atomic and Molecular Beam Methods, Oxford University Press: New York and Oxford, 1988.
[60] A.W. Castleman, R.G. Keesee, Ionic clusters, Chem. Rev., 86 (1986) 589-618.
[61] P. Kebarle, A.M. Hogg, Heats of Hydration and Solvation by Mass Spectrometry, J. Chem. Phys., 42 (1965) 798-799.
[62] P. Kebarle, S.K. Searles, A. Zolla, J. Scarborough, M. Arshadi, Solvation of the hydrogen ion by water molecules in the gas phase. Heats and entropies of solvation of individual reactions. $H^+(H_2O)_{n-1} + H_2O = H^+(H_2O)_n$, J. Am. Chem. Soc., 89 (1967) 6393-6399.
[63] A. Good, D.A. Durden, P. Kebarle, Ion--Molecule Reactions in Pure Nitrogen and Nitrogen Containing Traces of Water at Total Pressures 0.5--4 torr. Kinetics of Clustering Reactions Forming $H^+(H_2O)_n$, J. Chem. Phys., 52 (1970) 212-221.
[64] A. Good, D.A. Durden, P. Kebarle, Mechanism and Rate Constants of Ion--Molecule Reactions Leading to Formation of $H^+(H_2O)_n$ in Moist Oxygen and Air, J. Chem. Phys., 52 (1970) 222-229.
[65] M. Arshadi, R. Yamdagni, P. Kebarle, Hydration of the halide negative ions in the gas phase. II. Comparison of hydration energies for the alkali positive and halide negative ions, J. Phys. Chem., 74 (1970) 1475-1482.
[66] X. Yang, X. Zhang, A.W. Castleman, Chemistry of large hydrated anion clusters $X^-(H_2O)_n$, n = 0-59 and X = OH, O, O_2, and O_3. 2. Reaction of CH_3CN, J. Phys. Chem., 95 (1991) 8520-8524.
[67] H. Wincel, E. Mereand, A.W. Castleman, Jr., Reactions of N_2O_5 with Protonated Water Clusters $H^+(H_2O)_n$, n = 3-30, J. Phys. Chem., 98 (1994) 8606-8610.
[68] H. Wincel, E. Mereand, A.W. Castleman, Gas phase reactions of N_2O_5 with $X^-(H_2O)_n$, X = O, OH, O_2, HO_2, and O_3, J. Phys. Chem., 99 (1995) 1792-1798.

[69] N.G. Adams, D. Smith, The selected ion flow tube (SIFT); A technique for studying ion-neutral reactions, Int. J. Mass Spectrom. Ion Phys., 21 (1976) 349-359.
[70] A.A. Viggiano, F. Dale, J.F. Paulson, Proton transfer reactions of $H^+(H_2O)_{n=2\text{--}11}$ with methanol, ammonia, pyridine, acetonitrile, and acetone, J. Chem. Phys., 88 (1988) 2469-2477.
[71] Y. Kawai, S. Yamaguchi, Y. Okada, K. Takeuchi, Reactions of size-selected protonated water clusters $H^+(H_2O)_n$ (n = 2-6) with an acetone molecule in a guided ion beam apparatus, Int. J. Mass spectrom., 220 (2002) 375-383.
[72] N.F. Dalleska, K. Honma, P.B. Armentrout, Stepwise solvation enthalpies of protonated water clusters: collision-induced dissociation as an alternative to equilibrium studies, J. Am. Chem. Soc., 115 (1993) 12125-12131.
[73] T. Schindler, C. Berg, G. Niedner-Schatteburg, V.E. Bondybey, Solvation of hydrochloric acid in protonated water clusters, Chem. Phys. Lett., 229 (1994) 57-64.
[74] C. Guillaume, J. Lecalve, I. Dimicoli, M. Mons, Magic numbers in the mass distribution of the benzene$^+$-argonn ions: evaporation dynamics and cluster structure, Z. Phys. D-Atoms Mol. Clusters, 32 (1994) 157-165.
[75] J.M. L'Hermite, L. Marcou, F. Rabilloud, P. Labastie, A new method to study metastable fragmentation of clusters using a reflectron time-of-flight mass spectrometer, Rev. Sci. Instrum., 71 (2000) 2033-2037.
[76] T.L. Kruger, J.F. Litton, R.W. Kondrat, R.G. Cooks, Mixture analysis by mass-analyzed ion kinetic energy spectrometry, Anal. Chem., 48 (1976) 2113-2119.
[77] J. Laskin, C. Lifshitz, Kinetic energy release distributions in mass spectrometry, J. Mass Spectrom., 36 (2001) 459-478.
[78] V. Aviyente, M. Iraqi, T. Peres, C. Lifshitz, Tandem mass-spectrometry studies of acetone and acetone water cluster ions, J. Am. Soc. Mass. Spectrom., 2 (1991) 113-119.
[79] H. Vehkamäki, Classical Nucleation Theory in Multicomponent Systems, Springer- Verlag, Berlin-Heidelberg, Germany, 2006.
[80] R. Car, M. Parrinello, Unified Approach for Molecular Dynamics and Density-Functional Theory, Phys. Rev. Lett., 55 (1985) 2471-2474.
[81] C.J. Cramer, Essentials of Computational Chemistry: Theories and Models, 2nd ed., John Wiley & Sons, 2004.
[82] F. Jensen, Introduction to Computational Chemistry, 2nd ed., Wiley, 2006.
[83] I.N. Levine, Quantum Chemistry, 5th ed., Prentice Hall, 1999.
[84] P. Hohenberg, W. Kohn, Inhomogeneous Electron Gas, Phys. Rev., 136 (1964) B864-B871.
[85] W. Kohn, L.J. Sham, Self-Consistent Equations Including Exchange and Correlation Effects, Phys. Rev., 140 (1965) A1133-A1138.
[86] C. Møller, M.S. Plesset, Note on an Approximation Treatment for Many-Electron Systems, Phys. Rev., 46 (1934) 618-622.
[87] J.P. Perdew, A. Ruzsinszky, J.M. Tao, V.N. Staroverov, G.E. Scuseria, G.I. Csonka, Prescription for the design and selection of density functional approximations: More constraint satisfaction with fewer fits, J. Chem. Phys., 123 (2005).
[88] T. Schwabe, S. Grimme, Towards chemical accuracy for the thermodynamics of large molecules: new hybrid density functionals including non-local correlation effects, PCCP, 8 (2006) 4398-4401.
[89] G.A. Shamov, P.H.M. Budzelaar, G. Schreckenbach, Performance of the Empirical Dispersion Corrections to Density Functional Theory: Thermodynamics of

Hydrocarbon Isomerizations and Olefin Monomer Insertion Reactions, J. Chem. Theory Comput., 6 (2010) 477-490.
[90] T. Yanai, D.P. Tew, N.C. Handy, A new hybrid exchange–correlation functional using the Coulomb-attenuating method (CAM-B3LYP), Chem. Phys. Lett., 393 (2004) 51-57.
[91] W.J. Hehre, R.F. Stewart, J.A. Pople, Self-Consistent Molecular-Orbital Methods. I. Use of Gaussian Expansions of Slater-Type Atomic Orbitals, J. Chem. Phys., 51 (1969) 2657-2664.
[92] T.H. Dunning, Gaussian basis sets for use in correlated molecular calculations. I. The atoms boron through neon and hydrogen, J. Chem. Phys., 90 (1989) 1007-1023.
[93] D.E. Woon, T.H. Dunning, Gaussian basis sets for use in correlated molecular calculations. III. The atoms aluminum through argon, J. Chem. Phys., 98 (1993) 1358-1371.
[94] P. Kebarle, A.M. Hogg, Heats of Hydration and Solvation by Mass Spectrometry, J. Chem. Phys., 42 (1965) 798-799.
[95] A.W. Castleman, I.N. Tang, H.R. Munkelwitz, Clustering of Sulfur Dioxide and Water Vapor about Oxonium and Nitric Oxide Ions, Science, 173 (1971) 1025.
[96] P.W. Ryan, C.R. Blakley, M.L. Vestal, J.H. Futrell, Crossed-beam study of the reaction $H_3O^+(D_2O,H_2O)D_2HO^+$, J. Phys. Chem., 84 (1980) 561-567.
[97] D. Smith, N.G. Adams, M.J. Henchman, Studies of the binary reactions of $H_3O^+\cdot(H_2O)_{0,1,2}$ ions and their deuterated analogues with D_2O, H_2O, and NH_3, J. Chem. Phys., 72 (1980) 4951-4957.
[98] G. Hulthe, G. Stenhagen, O. Wennerström, C.-H. Ottosson, Water clusters studied by electrospray mass spectrometry, J. Chromatogr. A, 777 (1997) 155-165.
[99] S.-S. Lin, Detection of Large Water Clusters by a Low rf Quadrupole Mass Filter, Rev. Sci. Instrum., 44 (1973) 516-517.
[100] J.Q. Searcy, J.B. Fenn, Clustering of water on hydrated protons in a supersonic free jet expansion, J. Chem. Phys., 61 (1974) 5282-5288.
[101] J.J.L. Kassner, D.E. Hagen, Comment on "Clustering of water on hydrated protons in a supersonic free jet expansion", J. Chem. Phys., 64 (1976) 1860-1861.
[102] E.A. Steel, K.M. Merz, A. Selinger, A.W. Castleman, Mass spectral and computational free energy studies of alkali metal ion-containing water clusters, J. Phys. Chem., 99 (1995) 7829-7836.
[103] F. Sobott, A. Wattenberg, H.-D. Barth, B. Brutschy, Ionic clathrates from aqueous solutions detected with laser induced liquid beam ionization/desorption mass spectrometry, Int. J. Mass spectrom., 185-187 (1999) 271-279.
[104] A. Selinger, A.W. Castleman, Evidence for the encagement of alkali metal ions through the formation of gas-phase clathrates: Cs^+ in water clusters, J. Phys. Chem., 95 (1991) 8442-8444.
[105] S. Wei, Z. Shi, J.A.W. Castleman, Mixed cluster ions as a structure probe: Experimental evidence for clathrate structure of $(H_2O)_{20}H^+$ and $(H_2O)_{21}H^+$, J. Chem. Phys., 94 (1991) 3268-3270.
[106] K. Laasonen, M.L. Klein, Structural Study of $(H_2O)_{20}$ and $(H_2O)_{21}H^+$ Using Density Functional Methods, J. Phys. Chem., 98 (1994) 10079-10083.
[107] J.-W. Shin, N.I. Hammer, E.G. Diken, M.A. Johnson, R.S. Walters, T.D. Jaeger, M.A. Duncan, R.A. Christie, K.D. Jordan, Infrared Signature of Structures Associated with the $H^+(H_2O)_n$ (n = 6 to 27) Clusters, Science, 304 (2004) 1137-1140.

[108] M. Miyazaki, A. Fujii, T. Ebata, N. Mikami, Infrared Spectroscopic Evidence for Protonated Water Clusters Forming Nanoscale Cages, Science, 304 (2004) 1134-1137.

[109] S.S. Iyengar, M.K. Petersen, T.J.F. Day, C.J. Burnham, V.E. Teige, G.A. Voth, The properties of ion-water clusters. I. The protonated 21-water cluster, J. Chem. Phys., 123 (2005) 084309-084309.

[110] T. Kus, V.F. Lotrich, A. Perera, R.J. Bartlett, An ab initio study of the $(H_2O)_{20}H^+$ and $(H_2O)_{21}H^+$ water clusters, J. Chem. Phys., 131 (2009).

[111] M. Mella, A. Ponti, Alternative low-energy mechanisms for isotopic exchange in Gas-phase D2O-H+(H2O)n reactions, Chemphyschem, 7 (2006) 894-903.

[112] K. Mizuse, A. Fujii, Structural Origin of the Antimagic Number in Protonated Water Clusters $H^+(H_2O)_n$: Spectroscopic Observation of the "Missing" Water Molecule in the Outermost Hydration Shell, J. Phys. Chem. Lett., 2 (2011) 2130-2134.

[113] K. Hansen, P.U. Andersson, E. Uggerud, Activation energies for evaporation from protonated and deprotonated water clusters from mass spectra, J. Chem. Phys., 131 (2009) 124303.

[114] A.T. Blades, M. Peschke, U.H. Verkerk, P. Kebarle, Hydration energies in the gas phase of select $(MX)_mM^+$ ions, where $M^+ = Na^+, K^+, Rb^+, Cs^+, NH_4^+$ and $X^- = F^-, Cl^-, Br^-, I^-, NO_2^-, NO_3^-$. Observed magic numbers of $(MX)_mM+$ ions and their possible significance, J. Am. Chem. Soc., 126 (2004) 11995-12003.

[115] M.K. Beyer, Hydrated metal ions in the gas phase, Mass Spectrom. Rev., 26 (2007) 517-541.

[116] F. Schulz, B. Hartke, Dodecahedral Clathrate Structures and Magic Numbers in Alkali Cation Microhydration Clusters, Chemphyschem, 3 (2002) 98-106.

[117] F. Schulz, B. Hartke, A new proposal for the reason of magic numbers in alkali cation microhydration clusters, Theor. Chim. Acta, 114 (2005) 357-379.

[118] B. Hartke, A. Charvat, M. Reich, B. Abel, Experimental and theoretical investigation of microsolvation of Na^+-ions in the gas phase by high resolution mass spectrometry and global cluster geometry optimization, J. Chem. Phys., 116 (2002) 3588-3600.

[119] A. Khan, Theoretical studies of $Na(H_2O)_{19\text{-}21}^+$ and $K(H_2O)_{19\text{-}21}^+$ clusters: explaining the absence of magic peak for $Na(H_2O)_{20}^+$, Chem. Phys. Lett., 388 (2004) 342-347.

[120] V.E. Bondybey, M.K. Beyer, How many molecules make a solution?, Int. Rev. Phys. Chem., 21 (2002) 277-306.

[121] K.M. Ervin, P.B. Armentrout, Translational energy dependence of Ar^++XY --> ArX^++Y (XY=H_2,D_2,HD) from thermal to 30 eV c.m, J. Chem. Phys., 83 (1985) 166-189.

[122] V.G. Anicich, A.D. Sen, Deuterium exchange in the systems of H_2O^+/H_2O and H_3O^+/H_2O, Int. J. Mass Spectrom. Ion Processes, 172 (1998) 1-14.

[123] K. Honma, P.B. Armentrout, The mechanism of proton exchange: Guided ion beam studies of the reactions, $H(H_2O)_n^+$ (n=1-4)+D_2O and $D(D_2O)_n^+$ (n=1-4)+H_2O, J. Chem. Phys., 121 (2004) 8307-8320.

[124] S. Yamaguchi, S. Kudoh, Y. Okada, T. Orii, K. Takeuchi, T. Ichikawa, H. Nakai, Size-dependent reaction cross section of protonated water clusters $H^+(H_2O)_n$ (n=2-11) with D_2O, J. Phys. Chem. A, 107 (2003) 10904-10910.

[125] Z. Sun, C.-K. Siu, O.P. Balaj, M. Gruber, V.E. Bondybey, M.K. Beyer, Proton Transfer in Ionic Water Clusters, Angew. Chem. Int. Ed., 45 (2006) 4027-4030.

[126] P.U. Andersson, M.J. Ryding, O. Sekiguchi, E. Uggerud, Isotope exchange and structural rearrangements in reactions between size-selected ionic water clusters, $H_3O^+(H_2O)_n$ and $NH_4^+(H_2O)_n$, and D_2O, PCCP, 10 (2008) 6127-6134.

[127] D. Marx, Proton Transfer 200 Years after von Grotthuss: Insights from Ab Initio Simulations, Chemphyschem, 8 (2007) 209-210.

[128] H. Goldschmidt, O. Udby, Über Esterbildung, Z. physik. Chem., 60 (1907) 728-755.

[129] M.M. Mann, A. Hustrulid, J.T. Tate, The Ionization and Dissociation of Water Vapor and Ammonia by Electron Impact, Phys. Rev., 58 (1940) 340-347.

[130] M. Eigen, Proton Transfer, Acid-Base Catalysis, and Enzymatic Hydrolysis. Part I: Elementary Processes, Angewandte Chemie International Edition in English, 3 (1964) 1-19.

[131] G. Zundel, H. Metzger, Energiebänder der tunnelnden Überschuß-Protonen in flüssigen Säuren. Eine IR-spektroskopische Untersuchung der Natur der Gruppierungen $H_5O_2^+$, Z. Phys. Chem., 58 (1968) 225-245.

[132] C.J.D.T. von Grotthuss, Sur la décomposition de l'eau et des corps qu'elle tient en dissolution à l'aide de l'électricité galvanique, Ann. Chim., 58 (1806) 54-73.

[133] N. Agmon, THE GROTTHUSS MECHANISM, Chemical Physics Letters, 244 (1995) 456-462.

[134] O. Markovitch, H. Chen, S. Izvekov, F. Paesani, G.A. Voth, N. Agmon, Special Pair Dance and Partner Selection: Elementary Steps in Proton Transport in Liquid Water, J. Phys. Chem. B, 112 (2008) 9456-9466.

[135] M. Tuckerman, K. Laasonen, M. Sprik, M. Parrinello, Ab Initio Molecular Dynamics Simulation of the Solvation and Transport of H_3O^+ and OH^- Ions in Water, J. Phys. Chem., 99 (1995) 5749-5752.

[136] M. Tuckerman, K. Laasonen, M. Sprik, M. Parrinello, Ab initio molecular dynamics simulation of the solvation and transport of hydronium and hydroxyl ions in water, J. Chem. Phys., 103 (1995) 150-161.

[137] M.E. Tuckerman, D. Marx, M. Parrinello, The nature and transport mechanism of hydrated hydroxide ions in aqueous solution, Nature, 417 (2002) 925-929.

[138] P. Brzezinski, P. Ädelroth, Design principles of proton-pumping haem-copper oxidases, Curr. Opin. Struct. Biol., 16 (2006) 465-472.

[139] M. Rini, B.-Z. Magnes, E. Pines, E.T.J. Nibbering, Real-Time Observation of Bimodal Proton Transfer in Acid-Base Pairs in Water, Science, 301 (2003) 349-352.

[140] O.F. Mohammed, D. Pines, J. Dreyer, E. Pines, E.T.J. Nibbering, Sequential Proton Transfer Through Water Bridges in Acid-Base Reactions, Science, 310 (2005) 83-86.

[141] J. Hrušák, G.A. McGibbon, H. Schwarz, J.K. Terlouw, The hydrogen-bridged radical cation $[H_2O\cdots H\cdots O{=}C\text{-}OH^{\cdot +}$: A combined experimental and theoretical study of its stability and dissociation chemistry, Int. J. Mass Spectrom. Ion Processes, 160 (1997) 117-135.

[142] D.K. Bohme, Proton transport in the catalyzed gas-phase isomerization of protonated molecules, Int. J. Mass Spectrom. Ion Processes, 115 (1992) 95-110.

[143] J.C. Jiang, C. Chaudhuri, Y.T. Lee, H.C. Chang, Hydrogen Bond Rearrangements and Interconversions of $H^+(CH_3OH)_4H_2O$ Cluster Isomers, J. Phys. Chem. A, 106 (2002) 10937-10944.

[144] D. Marx, M.E. Tuckerman, J. Hutter, M. Parrinello, The nature of the hydrated excess proton in water, Nature, 397 (1999) 601-604.

[145] J.M.J. Swanson, J. Simons, Role of Charge Transfer in the Structure and Dynamics of the Hydrated Proton, J. Phys. Chem. B, 113 (2009) 5149-5161.

[146] J.H. Gross, Mass Spectrometry, Springer: Berlin, Germany, 2004.

[147] E. de Hoffmann, V. Stroobant, Mass Spectrometry, Principles and Applications, John Wiley & Sons, 2007.

[148] J.R. De Laeter, J.K. Böhlke, P. De Bièvre, H. Hidaka, H.S. Peiser, K.J.R. Rosman, P.D.P. Taylor, Atomic weights of the elements: Review 2000 - (IUPAC technical report), Pure Appl. Chem., 75 (2003) 683-800.

[149] M.J. Frisch, G.W. Trucks, H.B. Schlegel, G.E. Scuseria, M.A. Robb, J.R. Cheeseman, G. Scalmani, V. Barone, B. Mennucci, G.A. Petersson, H. Nakatsuji, M. Caricato, X. Li, H.P. Hratchian, A.F. Izmaylov, J. Bloino, G. Zheng, J.L. Sonnenberg, M. Hada, M. Ehara, K. Toyota, R. Fukuda, J. Hasegawa, M. Ishida, T. Nakajima, Y. Honda, O. Kitao, H. Nakai, T. Vreven, J.A. Montgomery, J.E. Peralta, F. Ogliaro, M. Bearpark, J.J. Heyd, E. Brothers, K.N. Kudin, V.N. Staroverov, R. Kobayashi, J. Normand, K. Raghavachari, A. Rendell, J.C. Burant, S.S. Iyengar, J. Tomasi, M. Cossi, N. Rega, J.M. Millam, M. Klene, J.E. Knox, J.B. Cross, V. Bakken, C. Adamo, J. Jaramillo, R. Gomperts, R.E. Stratmann, O. Yazyev, A.J. Austin, R. Cammi, C. Pomelli, J.W. Ochterski, R.L. Martin, K. Morokuma, V.G. Zakrzewski, G.A. Voth, P. Salvador, J.J. Dannenberg, S. Dapprich, A.D. Daniels, Farkas, J.B. Foresman, J.V. Ortiz, J. Cioslowski, D.J. Fox, Gaussian 09, Revision B.01, in, Wallingford CT, 2009.

[150] V.S. Bryantsev, M.S. Diallo, A.C.T. van Duin, W.A. Goddard, Evaluation of B3LYP, X3LYP, and M06-Class Density Functionals for Predicting the Binding Energies of Neutral, Protonated, and Deprotonated Water Clusters, J. Chem. Theory Comput., 5 (2009) 1016-1026.

[151] D.L. Fiacco, S.W. Hunt, K.R. Leopold, Microwave investigation of sulfuric acid monohydrate, J. Am. Chem. Soc., 124 (2002) 4504-4511.

[152] K.S. Thanthiriwatte, E.G. Hohenstein, L.A. Burns, C.D. Sherrill, Assessment of the Performance of DFT and DFT-D Methods for Describing Distance Dependence of Hydrogen-Bonded Interactions, J. Chem. Theory Comput., 7 (2010) 88-96.

[153] V. Barone, M. Biczysko, M. Pavone, The role of dispersion correction to DFT for modelling weakly bound molecular complexes in the ground and excited electronic states, Chem. Phys., 346 (2008) 247-256.

[154] S.N. Steinmann, C. Corminboeuf, Comprehensive Benchmarking of a Density-Dependent Dispersion Correction, J. Chem. Theory Comput., 7 (2011) 3567-3577.

[155] N. Bork, T. Kurtén, M.B. Enghoff, J.O.P. Pedersen, K.V. Mikkelsen, H. Svensmark, Ab initio studies of $O_2^-(H_2O)_n$ and $O_3^-(H_2O)_n$ anionic molecular clusters, $n \leq 12$, Atmos. Chem. Phys., 11 (2011) 7133-7142.

[156] Y. Li, R. Lu, Y. Hu, X. Wang, Multiphoton ionization and ab initio calculation studies of pyridine–water mixed clusters using time of flight mass spectrometer, Chem. Phys. Lett., 333 (2001) 153-161.

[157] H. Shinohara, U. Nagashima, H. Tanaka, N. Nishi, Magic numbers for water--ammonia binary clusters: Enhanced stability of ion clathrate structures, J. Chem. Phys., 83 (1985) 4183-4192.

[158] X. Yang, A.W. Castleman, Production and magic numbers of large hydrated anion clusters $X^-(H_2O)_{N=0-59}$ (X = hydroxyl, oxygen atom or molecule, and ozone) under thermal conditions, J. Phys. Chem., 94 (1990) 8500-8502.

[159] A.T. Blades, P. Kebarle, Study of the Stability and Hydration of Doubly Charged Ions in the Gas Phase: SO_4^{2-}, $S_2O_6^{2-}$, $S_2O_8^{2-}$, and Some Related Species, J. Am. Chem. Soc., 116 (1994) 10761-10766.

[160] X.-B. Wang, J.B. Nicholas, L.-S. Wang, Electronic instability of isolated SO_4^{2-} and its solvation stabilization, J. Chem. Phys., 113 (2000) 10837-10840.

[161] B. Gao, Z.-f. Liu, A first principles study on the solvation and structure of $SO_4^{2-}(H_2O)_n$, $n = 6$--12, J. Chem. Phys., 121 (2004) 8299-8306.

[162] V. Vchirawongkwin, B.M. Rode, I. Persson, Structure and Dynamics of Sulfate Ion in Aqueous Solution - An ab initio QMCF MD Simulation and Large Angle X-ray Scattering Study, J. Phys. Chem. B, 111 (2007) 4150-4155.

[163] A.R. Bandy, J.C. Ianni, Study of the hydrates of H_2SO_4 using density functional theory, J. Phys. Chem. A, 102 (1998) 6533-6539.

[164] A.B. Nadykto, F.Q. Yu, J. Herb, Theoretical analysis of the gas-phase hydration of common atmospheric pre-nucleation $(HSO_4^-)(H_2O)_n$ and $(H_3O^+)(H_2SO_4)(H_2O)_n$ cluster ions, Chem. Phys., 360 (2009) 67-73.

[165] M. Toivola, I. Napari, H. Vehkamäki, Structure of water-sulfuric acid clusters from molecular dynamics simulations, Boreal Environ. Res., 14 (2009) 654-661.

[166] C.-G. Ding, K. Laasonen, Partially and fully deprotonated sulfuric acid in $H_2SO_4(H_2O)_n$ (n=6-9) clusters, Chem. Phys. Lett., 390 (2004) 307-313.

[167] T. James, D.J. Wales, J. Hernández-Rojas, Global minima for water clusters $(H_2O)_n$, $n \leq 21$, described by a five-site empirical potential, Chem. Phys. Lett., 415 (2005) 302-307.

[168] H.M. Lee, P. Tarakeshwar, J. Park, M.R. Kołaski, Y.J. Yoon, H.-B. Yi, W.Y. Kim, K.S. Kim, Insights into the Structures, Energetics, and Vibrations of Monovalent Cation−$(Water)_{1-6}$ Clusters, J. Phys. Chem. A, 108 (2004) 2949-2958.

[169] B.S. González, J. Hernández-Rojas, D.J. Wales, Global minima and energetics of $Li^+(H_2O)_n$ and $Ca^{2+}(H_2O)_n$ clusters for $n \leqslant 20$, Chem. Phys. Lett., 412 (2005) 23-28.

[170] K. Hashimoto, K. Morokuma, Ab Initio Molecular Orbital Study of $Na(H_2O)_n$ (n = 1-6) Clusters and Their Ions. Comparison of Electronic Structure of the "Surface" and "Interior" Complexes, J. Am. Chem. Soc., 116 (1994) 11436-11443.

[171] J.S. Rao, T.C. Dinadayalane, J. Leszczynski, G.N. Sastry, Comprehensive Study on the Solvation of Mono- and Divalent Metal Cations: Li^+, Na^+, K^+, Be^{2+}, Mg^{2+} and Ca^{2+}, J. Phys. Chem. A, 112 (2008) 12944-12953.

[172] A.A. Viggiano, R.A. Morris, F. Dale, J.F. Paulson, Tropospheric Reactions of $H^+(NH_3)_m(H_2O)_n$ With Pyridine and Picoline, J. Geophys. Res., 93 (1988) 9534-9538.

Atmos. Chem. Phys., 12, 2809–2822, 2012
www.atmos-chem-phys.net/12/2809/2012/
doi:10.5194/acp-12-2809-2012

Atmospheric
Chemistry
and Physics

Reactions of $H^+(\text{pyridine})_m(H_2O)_n$ and $H^+(NH_3)_1(\text{pyridine})_m(H_2O)_n$ with NH_3: experiments and kinetic modelling

M. J. Ryding[1], Å. M. Jonsson[2], A. S. Zatula[3], P. U. Andersson[1], and E. Uggerud[3]

[1]Department of Chemistry, Atmospheric Science, University of Gothenburg, 412 96 Göteborg, Sweden
[2]IVL Swedish Environmental Research Institute Ltd., P.O. Box 5302, 400 14 Göteborg, Sweden
[3]Mass Spectrometry Laboratory and Centre for Theoretical and Computational Chemistry, Department of Chemistry, University of Oslo, P.O. Box 1033 Blindern, 0315 Oslo, Norway

Correspondence to: P. U. Andersson (pan@chem.gu.se)

Received: 23 June 2011 – Published in Atmos. Chem. Phys. Discuss.: 1 September 2011
Revised: 5 February 2012 – Accepted: 19 February 2012 – Published: 16 March 2012

Abstract. Reactions between pyridine containing water cluster ions, $H^+(\text{pyridine})_1(H_2O)_n$, $H^+(\text{pyridine})_2(H_2O)_n$ and $H^+(NH_3)_1(\text{pyridine})_1(H_2O)_n$ (n up to 15) with NH_3 have been studied experimentally using a quadrupole time-of-flight mass spectrometer. The product ions in the reaction between $H^+(\text{pyridine})_m(H_2O)_n$ ($m = 1$ to 2) and NH_3 have been determined for the first time. It is found that the reaction mainly leads to cluster ions of the form $H^+(NH_3)_1(\text{pyridine})_m(H_2O)_{n-x}$, with $x = 1$ or 2 depending on the initial size of the reacting cluster ion. For a given number of water molecules (from 5 to 15) in the cluster ion, rate coefficients are found to be slightly lower than those for protonated pure water clusters reacting with ammonia. The rate coefficients obtained from this study are used in a kinetic cluster ion model under tropospheric conditions. The disagreement between ambient ground level measurements and previous models are discussed in relation to the results from our model and future experimental directions are suggested.

1 Introduction

Atmospheric ions are initially formed by solar radiation, galactic cosmic rays and radioactive decay. The ions are found in the entire atmosphere, although the formation mechanisms vary with altitude, region and time of day. The main products of the ionisation of air are O_2^+, N_2^+ and free electrons (Wayne, 2000). Attachment of neutral polar molecules to the ions leads to charged molecular clusters. Subsequent to cluster formation and growth, ion-ion recombination of positively and negatively charged cluster ions may occur. For small clusters, this is believed to be associated with extensive fragmentation; for large clusters coalescence may occur. These larger neutral clusters formed by the recombination are suggested to be large enough to continue to grow spontaneously into new aerosol particles by condensation (Yu and Turco 2000; Yu 2003).

Several air ion mobility measurements have identified cluster ions in the troposphere. However, the chemical nature of these cluster ions is often difficult to identify (Horrak et al., 2000; Vana et al., 2008). By contrast, there have been measurements and identification of molecule ions in the troposphere during the last two decades. A large fraction of the molecule ions observed in these studies has likely originated from cluster ions that fragment before mass analysis (Eisele, 1983, 1986, 1988; Eisele and McDaniel, 1986; Eisele and Tanner, 1990; Schulte and Arnold, 1990). The first ground based measurement of atmospheric ion composition was performed by Perkins and Eisele in 1983 (Eisele, 1983; Perkins and Eisele, 1984). In the measurements, several unidentified positive ions were observed (Perkins and Eisele, 1984). Improved measurements conducted a few years later revealed the unidentified ions that had a mass-to-charge ratio of 80, 94 and 108 to be protonated pyridine ($C_5H_5NH^+$), protonated picoline (methyl-pyridine) and protonated lutidine (dimethyl-pyridine), respectively (Eisele, 1986, 1988). Several other ions have been identified in the troposphere in addition to these, although pyridinium and its derivatives are often found to dominate the mass spectrum. For example, Schulte and Arnold (1990) identified pyridinium as the dominating ion in air-plane based measurements in the free troposphere over Europe. Recently, Junninen et al. (2010) measured day-time air ions at an urban site (the SMEAR III station in Helsinki), using an Atmospheric Pressure Interface Time-of-Flight instrument. They identified protonated poly(alkyl) pyridines as one of the main positive compound types. Ehn et al. (2010) measured day and night-time air ions at a remote site (the SMEAR II station in Hyytiälä) using the same instrument. They observed pyridine ions and alkyl substituted pyridine ions in both the day and night-time ion spectra, with approximately a factor two higher concentration during night-time.

Sources of atmospheric pyridine and pyridine derivatives are supposed to be biomass burning, automobile exhaust, coal tars and tobacco smoke (Clemo 1973; Saintjalm and Moreetesta, 1980; Beig, 2008). The main atmospheric sink is considered to be reaction with OH radicals (Eisele, 1986; Atkinson et al., 1987; Eisele, 1988; Yeung and Elrod, 2003). Yeung and Elrod (2003) calculated atmospheric lifetimes based on experimentally determined reaction rate coefficients for pyridine and for various substituted pyridine compounds to be 44 days and around 1 to 10 days, respectively. Other suggested atmospheric sinks of significance are reaction with HNO_3 in polluted environments (Atkinson et al., 1987) and reaction with atomic chlorine (Zhao et al., 2007). Due to the localised and sometimes irregular nature of the sources – as well as the relatively short atmospheric lifetimes – the concentration of pyridine is expected to be highly variable with time and location (Beig and Brasseur 2000; Yeung and Elrod, 2003). Few measurements of pyridine concentrations in the atmosphere exist. Among these, Tanner and Eisele (1991) measured a concentration of about 2.5 ppt ± 50 % ($6.2 \times 10^7\,\mathrm{cm}^{-3}$) of molecular pyridine at Mauna Loa Observatory, Hawaii. In the measurements by Junninen et al. (2010) about $1\,\mathrm{cm}^{-3}$ of protonated pyridine was observed at the urban SMEAR III station in Helsinki. However, in contrast to most previous measurements they found up to six times higher concentrations for ionic alkyl substituted pyridine compounds $H^+C_5H_5N(CH_2)_n$, $1 \leq n \leq 6$, including picoline and lutidine. The reason for this is unknown but interesting and the findings show that there is a need to better understand the atmospheric chemistry of these compounds. Ehn et al. (2010) reported average concentrations of pyridinium and alkyl substituted pyridine ions from the SMEAR II station in Hyytiälä during 4 days in early May 2009: pyridinium $36.4\,\mathrm{cm}^{-3}$, picolinium $57.3\,\mathrm{cm}^{-3}$, lutidinium $33.5\,\mathrm{cm}^{-3}$. Also in this case, alkyl substituted pyridine ions were higher in concentration than the pyridine ion.

A kinetic cluster ion model by Beig and Brasseur (2000) indicate that pyridine-containing clusters may be the dominating positive ions in the lower free troposphere (from 1 to 6 km above ground). More specifically, the pyridinated cluster ions in the model were $H^+(X)_1(H_2O)_n$ and $H^+(NH_3)_p(X)_1(H_2O)_n$, where X = pyridine, picoline or lutidine. Beig and Brasseur proposed two reaction pathways for the formation of these pyridinated cluster ions from $H^+(H_2O)_n$ clusters. The first reaction pathway starts with addition of NH_3 to a protonated water cluster. The formed cluster can thereafter react with a pyridine type molecule X:

$$H^+(H_2O)_n + p\mathrm{NH_3} \rightarrow H^+(NH_3)_p(H_2O)_n \qquad \text{(R1a)}$$

$$H^+(NH_3)_p(H_2O)_n + X \rightarrow H^+(X)_1(NH_3)_{p-x}(H_2O)_{n-y} + x\mathrm{NH_3} + y\mathrm{H_2O} \qquad \text{(R1b)}$$

In the second reaction pathway, a pyridine molecule reacts with a protonated water cluster. The pyridine is thereafter ejected when ammonia attaches to the cluster in a second step:

$$H^+(H_2O)_n + X \rightarrow H^+(X)_1(H_2O)_{n-x} + x\mathrm{H_2O} \qquad \text{(R2a)}$$

$$H^+(X)_1(H_2O)_n + p\mathrm{NH_3} \rightarrow H^+(NH_3)_p(H_2O)_n + X \qquad \text{(R2b)}$$

The second step can thereafter be followed by Reaction (R1b) above to form a cluster containing both ammonia and pyridine. The driving force behind these reactions – forming cluster ions containing ammonia and pyridine derivatives – appears connected to the high basicities of ammonia and the pyridine derivatives. Note that loss of water is likely to occur also in the first step of the first mechanism (Reaction R1a) and in the second step of the second mechanism (Reaction R2b); however, this was not included in the notation by Beig and Brasseur.

The rate coefficients for the first three reactions have been determined by Viggiano et al. for the case X = pyridine (Viggiano et al., 1988a, b). The rate coefficients were found to be approximately equal to the collision rate constant. The rate of Reaction (R2b) is unknown; Beig and Brasseur assumed $10^{-11}\,\mathrm{cm}^{-3}\,\mathrm{s}^{-1}$ as an upper limit for the rate coefficient for all pyridine derivatives in their study, this is two orders of magnitude lower than the rate coefficient for Reaction (R1b) at 298 K.

The pyridinated cluster ions, $H^+(X)_1(NH_3)_p(H_2O)_n$, which may be the dominating positive cluster ions in the atmosphere, as suggested by Beig and Brasseur, could potentially be an important source for new aerosol formation. However, these cluster ions have to date not been measured in the atmosphere. This discrepancy has motivated us to perform well controlled experiments to investigate the formation mechanisms of these clusters. The reactions of two types of cluster ions with NH_3 in a cluster beam experiment are studied; the clusters being $H^+(\mathrm{pyridine})_m(H_2O)_n$ ($m = 1$ to 2, $n \leq 15$) and $H^+(NH_3)_1(\mathrm{pyridine})_1(H_2O)_n$ (also $n \leq 15$). The results from the experiments are input to improve the present kinetic model by Beig and Brasseur for atmospheric positive ions. The importance of evaporation of pyridine from the cluster ions is also studied in the improved model. Finally, the atmospheric implications of the experimental results and the results from the kinetic modelling are discussed.

2 Methods

2.1 Experimental

The experiments were performed using a modified quadrupole time-of-flight mass spectrometer (QTOF 2, Micromass/Waters, Manchester UK). The instrument and experimental procedure has been described in detail previously (Andersson et al., 2008; Ryding et al., 2011), and therefore only a brief overview is presented here. The cluster ions were produced from aqueous solutions at atmospheric pressure by electrospray ionization (ESI) and thereafter entered into the high vacuum part of the instrument. Two different solutions were used: 2.5 mM pyridine(aq) for production of $H^+(\text{pyridine})_m(H_2O)_n$ ($m = 1$ to 2, $n \leq 15$) ions and a mixture with 2.5 mM pyridine(aq) and 30 mM NH_3(aq) for production of $H^+(NH_3)_1(\text{pyridine})_1(H_2O)_n$ ions. A quadrupole mass filter (with better than unit resolution) allowed for selection of single sized clusters based on their mass-to-charge ratio, *m/z*. The selected clusters then entered the collision cell, where they were brought to collide with gaseous ammonia at a centre-of-mass (COM) collision energy $E_{\text{COM}} = 8\,\text{kJ mol}^{-1}$ (0.085 eV). The resulting products were analyzed by a reflectron time-of-flight (TOF) mass analyzer set at a mass resolution, $m/\Delta m$, of about 5000 (full-width-half-height). The ammonia was introduced into the collision cell through an Ultra-High-Vacuum (UHV) leak valve giving a pressure of about 10^{-5} mbar. This pressure of NH_3 was chosen to keep the number of collisions below 10 % to ensure single-collision conditions for the entire range of cluster sizes. Reference measurements were collected by measuring the cluster ion $H^+(\text{pyridine})_1(H_2O)_{11}$ at regular intervals during the experiment to make sure that the collision gas pressure was constant. For each measurement, a corresponding background measurement was collected with an empty collision cell. Due to limitations with the current setup the instrument is unable to accurately measure ions below $m/z = 50$; for this reason, the lightest cluster investigated was $H^+(H_2O)_4$. For the cluster ions $H^+(\text{pyridine})_1(H_2O)_{10}$ and $H^+(NH_3)_1(\text{pyridine})_1(H_2O)_{10}$ measurements were also performed at various collision energies between $1.45\,\text{kJ mol}^{-1}$ and $120\,\text{kJ mol}^{-1}$ (COM). A separate set of measurements were performed in order to estimate the evaporation of pyridine from clusters: $H^+(\text{pyridine})_m(H_2O)_5$ and $H^+(NH_3)_1(\text{pyridine})_m(H_2O)_5$ with $m = 1$ to 4 was allowed to pass through the empty collision cell at varying collision energies. In the first series, the energies varied from 0.4 to 2.0 eV (in the lab frame) corresponding to 39 to $193\,\text{kJ mol}^{-1}$, in the second series the energies varied from 0.1 to 0.7 eV corresponding to 10 to $68\,\text{kJ mol}^{-1}$. For producing the clusters containing three or four pyridine molecules, the pyridine concentration in the aqueous solutions was increased to 1.5 M. Reagents used in the experiments: H_2O (no. 95270 for HPLC, Fluka), pyridine (99.5 %, BDH Chemicals Ltd.), NH_3 (99.96 %, AGA), 25 % NH_3 (aq) (Pro analysi, Merck).

2.2 Positive ion model description

The positive cluster ion reaction schemes in this paper are based on the aforementioned model by Beig and Brasseur (2000). In their model, protonated water clusters, $H^+(H_2O)_n$, are continuously produced in a series of reactions starting from O_2^+ and N_2^+. Initially, ions O_2^+ and N_2^+ are formed by galactic cosmic rays and by radioactive decay (close to ground). Charge transfer reactions with molecular oxygen convert N_2^+ to O_2^+. The latter ion then forms O_4^+, which in turn reacts with H_2O to form $O_2^+(H_2O)$. Additional H_2O molecules add to the cluster, which forms $H^+(H_2O)_n$ via loss of O_2 and OH (Beig et al., 1993). Subsequent to this, the protonated water clusters may then react with ammonia, pyridine, picoline, lutidine, acetone and acetonitrile. The production of cluster ions is balanced by the loss of cluster ions through ion-ion recombination and attachment to aerosol particles. The concentration of negative ions in the model was set equal to the concentration of positive ions. In our first model (Model A), we have made two modifications to the model by Beig and Brasseur. Firstly, we have included the experimental results from this study. That is, in the reaction between $H^+(\text{pyridine})_m(H_2O)_n$ ($m = 1$ to 2, $n \leq 15$) and NH_3 virtually no exchange of pyridine for ammonia will take place. Instead, ammonia is incorporated into the cluster ion with subsequent loss of one or two water molecules, i.e. $H^+(\text{pyridine})_m(H_2O)_n + NH_3 \rightarrow H^+(NH_3)_1(\text{pyridine})_m(H_2O)_{n-\text{x}} + \text{x}H_2O$. Hence, the former reaction was excluded from the model and the latter was added (the corresponding modifications were made for the reactions with clusters containing picoline and lutidine). For simplicity, the rate coefficient for $H^+(\text{pyridine})_1(H_2O)_4 + NH_3$ (obtained in this study) was used for all pyridine/water clusters. Secondly, we have included reactions leading to clusters containing two amines (pyridine, picoline and lutidine). The reactions included in Model A are shown in Fig. 1 and the corresponding rate coefficients are given in Table 1. In our second model, Model B, we have omitted the amines picoline and lutidine since pyridine-containing cluster ions are found to be the dominating cluster ions in Model A. We also allowed for up to five pyridine molecules in each cluster. In this model we regard pyridine as a representative for all amines as most amines have high proton affinities and many other amine ions have been found in the atmosphere. The reactions included in this model are shown in Fig. 2 and the corresponding rate coefficients are given in Table 1. In the absence of detailed data for evaporation of pyridine from protonated water clusters and since we do not observe evaporation of pyridine under our experimental conditions (see Sect. 3.1), we excluded evaporation of pyridine in most of the model studies presented in this study. The differential rate equations were solved

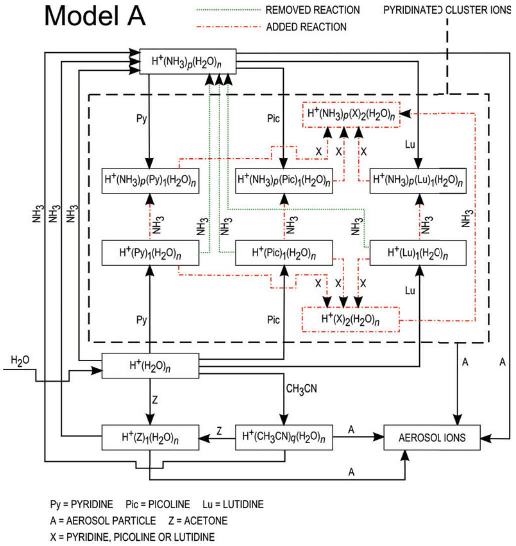

Fig. 1. Tropospheric cluster ion reaction scheme used in Model A. Dotted lines represent reactions removed from the model employed by Beig and Brasseur (2000). Dashed-dotted lines represent reactions not included in the model by Beig and Brasseur (2000).

in the program FACSIMILE (2007). All model calculations in this paper were performed under ground level conditions at a temperature of 298 K. Steady-state concentrations were reached after approximately 500 s.

3 Results

3.1 Experimental results

Figure 3a shows the TOF mass spectrum obtained for mass selected (by the quadrupole) $H^+(\text{pyridine})_1(H_2O)_{11}$ ions passing an empty collision cell. The intensity of the parent ion dominates but minor peaks corresponding to loss of 1 to 5 water molecules are also seen. The loss of water is caused by evaporation from the parent cluster during the flight time of about 160 µs from the quadrupole to the TOF unit. Evaporation is inevitable for the reactions studied here, applying this experimental setup including the setting of the collision energy. In agreement with a previous study by Ryding et al. (2011), loss of pyridine does not occur for this cluster. Figure 3b shows the TOF mass spectrum obtained after reaction between the cluster ion $H^+(\text{pyridine})_1(H_2O)_{11}$ and NH_3 at a collision energy of 8 kJ mol^{-1} (COM). Evaporation of water molecules during the passage through the QTOF 2 is found in approximately the same amounts as in the background measurement. That is, the area of the peaks at *m/z* 18, 36 and 54 u smaller than the parent ion is basically unaffected by the presence of NH_3 in the collision cell. For the reaction with NH_3, the main product formed is $H^+(NH_3)_1(\text{pyridine})_1(H_2O)_9$ at −19 u relative the parent ion mass. This means that NH_3 is incorporated into the cluster and typically two H_2O molecules evaporate from the short-lived collision complex formed. Product clusters corresponding to loss of one, three, four and five H_2O molecules are also seen; however, these products are significantly less abundant. Clusters $H^+(NH_3)_2(\text{pyridine})_1(H_2O)_n$ are produced in small amounts due to multiple collisions with NH_3. Essentially no pyridine is lost from the cluster ions upon reaction, as seen by the absence of significant peaks at the indicated locations in Fig. 3b: for the peaks found at *m/z* 98 and 116 u smaller than the parent ion the intensity is only $< 4 \times 10^{-6}$ compared to the total intensity in the measurement. Figure 3c and d show the corresponding mass spectra for the $H^+(\text{pyridine})_2(H_2O)_{11}$ cluster. The spectra of $H^+(\text{pyridine})_2(H_2O)_{11}$ is in principle the same as

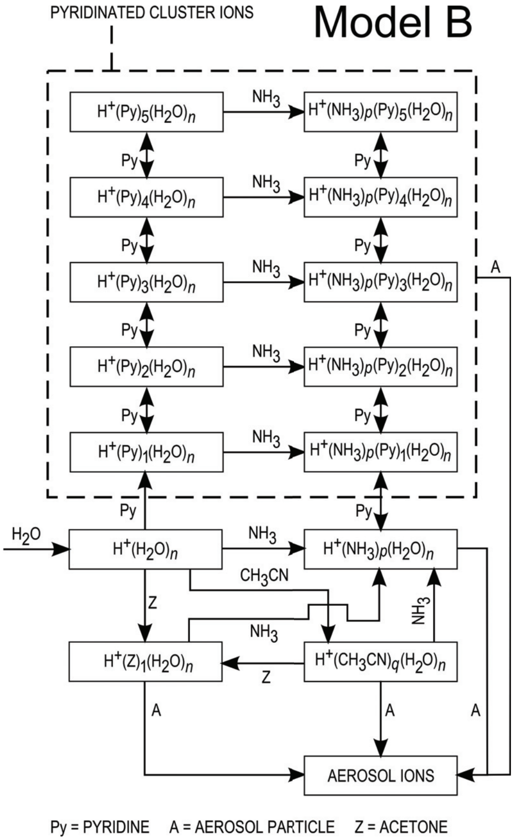

Fig. 2. Tropospheric cluster ion reaction scheme used in Model B.

Table 1. Rate coefficients for the reactions used in Model A and Model B.

Reaction	Rate coefficient, $cm^3\ s^{-1}$	Reference
Formation of $H^+(H_2O)_n$	$Rate_1 = 2$ (unit: $cm^{-3}\ s^{-1}$)	Beig and Brasseur (2000) [a]
$H^+(H_2O)_n + qCH_3CN \rightarrow H^+(CH_3CN)_q(H_2O)_n$	$k_1 = 3.06 \times 10^{-9}(300/T)$	Viggiano et al. (1988a)
$H^+(H_2O)_n + pNH_3 \rightarrow H^+(NH_3)_p(H_2O)_n$	$k_2 = 1.91 \times 10^{-9}(300/T)^{0.39}$	Viggiano et al. (1988a)
$H^+(H_2O)_n + CH_3COCH_3 \rightarrow H^+(CH_3COCH_3)_1(H_2O)_n$	$k_3 = 2.04 \times 10^{-9}(300/T)^{0.59}$	Viggiano et al. (1988a)
$H^+(CH_3COCH_3)_1(H_2O)_n + pNH_3 \rightarrow H^+(NH_3)_p(H_2O)_n$	$k_4 = 2 \times 10^{-9}$	Hauck and Arnold (1984)
$H^+(CH_3CN)_q(H_2O)_n + CH_3COCH_3 \rightarrow H^+(CH_3COCH_3)_1(H_2O)_n$	$k_5 = 1.8 \times 10^{-9}$	Hauck and Arnold (1984)
$H^+(CH_3CN)_q(H_2O)_n + pNH_3 \rightarrow H^+(NH_3)_p(H_2O)_n$	$k_6 = 1.8 \times 10^{-9}$	Schlager et al. (1983)
$H^+(NH_3)_p(H_2O)_n$ + picoline $\rightarrow H^+(NH_3)_p$(picoline)$_1(H_2O)_n$	$k_7 = 2.6 \times 10^{-9}(300/T)^{0.7}$	Viggiano et al. (1988b)
$H^+(NH_3)_p(H_2O)_n$ + lutidine $\rightarrow H^+(NH_3)_p$(lutidine)$_1(H_2O)_n$	$k_8 = 2 \times 10^{-9}$	assumed [b]
$H^+(NH_3)_p(H_2O)_n$ + pyridine $\rightarrow H^+(NH_3)_p$(pyridine)$_1(H_2O)_n$	$k_9 = 2.1 \times 10^{-9}(300/T)^{0.7}$	Viggiano et al. (1988b)
$H^+(H_2O)_n$ + picoline $\rightarrow H^+$(picoline)$_1(H_2O)_n$	$k_{10} = 2 \times 10^{-9}$	assumed [b]
$H^+(H_2O)_n$ + lutidine $\rightarrow H^+$(lutidine)$_1(H_2O)_n$	$k_{11} = 2 \times 10^{-9}$	assumed [b]
$H^+(H_2O)_n$ + pyridine $\rightarrow H^+$(pyridine)$_1(H_2O)_n$	$k_{12} = 2.08 \times 10^{-9}(300/T)^{0.89}$	Viggiano et al. (1988a)
$H^+(X)_1(H_2O)_n + pNH_3 \rightarrow H^+(NH_3)_p(H_2O)_n + X$	$k_{13} = k_{14} = k_{15} = 0$ [c]	assumed
cluster + aerosol $\rightarrow$ aerosol ion	$k_{16} = 5 \times 10^{-6}$	Beig and Brasseur (2000)
cluster + cluster recombination	$k_{17} = 6 \times 10^{-8}(300/T)^{0.5}$ $+1.25 \times 10^{-25}[M](300/T)^4$ [d]	Arijs and Brasseur (1986), Beig et al. (1993)
$H^+(X)_1(H_2O)_n + pNH_3 \rightarrow H^+(NH_3)_p(X)_1(H_2O)_n$	$k_{18} = 0.907 \times k_2$	this work
$H^+(X)_1(H_2O)_n + X \rightarrow H^+(X)_2(H_2O)_n$	$k_{19} = k_{12}$	assumed
$H^+(NH_3)_p(X)_1(H_2O)_n$ + pyridine $\rightarrow H^+(NH_3)_p(X)_2(H_2O)_n$	$k_{20} = k_9$	assumed
$H^+(NH_3)_p(X)_1(H_2O)_n$+ picoline $\rightarrow H^+(NH_3)_p(X)_2(H_2O)_n$	$k_{21} = k_7$	assumed
$H^+(NH_3)_p(X)_1(H_2O)_n$ + lutidine $\rightarrow H^+(NH_3)_p(X)_2(H_2O)_n$	$k_{22} = k_8$	assumed
$H^+(X)_2(H_2O)_n + pNH_3 \rightarrow H^+(NH_3)_p(X)_2(H_2O)_n$	$k_{23} = k_{18}$	assumed
$H^+(NH_3)_p(X)_2(H_2O)_n$ + pyridine $\rightarrow H^+(NH_3)_p(X)_3(H_2O)_n$	$k_{24} = k_9$	assumed
$H^+(NH_3)_p(X)_3(H_2O)_n$ + pyridine $\rightarrow H^+(NH_3)_p(X)_4(H_2O)_n$	$k_{25} = k_9$	assumed
$H^+(NH_3)_p(X)_4(H_2O)_n$ + pyridine $\rightarrow H^+(NH_3)_p(X)_5(H_2O)_n$	$k_{26} = k_9$	assumed

Note that X = pyridine, picoline or lutidine.

[a] The formation of $H^+(H_2O)_n$ was set to give the same rate as used by Beig and Brasseur (2000).

[b] The value is the same as used by Beig and Brasseur (2000).

[c] A value of $1 \times 10^{-11}\ cm^{-3}\ s^{-1}$ was used by Beig and Brasseur (2000).

[d] [M] is the neutral number density in cm^{-3}.

for $H^+(pyridine)_1(H_2O)_{11}$, with the notable exception that loss of a single pyridine molecule (*m/z* 79 u smaller than the parent ion) and loss of a pyridine molecule accompanied by loss of a water molecule (*m/z* 97 u smaller than the parent ion) can be observed. The peaks are found with approximately the same intensity in the background measurement and in the measurement with NH_3 present in the collision cell, with somewhat higher abundance in the former case. However, as will be discussed later, this loss of pyridine is likely resulting from collision induced dissociation (CID) and not evaporation. Due to the above mentioned evaporation of H_2O molecules from the parent ion, some of the detected products will have originated from reactions of pre-formed evaporation products. In order to estimate the contribution of these reactions, we devised the following simple model. The peak at *m/z* 1 u smaller than the parent ion represents the reaction $A^+(H_2O)_n + NH_3 \rightarrow A^+(NH_3)_1(H_2O)_{n-1} + H_2O$ (with $A^+ = H^+$, $H^+(pyridine)_1$, $H^+(pyridine)_2$ or $H^+(NH_3)_1(pyridine)_1$). We assume that all of the evaporation products $A^+(H_2O)_{n-x}$, $x = 1$, 2, 3 in a mass spectrum would form the products $A^+(NH_3)_1(H_2O)_{n-x-1}$, $x = 1$, 2, 3 to a degree that corresponds to the relative intensity of the peak 1 u smaller than the parent ion in a mass spectrum where $A^+(H_2O)_{n-x}$, $x = 1$, 2, 3 is the parent ion. This gives a small contribution from the $A^+(H_2O)_{n-1}$ cluster to the $A^+(NH_3)_1(H_2O)_{n-2}$ peak, located at *m/z* 19 u smaller than the parent ion. The remaining intensity in this peak originate from the parent ion reaction $A^+(H_2O)_n + NH_3 \rightarrow A^+(NH_3)_1(H_2O)_{n-2} + 2H_2O$. We calculated the magnitude of this reaction for all parent ion cluster sizes, and applied it to the correspondingly sized evaporation products as well. We were then able to estimate the magnitude of the third parent ion reaction: $A^+(H_2O)_n + NH_3 \rightarrow A^+(NH_3)_1(H_2O)_{n-3} + 3H_2O$ in the same way. A more thorough description of the procedure can be found in the Supplement.

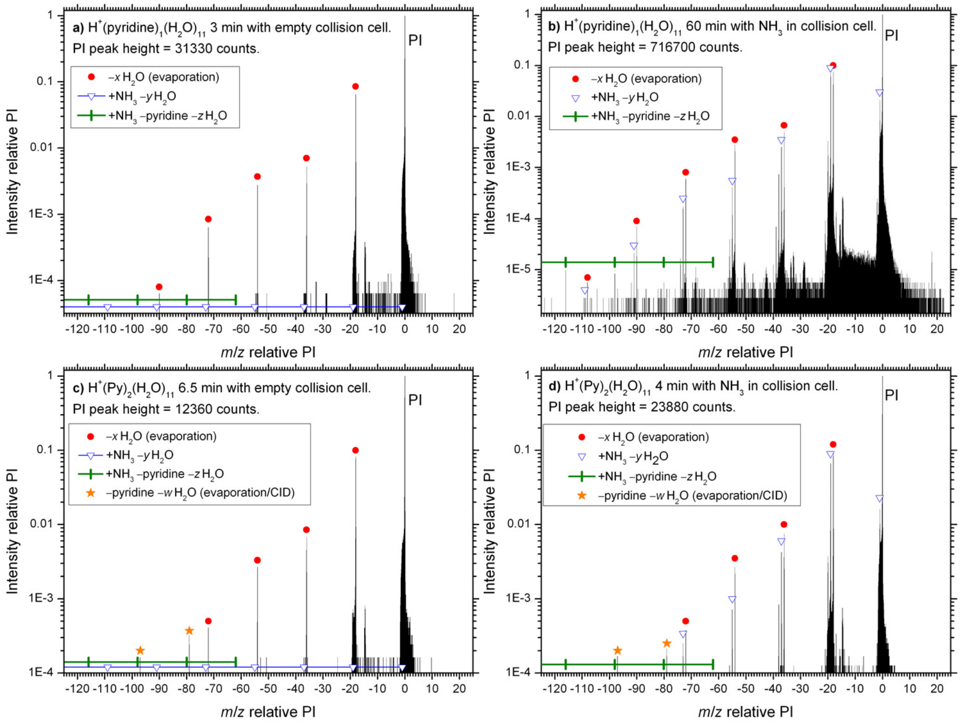

Fig. 3. Mass spectra of $H^+(pyridine)_m(H_2O)_{11}$ with peak intensities expressed relative to the parent ion (PI) mass and height. **(a)** m = 1, background measurement. **(b)** m = 1, the cluster ion reacting with NH_3 at 8 kJ mol^{-1}. **(c)** m = 2, background measurement. **(d)** m = 2, the cluster ion reacting with NH_3 at 8 kJ mol^{-1}. The product $H^+(NH_3)_1(pyridine)_1(H_2O)_{11-y}$ peaks are designated by open blue triangles. Red circles designate peaks arising from evaporation of H_2O from the parent ion. Green vertical lines designate the *m/z* where a possible NH_3/pyridine exchange product, $H^+(NH_3)_1(H_2O)_{10-z}$, would appear. Loss of pyridine without exchange for NH_3 is designated by orange stars.

Figure 4 shows the branching ratios of different products from the $H^+(pyridine)_m(H_2O)_n + NH_3$ reaction ($m = 0$ to 2) at $E_{COM} = 8$ kJ mol^{-1}. For $H^+(H_2O)_n + NH_3$ the main product peaks represent incorporation of the NH_3 molecule and loss of two or three water molecules. The simple model described above attributes the intensity of these peaks to reactions of the parent ion (by 100 % and ≥90 %, respectively). Peaks corresponding to addition of the ammonia molecule and loss of four and five H_2O from the parent cluster can be seen; they tend to be higher for the larger clusters. A significant part of the abundance of these products is likely resulting from reactions of evaporation products; they have been included for comparison. Loss of a single water molecule after reaction with NH_3 is effectively not observed for this cluster type.

The branching ratios of the $H^+(pyridine)_1(H_2O)_n$ and $H^+(pyridine)_2(H_2O)_n$ clusters are rather similar, and are dominated by loss of two water molecules after addition of the ammonia molecule. For smaller clusters, loss of a single water molecule occurs with a frequency similar to the loss of two water molecules. However, the $-H_2O$ curve drops off with size, giving about an order of magnitude lower abundance compared to the $-2H_2O$ products as n approaches 15. Both of these peaks are due to parent ion reactions, while the peaks corresponding to loss of three or four water molecules after addition of ammonia is likely to contain large contributions from reactions of evaporation clusters. Again, we notice that virtually no pyridine leaves the cluster ions after reaction with ammonia, neither for $H^+(pyridine)_1(H_2O)_n$ nor for $H^+(pyridine)_2(H_2O)_n$. This is in contrast to the assumption made by Beig and Brasseur (2000).

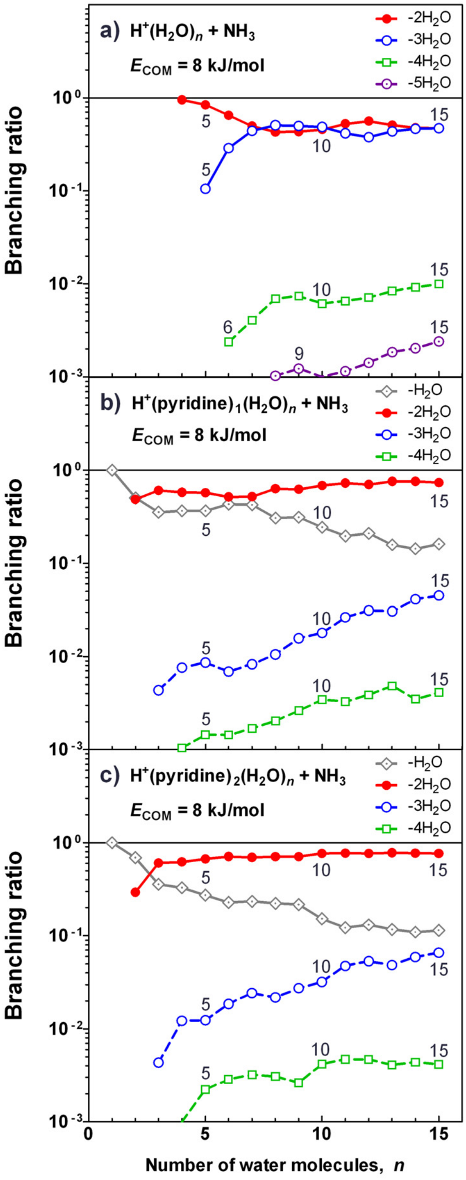

Fig. 4. Branching ratios for the reactions of $H^+(pyridine)_m(H_2O)_n$ ($m = 0$ to 2) with NH_3 at $E_{COM} = 8\,kJ\,mol^{-1}$. The number of water molecules, n, is indicated for some of the data points to improve readability. Dashed lines indicate products likely resulting from clusters that have lost water molecules prior to reaction.

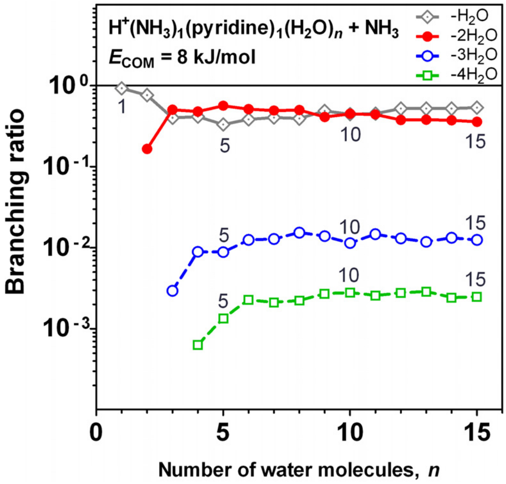

Fig. 5. Branching ratios for $H^+(NH_3)_1(pyridine)_1(H_2O)_n$ reacting with NH_3 at $E_{COM} = 8\,kJ\,mol^{-1}$. The curves represent peaks corresponding to the parent ion incorporating NH_3 and losing one to four H_2O. Dashed lines indicate products likely resulting from clusters that have lost water molecules prior to reaction. The numbers next to the curves indicate the number of water molecules, n.

Branching ratios for the $H^+(NH_3)_1(pyridine)_1(H_2O)_n + NH_3$ reaction are shown in Fig. 5 for $n = 1$ to 15. As seen, the products are dominated by incorporation of the reactant NH_3 and loss of one or two water molecules in more or less equal amounts, except for $n = 2$. Again, these reactions can be attributed to the parent ion by 100 % and ≥ 90 %, respectively. Products with three or four water molecules fewer than the parent ion are also observed and are likely formed from evaporation product reactions. Common for all the curves in Fig. 5 is that they show less size dependence than the clusters in Fig. 4.

The reaction rate coefficients for the clusters $H^+(H_2O)_n$, $H^+(pyridine)_1(H_2O)_n$, $H^+(pyridine)_2\ (H_2O)_n$ and $H^+(NH_3)_1(pyridine)_1(H_2O)_n$ reacting with NH_3 at $8\,kJ\,mol^{-1}$ (COM) are found in Fig. 6 as a function of the number of water molecules in the cluster, $n = 1$ to 15 ($n = 4$ to 15 in the case of pure water clusters). In the absence of an exactly calibrated NH_3 pressure in the collision cell the reaction rate coefficients are expressed relative to the rate coefficient of the $H^+(H_2O)_4$ cluster. It should, however, be mentioned that reference measurements show the pressure to be constant during the course of the experiments. The thermal rate coefficients for the reference cluster $H^+(H_2O)_4$ is $1.91 \times 10^{-9}\ (300/T)^{0.39}\ cm^3\,s^{-1}$, (Viggiano et al., 1988a). For the same cluster reacting with ND_3 at $E_{COM} = 8\,kJ\,mol^{-1}$ (0.085 eV) Honma et al. (1992) reported a reaction cross section of approximately $1.5 \times 10^{-14}\,cm^2$.

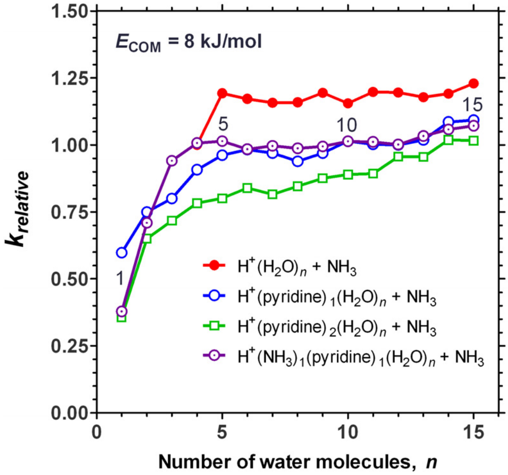

Fig. 6. Relative reaction rate coefficients for cluster ions $H^+(pyridine)_m(H_2O)_n$ (with $m = 0$ to 2) and $H^+(NH_3)_1(pyridine)_1(H_2O)_n$, reacting with NH_3 at $E_{COM} = 8\,kJ\,mol^{-1}$. The rate coefficients are normalized to the rate coefficient for $H^+(H_2O)_4$ reacting with NH_3 ($1.91 \times 10^{-9}\,cm^3\,s^{-1}$ at 298 K (Viggiano et al., 1988a)). The numbers 1, 5, 10, 15 indicate the number of water molecules to improve readability.

For the present case, given a velocity of $1090\,ms^{-1}$ through the collision cell, this corresponds to a reaction rate coefficient of $1.6 \times 10^{-9}\,cm^3\,s^{-1}$ for the reference cluster. As can be seen in Fig. 6, pure water clusters exhibit a somewhat higher reaction rate in the size range $n = 5$ to 15 compared to the pyridine containing clusters.

In order to estimate the rate coefficient for exchanging a pyridine molecule in a cluster with an ammonia molecule i.e. Reaction (R2b) above, we calculated the total abundance of the peaks corresponding to incorporation of ammonia and loss of pyridine and 0 to 2 water molecules. We found that for $H^+(pyridine)_m(H_2O)_n$ clusters with $m = 1$ to 2 and $n = 1$ to 15, the maximum relative rate coefficient for loss of pyridine was 8.0×10^{-4} (the standard deviation due to signal statistics is 2.4×10^{-4}) relative the total rate coefficient for $H^+(H_2O)_4 + NH_3$. Using the value by Viggiano et al. (1988a) for the latter, this gives a rate coefficient of $1.5 \times 10^{-12}\,cm^3\,s^{-1}$ (at 298 K) for the reaction $H^+(pyridine)_1(H_2O)_n + NH_3 \rightarrow H^+(NH_3)_1(H_2O)_{n-x} + xH_2O$ + pyridine. This is a factor of 7 lower than $1 \times 10^{-11}\,cm^3\,s^{-1}$ as assumed by Beig and Brasseur. However, for the majority of the clusters in our study the reaction rate coefficient is even lower. Typical values of the rate coefficient for the above reaction is in the range of 1×10^{-4} to 4×10^{-4} relative $H^+(H_2O)_4$.

Table 2. Initial concentrations in cm^{-3} for the simulations presented in Figs. 7 and 8.

Figure	7	8a–b	8c–d
Model	A	B	B
NH_3	2.46×10^{10}	2.46×10^{10}	4.92×10^{8}
H_2O	4.61×10^{17}	4.61×10^{17}	4.61×10^{17}
Pyridine	variable	variable	variable
Picoline	[pyridine]/10	–	–
Lutidine	[pyridine]/10	–	–
Acetone	3.69×10^{10}	3.69×10^{10}	3.69×10^{10}
CH_3CN	4.92×10^{8}	4.92×10^{8}	4.92×10^{8}
Aerosol	1.0×10^{3}	1.0×10^{3}	1.0×10^{3}
Negative ions	= [positive ions]	= [positive ions]	= [positive ions]

Separate measurements were performed in order to estimate the evaporation of pyridine from clusters containing between one and four pyridine molecules and up to one ammonia molecule. In the Supplement these measurements are described. To summarise, we were unable to determine the evaporation rate coefficients for loss of pyridine from neither of the clusters since a potential weak signal from evaporation could not be separated from collision induced dissociation losses. However, we conclude that the evaporation rate coefficient is of the order $0.1\ s^{-1}$ or lower under the experimental conditions.

3.2 Modelling results

We have modelled the reaction kinetics using three different models. First we performed a calculation using the model of Beig and Brasseur applying their set of parameters, and successfully reproduced their results. We thereafter used Model A at different pyridine concentrations. The concentrations used for all molecules in the model are shown in Table 2. The results are shown in Fig. 7 on a linear scale (in the Supplement the results are shown on a logarithmic scale to include also ions with low concentrations). At pyridine concentrations below $10^4\,cm^{-3}$, clusters of the type $H^+(NH_3)_p(H_2O)_n$ dominate completely but already at pyridine concentrations of $2.8 \times 10^6\ cm^{-3}$, 50 % of the clusters contain both pyridine and ammonia. At concentrations above $5 \times 10^6\,cm^{-3}$, clusters with ammonia, water and two pyridine molecules dominate. Since the lutidine and picoline concentration is 10 times lower than the pyridine concentration, clusters containing both pyridine and lutidine or picoline are found in concentrations about 10 times lower than the concentration of $H^+(NH_3)_p(pyridine)_2(H_2O)_n$. In order to evaluate the importance of including the reaction $H^+(pyridine)_1\ (H_2O)_n + pNH_3 \rightarrow H^+(NH_3)_p(pyridine)_1\ (H_2O)_{n-x} + xH_2O$ in Model A, we also performed calculations in which we substituted this reaction with $H^+(pyridine)_1(H_2O)_n + pNH_3 \rightarrow H^+(NH_3)_p(H_2O)_{n-x} + xH_2O + pyridine$, i.e.

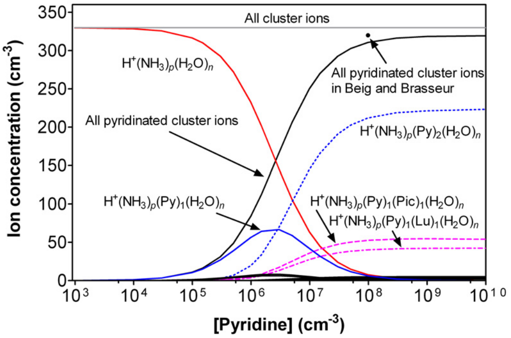

Fig. 7. Concentration of cluster ions as a function of pyridine concentration. The values were calculated using Model A and the initial concentrations are given in Table 2. The total concentration of pyridinated cluster ions in the model by Beig and Brasseur (2000) is also indicated. Py, Pic and Lu indicate pyridine, picoline and lutidine, respectively.

Reaction (R2b). Essentially no difference in ion concentrations obtained from the two models were observed, neither at an ammonia concentration of $2.46 \times 10^{10}\,cm^{-3}$ nor at an ammonia concentration 50 times lower.

A typical pyridine concentration in the troposphere is around 4 ppt ($9.9 \times 10^7\,cm^{-3}$ at 298 K) (Eisele, 1988; Tanner and Eisele, 1991). From Fig. 7 it is clear that more than one pyridine molecule may be present in the cluster ions in the atmosphere provided that evaporation of pyridine from the cluster is small compared to the formation mechanisms (as assumed in the model). In order to study this in more detail we constructed Model B, where up to five pyridine molecules are allowed to be incorporated in each cluster. In Fig. 8, we show the ion concentration as a function of pyridine concentration at a typical ammonia concentration (1.0 ppb, or $2.46 \times 10^{10}\,cm^{-3}$). Assuming no evaporation, a pyridine concentration of 4 ppt ($9.9 \times 10^7\,cm^{-3}$) would give more than four pyridine molecules in most clusters (the maximum number of pyridine molecules in a cluster is five in the model, but the number of pyridine molecules in such a cluster should be regarded as five or more). Neglecting evaporation of pyridine may not be realistic, but this model shows that clusters with a multiple number of pyridine molecules may be present in the atmosphere if evaporation is low (the influence of the evaporation rate on the number of pyridine molecules in the cluster is presented below). In Fig. 8b, the concentrations from Fig. 8a are shown on a logarithmic scale. The concentration of $H^+(CH_3COCH_3)_1(H_2O)_n$, $H^+(H_2O)_n$, and $H^+(CH_3CN)_q(H_2O)_n$ are all below $0.1\,cm^{-3}$ at all pyridine concentrations used. The concentration of $H^+(pyridine)_m(H_2O)_n$ $1 \leq m \leq 5$ are also well below $0.1\,cm^{-3}$ at pyridine concentrations below $3 \times 10^{10}\,cm^{-3}$ and an ammonia concentration of $2.46 \times 10^{10}\,cm^{-3}$.

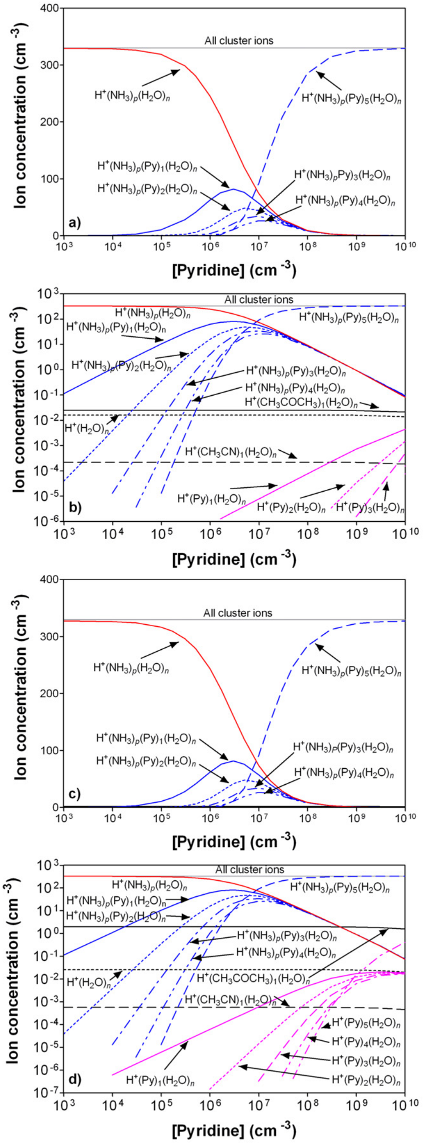

Fig. 8. Concentration of cluster ions as a function of pyridine concentration. The values were calculated using Model B and the initial concentrations are given in Table 2. Panel **(a)** and **(b)** shows the results using an ammonia concentration of $2.46 \times 10^{10}\,cm^{-3}$ on a linear and logarithmic scale, respectively. Panel c) and d) shows the results for an ammonia concentration of $4.92 \times 10^8\,cm^{-3}$. Py, Pic and Lu indicate pyridine, picoline and lutidine, respectively.

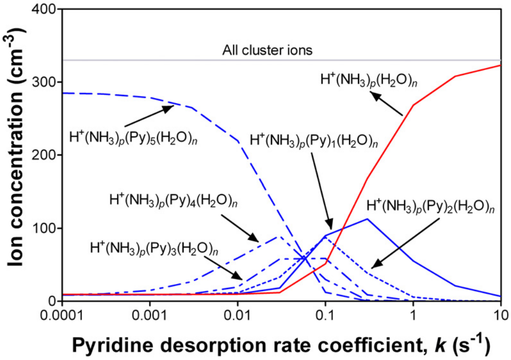

Fig. 9. Concentrations of the most abundant cluster ions as a function of pyridine desorption rate coefficient. The values were calculated using Model B with inclusion of evaporation of pyridine. The initial concentrations are given in Table 2 except the concentration of pyridine that was kept at $9.84 \times 10^7\ \mathrm{cm}^{-3}$.

We also studied the influence of the ammonia concentration on the number of pyridine molecules in the clusters using Model B. Decreasing the ammonia concentration 50 times (shown in Fig. 8c–d) gave no significant change in the concentration of $H^+(\mathrm{pyridine})_m(H_2O)_n$ and $H^+(NH_3)_p(\mathrm{pyridine})_m(H_2O)_n$. However, the concentration of $H^+(CH_3COCH_3)_1(H_2O)_n$ is increased to about $2\ \mathrm{cm}^{-3}$ up to a pyridine concentration of about $10^9\ \mathrm{cm}^{-3}$. The concentrations of $H^+(\mathrm{pyridine})_m(H_2O)_n$ $1 \leq m \leq 5$ are below 0.1 cm^{-3} except for $H^+(\mathrm{pyridine})_5(H_2O)_n$ at pyridine concentrations above $3 \times 10^9 \mathrm{cm}^{-3}$.

Neglecting evaporation of pyridine from clusters $H^+(NH_3)_p(\mathrm{pyridine})_m(H_2O)_n$ is likely not realistic and we therefore studied the importance of this evaporation using Model B with a pyridine concentration of 4 ppt (9.9×10^7 cm^{-3}). The evaporation of pyridine was assumed to be proportional to the number of unprotonated pyridine in the cluster. We also assumed that $H^+(\mathrm{pyridine})_m(H_2O)_n$ have one protonated pyridine and $H^+(NH_3)_p(\mathrm{pyridine})_m(H_2O)_n$ have none protonated pyridine. The results are shown in Fig. 9. As seen in the figure, a desorption rate coefficient as low as $10^{-3}\ \mathrm{s}^{-1}$ ($3.6\ \mathrm{h}^{-1}$) will influence the cluster distribution. At desorption rate coefficients larger than around $10\ \mathrm{s}^{-1}$, clusters containing pyridine are almost absent.

The above presented results from model calculations are all calculated with an aerosol concentration of $1000\ \mathrm{cm}^{-3}$. In order to study the sensitivity of the cluster ion concentration with respect to the aerosol concentration we performed calculations using Model A with aerosol concentrations varying from 10^2 to $10^4\ \mathrm{cm}^{-3}$ and used a fixed pyridine concentration of 4 ppt ($9.9 \times 10^7\ \mathrm{cm}^{-3}$). The results are presented in Figure 10. In clean air (aerosol concentration of $10^2\ \mathrm{cm}^{-3}$) the ion concentrations are slightly higher (around a factor 2) than at intermediate concentrations (aerosol concentration of $10^3\ \mathrm{cm}^{-3}$) but the relation between the cluster ion concentrations are the same. In polluted air (aerosol concentration of $10^4\ \mathrm{cm}^{-3}$) the ion concentration is significantly lower (around a factor 30) than at intermediate concentrations ($10^3\ \mathrm{cm}^{-3}$) and the relation between the cluster ion concentrations are also different: the more pyridine molecules in the cluster, the larger the decrease in concentration.

4 Discussion and atmospheric implications

Honma et al. (1992) studied the reaction of $H^+(H_2O)_4$ with ND_3 and for all products where the ammonia-d3 molecule entered the cluster all three deuterium atoms remained there after evaporation of H_2O. Effective H/D exchange between molecules in the reaction complex requires a mobile proton (Yamaguchi et al., 2003; Honma and Armentrout 2004; Andersson et al., 2008; Ryding et al., 2011). This observation must be the consequence of strong proton binding most likely due to an adamant NH_4^+ core ion, corresponding to its comparably high pK_a value. It has been shown that this absence of H/D exchange extends to larger sizes (Andersson et al., 2008). Thus we expect protonation exclusively on the ammonia molecule for all clusters formed in the reaction $H^+(H_2O)_n + NH_3 \rightarrow H^+(NH_3)_1(H_2O)_{n-x} + xH_2O$. Since the pyridine molecule of a $H^+(\mathrm{pyridine})_1(H_2O)_n$ or $H^+(NH_3)_1(\mathrm{pyridine})_1(H_2O)_n$ cluster does not leave after addition of NH_3, the product will contain two or three basic molecules. This raises a number of interesting questions regarding the cluster structure, dynamics and protonation site. In the case of pure pyridine water clusters, one pyridine molecule in a protonated water cluster leads to locking of the proton (i.e. the proton is bound to the pyridine molecule), while with two or three pyridine molecules in the cluster the proton becomes mobile (Ryding et al., 2011). The situation is more complicated for the present mixed clusters, since we are now dealing with two different types of nitrogen bases. The gas phase proton affinity of pyridine is greater than that of ammonia; they are $930\ \mathrm{kJ\,mol}^{-1}$ and $853.6\ \mathrm{kJ\,mol}^{-1}$, respectively (Lide, 2006c). However, in bulk water, ammonia is the stronger base as indicated by the higher acid dissociation constant of its conjugate acid ($pK_a = 9.25$ for ammonium, $pK_a = 5.23$ for pyridinium, Lide, 2006a,b). The reversal relation of proton affinities in gas phase and in bulk is presumably a consequence of the ability of ammonium to interact with water through four hydrogen bonds, while pyridinium is limited to one hydrogen bond. Since molecular clusters represent a bridge between the domains of gas phase chemistry and bulk, it is difficult to determine the effective proton affinities, and therefore to which degree the proton will be mobile within the reaction complex. Further studies of clusters containing both ammonia and pyridine using deuterated reactants – for instance D_2O – should provide additional clues.

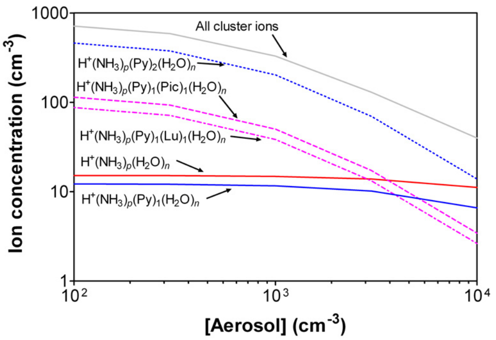

Fig. 10. Concentrations of the most abundant cluster ions as a function of aerosol concentration. The values were calculated using Model A. The initial concentrations are given in Table 2 except the concentration of pyridine that was kept at $9.83 \times 10^7\ cm^{-3}$ and the aerosol concentration that was varied.

The current setup of the TOF unit does not allow for accurate quantification of product ions below $m/z = 50$. For the $H^+(H_2O)_4$ cluster we were only able to measure the reaction products $H^+(NH_3)_1(H_2O)_3$ and $H^+(NH_3)_1(H_2O)_2$ at $m/z = 72$ and $m/z = 54$, respectively. Consequently, the -3H_2O peak is missing for this cluster in Fig. 4a. The experiments by Honma et al. (1992) indicate that the reaction leading to formation of $H^+(NH_3)_1(H_2O)_1$ should represent no more than a few percent of the total abundance; the main product is in fact $H^+(NH_3)_1(H_2O)_2$ ($-2\,H_2O$ in Fig. 4a) which constitutes almost the entire reaction cross section, which is in good agreement with the results in Fig. 4a.

For the experimental setup described in Sect. 2.1, applying collision energy in the lab frame below approximately 0.3 eV was observed to result in inefficient ion transmission and major loss of signal. Measurements are possible, although the sampling time would have to be increased many times over. The collision energy used in the measurements, $8\ kJ\ mol^{-1}$ (COM), was chosen since it allowed for a satisfactory beam intensity to be obtained for all cluster ions studied. This energy is a factor two higher than typical tropospheric collision energies ($\sim 4\ kJ\ mol^{-1}$ at room temperature). However, the heating of the formed reaction complex due to addition of NH_3 (i.e. the dissociation energy) is larger still, with values in the range of 65 to $120\ kJ\ mol^{-1}$ depending on cluster size (based on calculations for clusters with $n = 4$ to 7 using data from Meotner (1984) and Lide (2006c)). The use of higher collision energies would therefore be expected to have only minor effects on the results, as long as the collision energy is sufficiently small compared to the dissociation energy of NH_3 for the cluster in question.

The above mentioned experiment by Honma et al. (1992) show that the total cross section of the $H^+(H_2O)_4$ cluster reacting with ND_3 remains virtually unchanged up to collision energies of $20\ kJ\ mol^{-1}$ (COM). For all measured collision energies in this range, the cross section is made up almost entirely by the reaction forming the product $H^+(NH_3)_1(H_2O)_2$, indicating that the energy released into the cluster upon addition of an ammonia molecule corresponds to evaporation of two H_2O. Based on values calculated using literature thermochemical data (Meotner 1984; Lide 2006c), the energy released by introducing NH_3 into the $H^+(H_2O)_4$ cluster is $120\ kJ\ mol^{-1}$. The dissociation energies for losing first one H_2O and then a second H_2O from the intermediate cluster $H^+(NH_3)_1(H_2O)_4$ are $44\ kJ\ mol^{-1}$ and $52\ kJ\ mol^{-1}$, respectively. For larger protonated water cluster that reacts with NH_3 at $8\ kJ\ mol^{-1}$ (COM) we see approximately equal amounts of evaporation of two and three H_2O from the reaction complex (Fig. 4a), implying a somewhat different balance between the dissociation energies of NH_3 and H_2O. As cluster size increases, the energy released into the cluster when NH_3 enters the reaction complex becomes smaller compared to the energy cost of evaporating first one and then a second water molecule. For instance, for $H^+(H_2O)_7$, the former is $65\ kJ\ mol^{-1}$ while the latter two are $35\ kJ\ mol^{-1}$ and $38\ kJ\ mol^{-1}$, respectively. This is contrary to the experimental findings in Fig. 4a. The discrepancy could be due to the fact that the experimental branching ratios do not necessarily represent a sequential loss of H_2O molecules since there is also a possibility of loss of water as a dimer or a trimer (dissociation energies of the dimer and trimer are $20.7\ kJ\ mol^{-1}$ and $21.7\ kJ\ mol^{-1}$, respectively, Santra et al., 2007). Furthermore, the temperature is higher for larger clusters in the beam, which might be part of the explanation. For the pyridine containing clusters in Fig. 4b–c, the tendency is loss of – on average – fewer water molecules post reaction. Even fewer water molecules are lost from the $H^+(NH_3)_1(\text{pyridine})_1(H_2O)_n$ cluster, with the $+NH_3\ -H_2O$ and $+NH_3\ -2H_2O$ peaks being of equal size. The latter case is likely to be a consequence of the cluster already containing a NH_3 molecule; a similar effect was observed by Viggiano et al. (Viggiano et al., 1988b) for the cases $H^+(H_2O)_n + NH_3$ and $H^+(NH_3)_p(H_2O)_n + NH_3$.

Separate measurements of $H^+(\text{pyridine})_1(H_2O)_{10}$ and $H^+(NH_3)_1(\text{pyridine})_1(H_2O)_{10}$ reacting with NH_3 at different collision energies give further insights into the impact of E_{COM} on the respective branching ratios. In the case of the former, the branching ratios are essentially unchanged below $8\ kJ\ mol^{-1}$, with the branching ratio of $-2\,H_2O$ changing from 0.64 at $8\ kJ\ mol^{-1}$ to 0.60 at $3\ kJ\ mol^{-1}$. The corresponding change for $-H_2O$ is from 0.23 to 0.31. For the latter cluster, the changes are somewhat more significant, with both curves having a branching ratio of 0.43 at $E_{COM} = 8\ kJ\ mol^{-1}$. A change in E_{COM} to $3\ kJ\ mol^{-1}$ results in the $-2H_2O$ curve dropping to 0.35 and the $-H_2O$ curve increasing to 0.56. It would seem that for this cluster, the collision energy of choice (8 kJ mol^{-1}) also happens to be the point where the two curves representing the collision energy dependence of the +NH_3 −H_2O product and the +NH_3−2H_2O product cross each other. Consequently, for typical tropospheric conditions the +NH_3−H_2O product would have a higher abundance than the +NH_3 − 2 H_2O product for this cluster.

The pure water clusters in Fig. 6 have a somewhat higher reaction rate coefficient for collision with NH_3 compared to the pyridine containing cluster for a large part of the size range. This is very similar to the behaviour exhibited by these three cluster types when reacting with D_2O, as reported in a previous study (Ryding et al., 2011).

Model A gave results that were in excellent agreement with those of Beig and Brasseur (2000) with regards to the concentration of pyridinated cluster ions. Our model is also in agreement with Beig and Brasseur in that the pyridinated cluster ions dominates the tropospheric ion spectrum. Our experiments show that the reaction between $H^+(\text{pyridine})_1(H_2O)_n$ and NH_3 does not result in loss of pyridine and that the reaction have a higher rate coefficient than assumed by Beig and Brasseur (by about two orders of magnitude). However, this did not have any significant effect on the modelled cluster distribution. Model A allows for two pyridine derivatives in each cluster ion, and the model calculations show that it should be possible for these clusters to form in the troposphere. In Model B we allowed for up to five pyridines in each cluster ion. The model calculations showed that already at a pyridine concentration of 10^7 cm^{-3} the cluster ion distribution is dominated by clusters containing ammonia, water and five (or more) pyridines (or other amines) when evaporation of pyridine is neglected. When including evaporation of pyridine the outcome depends strongly, as expected, on the evaporation rate coefficient. We estimate that the desorption rate of pyridine was below about 0.1 s^{-1} under the present experimental conditions. As seen in Fig. 9, at this desorption rate the major cluster ions found in Model B are $H^+(NH_3)_p(\text{pyridine})_1(H_2O)_n$ and $H^+(NH_3)_p(\text{pyridine})_2(H_2O)_n$ in equal amounts. However, the temperature of our clusters in the experiments is well below 298 K: hence the evaporation rate of pyridine from water containing clusters at tropospheric temperatures remains unknown.

Measurements by Junninen et al. (2010) and Ehn et al. (2010) suggest that the ions of alkyl substituted pyridine compounds may be more abundant than ordinary protonated pyridine at ground level in urban and boreal environments. This may seem contradictory when considering the atmospheric concentrations of the compounds in question, as well as the lifetime calculations (for instance by Yeung and Elrod, 2003), both of which indicate pyridine as the more common neutral species. However, as pointed out by Junninen et al., the transition from neutral molecule to cation takes place by addition of a proton, which will lead to compounds with higher proton affinity being relatively more abundant in the tropospheric ion spectrum. The proton affinities in question are 930 kJ mol^{-1} for pyridine, 943.4 to 949.1 kJ mol^{-1} (depending on isomer) for picoline and 955.4 to 963.0 kJ mol^{-1} (depending on the isomer) for lutidine (Lide, 2006c). For cluster ions, the type of pyridine or pyridine derivative that enters the clusters (Reactions R1b and R2a) is likely more dependent on concentration than proton affinity. In case of larger water cluster ions with more than one pyridine type molecule the actual protonation site becomes a matter of basicity. Relevant pK_a values are as follows: 5.23 for pyridinium, 5.70 to 6.00 for picolinium (depending on isomer), 6.15 to 6.99 depending on isomer for lutidinium (Lide 2006b). Since the transition from atmospheric pressure to high-vacuum probably leads to a large tendency for fragmentation and/or evaporation of a cluster ion, actual measurements of clusters containing both pyridine and an alkyl substituted variant are likely to be detected as the latter since both the proton affinity and the acid dissociation constants are higher. If also ammonia is present – as indicated by our calculations – the proton may also be situated on the ammonia molecule ($pK_a = 9.25$ for ammonium). The location of the proton is probably also dependent on the cluster size. The fragmentation and evaporation upon sampling could be a reason why clusters containing both ammonia and pyridine (or pyridine derivative) are not observed in the studies by Junninen et al. and Ehn et al. However, our model simulations also show that neglecting evaporation of pyridine in the initial model by Beig and Brasseur may have overestimated the importance of these clusters in the atmosphere. In order to better understand the fragmentation and evaporation processes of these ions during atmospheric measurements, we suggest experimental studies on collision induced dissociation of water cluster ions containing two or more amines. We also suggest detailed studies on evaporation of amines from charged water-containing clusters under tropospheric conditions.

As evident from the measurements by Ehn et al. many ions are missing in order for our model to be universal. Including all ions today is not realistic since many reactions with these ions have unknown rate coefficients. We regard pyridine in our model to represent most amines in the atmosphere and our model should therefore be a good simplification of the complex cluster ion reactions taking place in the troposphere. However, we emphasise that there is a great need for new laboratory measurements and innovative field measurements to determine reaction- and desorption rate coefficients in order to improve the model and our understanding of cluster ion formation in the troposphere. For instance, during field measurements of air ions we suggest that the concentrations of neutral amines are also measured.

Supplementary material related to this article is available online at: http://www.atmos-chem-phys.net/12/2809/2012/acp-12-2809-2012-supplement.zip.

Acknowledgements. This work was supported by the Swedish Research Council, the Norwegian Research Council by the Grant No. 179568/V30 to the Centre for Theoretical and Computational Chemistry through their Centre of Excellence program, and the Nanoparticle in Interactive Environments platform at the Faculty of Science at University of Gothenburg. MJR is grateful for travel grants awarded by the University of Gothenburg through Jubileumsfonden and Filosofiska fakultetens gemensamma donationsnämnd.

Edited by: M. Kulmala

References

Andersson, P. U., Ryding, M. J., Sekiguchi, O. and Uggerud, E.: Isotope exchange and structural rearrangements in reactions between size-selected ionic water clusters, $H_3O+(H_2O)(n)$ and NH_4+(H_2O)(n), and D_2O, Phys. Chem. Chem. Phys., 10, 6127–6134, 2008.

Arijs, E. and Brasseur, G.: Acetonitrile in the Stratosphere and Implications for Positive-Ion Composition, J. Geophys. Res. Atmos., 91, 4003–4016, 1986.

Atkinson, R., Tuazon, E. C., Wallington, T. J., Aschmann, S. M., Arey, J., Winer, A. M. and Pitts, J. N.: Atmospheric Chemistry of Aniline, N,N-Dimethylaniline, Pyridine, 1,3,5-Triazine, and Nitrobenzene, Environ. Sci. Technol., 21, 64–72, 1987.

Beig, G.: Global change induced trends in ion composition of the troposphere to the lower thermosphere, Ann. Geophys., 26, 1181–1187, 2008, http://www.ann-geophys.net/26/1181/2008/.

Beig, G. and Brasseur, G. P.: Model of tropospheric ion composition: A first attempt, J. Geophys. Res. Atmos., 105, 22671–22684, 2000.

Beig, G., Walters, S. and Brasseur, G.: A 2-Dimensional Model of Ion Composition in the Stratosphere .1. Positive-Ions, J. Geophys. Res. Atmos., 98, 12767–12773, 1993.

Clemo, G. R.: Some Aromatic Basic Constituents of Coal Soot, Tetrahedron, 29, 3987–3990, 1973.

Ehn, M., Junninen, H., Petäjä, T., Kurtén, T., Kerminen, V.-M., Schobesberger, S., Manninen, H. E., Ortega, I. K., Vehkamäki, H., Kulmala, M., and Worsnop, D. R.: Composition and temporal behavior of ambient ions in the boreal forest, Atmos. Chem. Phys., 10, 8513–8530, doi:10.5194/acp-10-8513-2010, 2010.

Eisele, F. L.: Direct Tropospheric Ion Sampling and Mass Identification, Int. J. Mass Spectrom. Ion Processes, 54, 119–126, 1983.

Eisele, F. L.: Identification of Tropospheric Ions, J. Geophys. Res. Atmos., 91, 7897–7906, 1986.

Eisele, F. L.: First tandem mass spectrometric measurement of tropospheric ions, J. Geophys. Res. Atmos., 93, 716-24, 1988.

Eisele, F. L. and McDaniel, E. W.: Mass-Spectrometric Study of Tropospheric Ions in The Northeastern and Southwestern United-States, J. Geophys. Res. Atmos., 91, 5183–5188, 1986.

Eisele, F. L. and Tanner, D. J.: Identification of ions in continental air, J. Geophys. Res. Atmos., 95, 20539–50, 1990.

FACSIMILE v4.0 User Guide: MCPA Software Ltd, Oxford, UK, 2007.

Hauck, G. and Arnold, F.: Improved Positive-Ion Composition Measurements in the Upper Troposphere and Lower Stratosphere and the Detection of Acetone, Nature, 311, 547–550, 1984.

Honma, K. and Armentrout, P. B.: The mechanism of proton exchange: Guided ion beam studies of the reactions, H(H_2O)(n)(+) (n = 1–4)+D_2O and D(D_2O)(n)(+) (n=1-4)+H_2O, J. Chem. Phys., 121, 8307–8320, 2004.

Honma, K., Sunderlin, L. S. and Armentrout, P. B.: Reactions of Protonated Water Clusters with Deuterated Ammonia – H(H_2O)N+(N = 1-4) + ND3, Int. J. Mass Spectrom. Ion Processes, 117, 237–259, 1992.

Horrak, U., Salm, J., and Tammet, H.: Statistical characterization of air ion mobility spectra at Tahkuse Observatory: Classification of air ions, J. Geophys. Res.-Atmos., 105, 9291–9302, 2000.

Junninen, H., Ehn, M., Petäjä, T., Luosujärvi, L., Kotiaho, T., Kostiainen, R., Rohner, U., Gonin, M., Fuhrer, K., Kulmala, M., and Worsnop, D. R.: A high-resolution mass spectrometer to measure atmospheric ion composition, Atmos. Meas. Tech., 3, 1039–1053, doi:10.5194/amt-3-1039-2010, 2010.

Lide, D. R.: Dissociation Constants of Inorganic Acids and Bases, CRC Handbook of Chemistry and physics, internet version 2006, D. R. Lide. Boca Raton, FL, USA, Taylor and Francis, 2006a.

Lide, D. R.: Dissociation Constants of Organic Acids and Bases, CRC Handbook of Chemistry and physics, internet version 2006, D. R. Lide. Boca Raton, FL, USA, Taylor and Francis, 2006b.

Lide, D. R.: Proton Affinities, CRC Handbook of Chemistry and physics, internet version 2006, D. R. Lide. Boca Raton, FL, USA, Taylor and Francis, 2006c.

Meotner, M.: The Ionic Hydrogen-Bond and Ion Solvation 2. Solvation of Onium Ions by One to 7 H_2O Molecules – Relations between Monomolecular, Specific, and Bulk Hydration, J. Am. Chem. Soc., 106, 1265–1272, 1984.

Perkins, M. D. and Eisele, F. L.: First mass-spectrometric measurements of atmospheric ions at ground level, J. Geophys. Res. Atmos., 89, 9649–57, 1984.

Ryding, M. J., Zatula, A. S., Andersson, P. U. and Uggerud, E.: Isotope exchange in reactions between D_2O and size-selected ionic water clusters containing pyridine, H+(pyridine)m(H2O)n, Phys. Chem. Chem. Phys., 13, 1356–1367, 2011.

Saintjalm, Y. and Moreetesta, P.: Study of Nitrogen-Containing Compounds in Cigarette-Smoke by Gas Chromatography-Mass Spectrometry, J. Chromatogr., 198, 188–192, 1980.

Santra, B., Michaelides, A. and Scheffler, M.: On the accuracy of density-functional theory exchange-correlation functionals for H bonds in small water clusters: Benchmarks approaching the complete basis set limit, J. Chem. Phys., 127, 2007.

Schlager, H., Fabian, R., and Arnold, F.: A new cluster ion source/ion drift cell apparatus for atmospheric ion studies – First mobility and reaction rate coefficient measurements, 3rd Int. Swarm Seminar, Innsbruck, Austria, 1983.

Schulte, P. and Arnold, F.: Pyridinium Ions and Pyridine in the Free Troposphere, Geophys. Res. Lett., 17, 1077–1080, 1990.

Tanner, D. J. and Eisele, F. L.: Ions in Oceanic and Continental Air Masses, J. Geophys. Res. Atmos., 96, 1023–1031, 1991.

Vana, M., Ehn, M., Petaja, T., Vuollekoski, H., Aalto, P., de Leeuw, G., Ceburnis, D., O'Dowd, C. D. and Kulmala, M.: Characteristic features of air ions at Mace Head on the west coast of Ireland, Atmos. Res., 90, 278–286, 2008.

Wayne, R. P.: Chemistry of Atmospheres, Oxford, Oxford University Press, 2000.

Viggiano, A. A., Dale, F., and Paulson, J. F.: Proton transfer reactions of aquated hydrogen ions (H+(H_2O)n = 2–11) with methanol, ammonia, pyridine, acetonitrile, and acetone, J. Chem. Phys., 88, 2469–77, 1988a.

Viggiano, A. A., Morris, R. A., Dale, F., and Paulson, J. F.: Tropospheric Reactions of H+(NH_3)M(H_2O)N with Pyridine and Picoline, J. Geophys. Res. Atmos., 93, 9534–9538, 1988b.

Yamaguchi, S., Kudoh, S., Okada, Y., Orii, T., Takeuchi, K., Ichikawa, T., and Nakai, H.: Size-dependent reaction cross section of protonated water clusters H+(H_2O)(n) (N=2–11) with D2O, J. Phys. Chem. A, 107, 10904–10910, 2003.

Yeung, L. Y. and Elrod, M. J.: Experimental and computational study of the kinetics of OH plus pyridine and its methyl- and ethyl-substituted derivatives, J. Phys. Chem. A, 107, 4470–4477, 2003.

Yu, F. Q.: Nucleation rate of particles in the lower atmosphere: Estimated time needed to reach pseudo-steady state and sensitivity to H_2SO_4 gas concentration, Geophys. Res. Lett., 30, 1526–1529, 2003.

Yu, F. Q. and Turco, R. P.: Ultrafine aerosol formation via ion-mediated nucleation, Geophys. Res. Lett., 27, 883–886, 2000.

Zhao, Z., Huskey, D. T., Olsen, K. J., Nicovich, J. M., McKee, M. L., and Wine, P. H.: Kinetics, mechanism, and thermochemistry of the gas-phase reaction of atomic chlorine with pyridine, Phys. Chem. Chem. Phys., 9, 4383–4394, 2007.

VI